SURFACE ATTRIBUTES AND MULTISCALE FRICTIONAL PROPERTIES OF COTTON (*Gossypium hirsutum L.*) FIBERS

A Dissertation

by

FARZAD HOSSEINALI

Submitted to the Office of Graduate and Professional Studies of
Texas A&M University
in partial fulfillment of the requirements for the degree of

DOCTOR OF PHILOSOPHY

Chair of Committee,	J. Alex Thomasson
Committee Members,	James D. Batteas
	Eric F. Hequet
	Sandun Fernando
Head of Department,	Steve Searcy

May 2018

Major Subject: Biological and Agricultural Engineering

ABSTRACT

Frictional properties of fiber assemblies from different cotton varieties were investigated using a sliding friction tester. Results indicated that frictional characteristics of cotton fibers varied significantly among varieties. A significant, negative correlation between friction coefficient (μ) and fiber yellowness and a strong positive correlation between μ and short-fiber content were observed. Multilinear regression analysis showed that fiber friction is a complex phenomenon that depends on fiber dimensional, mechanical, and surface properties. In addition, a fiber simulation model was developed to explain the partial relationships between the fiber dimensional properties and its frictional characteristics. The model shows that, for assemblies of fibers with the same mass and equal average mean length, the true contact area increases with decreasing fiber maturity and fineness.

In the second phase of this research, surface of cotton fibers from two different samples—with statistically distinct macroscale frictional properties—were further characterized at the nanoscale using various atomic force microscope (AFM) operation modes. A cotton fiber surface is naturally coated with a few hundred nanometer-thick layer of lipids, fatty acids, alcohols, and pectins, collectively called the cotton cuticular wax. Surface topography and friction images of the fibers were obtained with conventional contact mode AFM. The nanomechanical property images—such as adhesion and deformation—were obtained in force tapping mode. The results indicate that fibers with higher macroscale friction were also associated with higher nanoscale

friction, adhesion, and deformation. The differences in nanoscale friction, adhesion, and deformation signals is attributed to fiber surface hydrophobicity and stiffness, which in turn may depend on the waxy layer thickness, fatty acids hydrocarbon chain length, and film viscosity.

DEDICATION

The dissertation is dedicated to my family and friends.

ACKNOWLEDGEMENTS

I would like to thank my committee chair, Professor Alex Thomasson, for his patient encouragement, invaluable advice, and consistent support. He has been a spectacular mentor and taught me how to be a good researcher. I want to extend my gratitude to committee members, Professor James Batteas, Professor Eric Hequet, and Professor Sandun Fernando, for their guidance and support throughout the course of this research. Thanks also go to the Biological & Agricultural Engineering Department faculty and staff for making my time at Texas A&M University a great experience. Access to the Material Characterization Facility (MCF) and Microscopy and Imaging Center (MIC) at Texas A&M University is greatly acknowledged. I also want to extend my gratitude to the Cotton Incorporated for supporting this research project.

CONTRIBUTORS AND FUNDING SOURCES

This work was supported in part by the Cotton Incorporated under Grant 05-755. This work was supported in part by the dissertation committee chair, Professor Alex Thomasson of the Department of Biological and Agricultural Engineering.

TABLE OF CONTENTS

Page

LIST OF FIGURES

Page

LIST OF TABLES

Page

CHAPTER I

INTRODUCTION

Fiber Damage During Lint Cleaning

Fiber Breakage and Nep Formation

Processing of seed cotton into fiber and seed is generally referred to as ginning. An industrial scale ginning facility is composed of multiple unit operations such as a feed control system, dryers, cylinder cleaners, stick machines, extractor feeders, gin stands, lint cleaners, and baling press machines [1]. The importance of monitoring the fiber quality parameters throughout different stages of a ginning operation should be strongly emphasized. Different on-line sensors have been developed and commercialized to control main ginning operation parameters such as the real-time cotton mass flow, the quantity of impurity particles, and the level of fiber moisture content. In comparison, the number of studies concerning the development of in-situ fiber physical properties measurements with potential application in ginning processes is limited. Some of these studies are as follows. Thomasson et al. measured the reflectance of different cotton samples at near infrared (NIR) wavelengths. They showed that ratios of NIR bands are strong predictors of the high volume instrument (HVI) measurements such as Micornaire and length [2]. By applying similar methodology, Sui et al. developed an image-based optical sensor to estimate the cotton Micronaire value [3]. Shahriar et al. developed an imaging system, based on the transfer learning approach, with capability to measure both length and average maturity of individual fibers from their longitudinal images [4]. As has been seen, sensors can be developed based on image processing algorithms to more

precisely monitor fiber quality parameters throughout different stages of fiber processing.

The two main purpose of the overall ginning process are to separate fibers from their seeds, and to improve the composite grade of cotton by removing impurity particles entrapped within masses of fibers. While performing these tasks, special care is taken by cotton ginners to avoid fiber damage and to preserve fiber length characteristics. Nevertheless, it is well documented that the ginning operation breaks some fibers and degrades the mean fiber length [5–11]. Research has shown that fiber damage is a strongly dependent on the sequence of cleaning and ginning machines, settings of the machines, moisture content of fibers during processing, the type of impurities, heating conditions, and inherent physical properties of fibers—which depend on the cotton variety and environmental factors during the growing season. For this reason, ginning machines, which can potentially degrade fiber quality, need to be studied and analyzed in more detail with respect to their effects on fiber quality.

One of the main unit operations in cotton ginning is lint cleaning, which is commonly done with a saw-type lint cleaner (SLC) [12]. Lint cleaning is defined as any dry process related to the release of large foreign matter and fine dust particles from the cotton fiber mass with mechanical and/or pneumatic actions. SLC machines are installed immediately after the gin stand or another SLC machine. An SLC consists of a fiber condenser drum, a controlled-batt feed mechanism, a saw-wire-wrapped cylinder, a set of grid bars around the saw cylinder, and an air suction doffing system. The performance of an SLC machine is often evaluated by variables such as cleaning efficiency, lint

wastage, lint turnout, and reductions in fiber quality (known as fiber damage). Cleaning efficiency is determined by measuring the foreign matter content of a fiber sample before and after the lint cleaning process. Lint wastage is a measure of the fibrous portion of waste material removed by an SLC machine. Changes in fiber quality are calculated by measuring certain fiber quality parameters of the fiber sample before and after the lint cleaning process. A desirable lint cleaning process is considered to be the one that removes a maximum of impurity particles (high efficiency) while preserving the fiber length characteristics (low lint damage and wastage). As reported by Sui et al. and Hughs et al., although harsh lint cleaning operations increase lint cleaning efficiency, they negatively impact fiber quality parameters by degrading the average fiber length [11], and increasing both the Short Fiber Content (SFC) and the nep content [13, 14].

In order to understand the origin of forces applied to fibers as they pass through an SLC machine, different stages of a lint cleaning operations are briefly reviewed here [15, 16]. First, fibers, which are separated from their seed, enter the SLC by air current. These fibers are accumulated on a perforated separator cylinder by air pressure, with a suction fan. The forces acting on fibers caused by the air flow have not been reported to cause significant fiber breakage; however, these forces are able to separate some fine dust particles entrained within the fibers. Fibers on the separator cylinder are loosely entangled with one another and form what is known as the cotton batt. Forces that hold fibers together in a batt are due to the inter-fiber friction as a result of the natural bending, convolutions, and crimp of fibers. In modern SLCs, a compressed fiber batt is fed between the separator cylinder and a steel feed plate onto a saw cylinder. Typically,

the saw cylinder rotates at ~1000 rpm, compared to the separator cylinder that turns at ~450 r/min. This variation between the linear velocities of the two cylinders causes a harsh combing action on the fibers. During the combing action, a saw tooth strokes a small tuft of fibers and pulls it away (Figure 1). At the same time that the tuft is being seized by the saw tooth, compressive forces between the feed plate and the separator cylinder loosely grip the other end of the fiber tuft. As a result, the fibers are straightened. The fiber straightening action is of utmost importance since it eases the process of impurity particle removal in the next stages of lint cleaning. Two major forces are applied to fibers in this stage of lint cleaning which may cause fiber breakage: (i) tensile forces along the fiber axis as they are seized by a saw tooth and (ii) frictional force on fiber surfaces as they rapidly travel around the edge of a feed plate. Therefore, the manner in which fibers are delivered to the saw is a critical mechanical procedure that determines largely both the cleaning efficiency and the fiber damage. As the saw tooth and the fibers attached to it continue to rotate with the approximate linear velocity of 20 m/s, the fiber tuft will be dragged and scrubbed against eight sharp-edge grid bars. Two primary purposes of grid bars are to separate impurity particles from fibers and to deflect fibers to remain on the saw cylinder. The fiber-grid bar interaction can be divided into four continuous steps. In step one, before fibers approach the grid bar, centrifugal forces with respect to the axis of rotation cause slight elevation of the fibers from the cylinder surface (Figure 1a). Impurity particles with more mass have more centrifugal force acting upon them. As a result, large impurity particles and some poorly attached fibers are separated by centrifugal force. In step two, the middle section of the fiber tuft

impacts against the edge of the grid bar (Figure 1b). In step three, the tuft rapidly slides over the grid bar under normal pressure due to the centrifugal forces (Figure 1c). Shear stresses applied to the tuft in this step have a tendency to restrain the movement of the tuft. Once a foreign particle encounters the grid bar edge, it functions as a surface impurity or a bump compared to the flat surface of the fibrous assembly. Therefore, since there is more contact area and interaction between the particles and the stiff grid bar, frictional forces acting on them are higher. In the case where the sum of these resistance forces is high compared to the forces holding the particle inside the assembly, the particle will be detached from the tuft to dissipate the frictional energy. As a result, the particle rebounds from the grid bar and is separated from the tuft. The same thing can be said for individual fibers within fiber tufts; that is, if a significant amount of frictional force is applied to fibers by grid bars, they are either separated from the tuft or break into smaller segments. In step four, fibers travel past the grid bar (Figure 1d). At the end of lint cleaning process, straightened fibers are collected from the saw cylinder and transported to the next stage of the ginning operation. Throughout a lint cleaning process, pneumatic, tensile, centrifugal, and frictional forces are applied to fibers. Among these, tensile and high-speed frictional forces cause fiber breakage and damage. While several studies have been conducted on tensile properties of fibers, limited research has been published on surface roughness of fiber assemblies and its impact on frictional forces between fibers and the SLC grid bars.

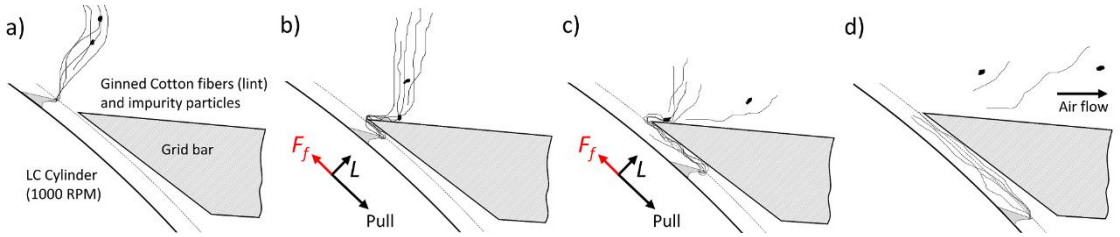

Figure 1 Mechanism of the fiber-grid bar interaction

Friction as a Key Factor

SLC design and developments have been more based on trial-and-error methods than science. Researchers have been trying to optimize the effect of the SLC design factors in order to achieve a maximum cleaning efficiency and retain fiber qualities. Modification and optimization of design factors alter the magnitude of forces and interactions between fibers and machine parts. Some of the published studies on this subject are summarized here. Baker et al. reported that changes in the batt weight, the combing ratio, and the saw speed did not have any major impact on fiber quality measurements [17, 18]. However, they significantly influenced both lint wastage and cleaning efficiency. Baker et al. later studied the effect of the combing ratio on fiber quality measurements and open-end spun yarn properties [19]. Their results showed that increasing the combing ratio from 25 to 50 significantly reduced the 2.5% span length and the upper quartile length; nevertheless, the yarn properties were not affected in a major way. Leonard et al. compared the performance of notched-edge grid bars against regular plain-edge ones [20]. Any modification in grid bars design alters the scrubbing forces applied to fiber tufts. However, they reported that the indentation of the grid bars edge did not affect the level

of fiber damage significantly. Columbus studied influences of four saw cylinder speeds and the saw tooth density on fiber quality parameters and the SLC cleaning efficiency [21]. His results showed that, at a constant combing ratio, an increase in the saw cylinder speed did not affect the HVI upper half-mean length. However, increasing the saw tooth density significantly reduced the upper half-mean length. Baker et al. studied effects of the spacing between grid bars, the curvature radius of grid bars front edge, and the clearance distance between grid bars and the saw teeth on cleaning performance and fiber quality measurements [22]. Their results indicated that the studied variables had no significant effect on HVI parameters. The sharp edge grid bars, however, produced better fiber length distributions as measured by the array method. Mangialardi modified an SLC machine by reversing its feed plate and mounting a round lint-saver bar and a carding brush ahead of the first grid bar [23]. By reversing the feed plate, less frictional shear stresses are placed on fibers since they do not have to travel around the edge of the feed plate once a saw tooth seizes them. His study showed that, although reversing the feed plate improved the fiber quality preservation, it reduced the cleaning performance of the machine. The effects of the round lint-saver bar and the carding brush on fiber quality were not significant. He concluded that the action of fiber and grid bar have a greater impact on the impurity particle removal process than the action of fiber and feed plate. Le studied the effects of saw speed, feed rate, combing ratio, and moisture content on the fiber damage [24]. He concluded that fibers with lower moisture content experienced significantly more breakage throughout the lint cleaning processing. According to his study, the changes in machine settings caused no significant effect on

the typical level of fiber damage imparted by the SLC. Gordon et al. used a laboratory scale SLC and investigated the effects of various lint cleaning elements on fiber quality by eliminating them from the machine [25]. They concluded that the majorly of fiber damage in a SLC takes place when fibers are being delivered from the feed plate onto the saw cylinder. This literature review indirectly shows that the modification of fiber and machine parts interactions—mostly in the form of alteration in frictional forces between fibers and the grid bars or fibers and the feed plate—impacts the magnitude of fiber breakage and damage during the lint cleaning operation.

In addition to machine settings, inherent physical properties of fibers also affect the performance of fibers during a lint cleaning operation. Dever et al. studied the effects of fiber properties on the extent of fiber breakage during ginning operations [26]. They reported that the fiber breakage in the saw ginning and the lint cleaning processes was better correlated with fibers strength and fineness, respectively. Their results showed that, throughout the ginning operation, the finer and stronger fibers from the *gossypium barbadense* cultivar incurred less damage compared to the coarser and weaker ones from the *gossypium hirsutum* type. Their study on relationships between fiber properties and nep formation showed that the final nep count after ginning was significantly correlated with fiber maturity. However, the tendency of fibers to entangle into neps during the ginning operation was reported to be more correlated with the flexural rigidity of fibers—as determined by their length and fineness—and the amount of foreign matter content. Mangialardi et al. reported that both variety and the degree of mechanical lint cleaning significantly impacted the final nep count [27]. Their results showed that the

varieties with lower nep counts were also associated with higher Micronaire values. Hughs et al. conducted a similar type of experiment on seven varieties and four level of lint cleaning [28]. Their results showed that the nepping potential of cotton fibers varies significantly across different varieties and the lint cleaning treatment. These studies signify the influence of the inherent fiber quality parameters on the level of fiber damage during the lint cleaning process. Since significant frictional forces are applied to fibers during lint cleaning, the surface roughness of individual fibers and fiber assemblies are certainly among those inherent fiber quality parameters that directly influence fiber damage in this unit operation.

Literature Review

Friction Laws

For Unlubricated Metallic Materials

Friction affects many industrial waste issues such as large-scale energy dissipation and material losses taking place at contacting interfaces. Friction is defined as the force resisting the relative motion of solid surfaces sliding against each other [29, 30]. In the simplest scenario, when two relatively smooth surfaces slide past each other, molecules at the surface of materials collide with one another (interfacial friction) and, as a result, kinetic energy will be transferred between them. This energy will be distributed among their internal molecules as random motion or heat. In real life examples, the fraction of the energy transferred between sliding surfaces is influenced by the extent of intermolecular attractive forces (adhesion force) and existence of a lubricant film layer between the surfaces (boundary or thin film lubrication). Frictional force between dry

metallic solids obeys the Amontons' law. That is, the friction force F_f between two macroscopic bodies is linearly proportional to the applied load L

$$F_f = \bar{\mu} L \quad (1)$$

Here, $\bar{\mu}$ is the macroscopic coefficient of friction which can be defined both from equation (1), as $\bar{\mu} = F_f/L$, or as a slope in the F_f vs L plot such that $\bar{\mu} = dF/dL$. The coefficient of friction can be measured in either static or dynamic states. The static friction coefficient μ_s determines the lateral force needed to initiate relative motion and is typically larger than the coefficient of kinetic friction μ_k that corresponds to the force needed to continue the motion. Amontons' law is still widely applied to nonadhering and unlubricated contact systems. However, this geometrical interpretation of friction breaks down when surfaces are in adhesive contact or when a liquid film separates them. In order to consider the effect of adhesive bonds on the friction force of smooth surfaces, it has been suggested to modify Amontons' equation to the following form [31]

$$F_f = \bar{\tau} A_{real} + \bar{\mu} L \quad (2)$$

Here, $\bar{\tau}$ is the effective shear strength of contacting bodies at the real contact area A_{real}. The first component of equation (2) accounts for the adhesion-controlled impact (friction force at zero load) and is related to the intermolecular forces between surfaces. The second component accounts for the load-controlled impact and is related to the structure and topography of surfaces. A macroscopic contact, with the apparent contact area of $A_{apparent}$, is rough and consists of n number of smaller contacts. If we denote the contact area of the asperity i by A_i, so that $A_{real} = \sum_{i=1}^{n} A_i$, then equation (2) can be rewritten as

$$F_f = \bar{\tau} \sum_{i=1}^{n} A_i + \bar{\mu} L \qquad (3)$$

At low loads, the friction force is mostly adhesion-controlled. At high loads, irrespective of the relationship between load and real contact area, the friction force is dominated by the load-controlled impact.

For Unlubricated Polymer Solids

Friction, adhesion, and wear of polymer materials have long been studied [32–34]. Specifically, the tribological properties of conventional bulk plastics [35–38], rubber-like materials [39], fiber-reinforced composites [40], polymer nanocomposites [41–43], cross-linked hydrogels [44], end-grafted polymers (a.k.a. polymer brushes) [45], mammalian articular joints [46], gecko-inspired surfaces [47], mussel-inspired coatings [48] have been investigated. For viscoelastic solids, such as polymers, it has been shown that friction is velocity-dependent and equation (1) cannot be valid over a wide range of sliding velocities. In fact, the plot of $F_f \ vs \ V$ is often used for various viscoelastic materials to analyze their energy dissipating mechanisms underlying the friction process. Therefore, for polymers, the coefficient of friction is material-dependent and influenced by both the sliding velocity and the real contact area (especially, at low normal loads).

The polymer sliding friction mechanism may consist of two components: the deformation component, F_d, and the adhesion component, F_a [29, 32]. The relative contributions of these components are influenced by surface roughness, polymer viscoelasticity, the sliding velocity, temperature, moisture content, and lubricity of contacting materials. Jiang et al. showed that, at low normal loads, the thermoplastic olefin surfaces with higher surface roughness are associated with lower static coefficient

of friction [49]. The deformation component arises due to the plowing of asperities of a harder solid through a softer one. Once two rough surfaces slide against each other, if the contact pressure exceeds the yield stress of the junctions, the softer material will deform and will pile up ahead of asperities of the rigid material. This phenomenon is mainly governed by the viscoelastic energy dissipation characteristics of the bulk polymers near deforming asperities. Jiang et al. showed that the plowing of a polymer material ahead of an asperity depends on the mechanical properties of the polymer and its stress-strain curve [50]. The deformation component is therefore proportional to the energy of plowing and affected by the normal load according to the following equation

$$F_d = c(L)^n \tan\delta \qquad (4)$$

where c and n are constant and $\tan\delta$ is the tangent loss, a variable accounting for the internal friction between polymer chains. Equation (4) indicates that the deformation component is affected by the internal friction within a bulk of polymer [39]. The adhesion component, however, is affected by the surface energetics parameters of the polymer and is proportional to the shear strength and the real contact area of the contacting asperities:

$$F_a = \bar{\tau} A_{real} \qquad (5)$$

For rough surfaces, the real contact area is the summation of all singles asperity contacts [51, 52]. Typically, the contact radius of each single asperity junction is in the range of 10 to 100 μm [53]. Fundamental experiments on the interfacial friction mechanism of polymer-on-polymer single asperity contact at this length scale (contact radius of ~30 μm) have been conducted [54–58]. These studies showed that the polymer interfacial friction depends on the arrangement and state of macromolecule chains at, or very near, the surface.

During sliding friction, polymer segments, in the forms of chain loops and free-ends, penetrate into the opposite surface and cause an increase in both the shear angle and the number of van der Waals bonds between the surfaces. It has been reported that changes in the degree of crosslinking or the density of free-ends (chain scission) at the polymer surface significantly affect interfacial polymer-on-polymer friction. In fact, cross-linking of glassy polystyrene (PS) and poly(vinylbenzyl chloride) (PVBC) resulted in lower interfacial friction. This effect was attributed to the reduced density of the polymer segments at the surfaces. As a result of crosslinking, the polymer network becomes more rigid and polymer free-ends might not be able to interpenetrate into the opposing surface. On the other hand, scission (bond-breaking) of the cross-linked PS and PVBC surfaces increased the interfacial friction force considerably. In this scenario, free-ends penetrate deeply into the opposing surface while they are still anchored to their own surface. According to these studies, it can be concluded that interfacial friction force between polymer surfaces depends on the number of chain ends at the surface, the rate of interpenetration of polymer segments, and the extent of the penetration. In addition to these factors, one should also consider the effects of the real contact area and the asperity deformation in analyzing the overall friction mechanism between macroscopic polymeric contact systems. It is reported that the polymer-on-polymer friction mechanism for a single asperity junction can be applied to multiple asperity contacts by implementing proper statistical averaging and summing techniques.

Friction Models for Fibrous Textiles

Several friction models have been proposed to describe the relationships between the friction force, the contact area, and the normal load when fibrous materials slide past each other or another surface [59–63]. Often these models have been used by researchers to explain their contact system of interest without proper knowledge of the origin of these models and the particular assumptions that have to be made. The purpose of this section is to briefly review these models and highlight related assumptions. It will also help us explain our choice of equation (1) as the best fit for our system of study.

Manmade textile fibers are produced from synthetic polymers with well-defined fiber cross-section shape and dimensions. Frictional forces opposing the relative motion of a fiber with respect to its adjacent fibers or another surface can be explained by two mechanisms: adhesion (over the contact area) and viscoelastic surface deformation (or plowing). The friction laws of polymeric surfaces were first applied to the study of friction between textile fibers by Howell [59–61]. Under the assumptions of insignificant surface roughness and zero plowing, he proposed the following equation for friction between two crossed fibers:

$$F_f = aL^n \quad (6)$$

where a and n are constants depending on the fiber type. In the case of contact between two smooth cylindrical surfaces, the theoretical values of the parameters a and n depend on the shear breaking strength, mechanical properties, and dimensions of the cylinders. Equation (6) can be derived from the famous Hertz contact theory in the contact region

between the two elastic sold spheres. Under Howell's assumptions, friction is only proportional to the shear strength of the junctions and the real area of contact such that:

$$F_f = \bar{\tau} A_{real}. \qquad (7)$$

The real contact area for two crossed cylinders is in the shape of a circle with radius a. If we assume that the fibers deform in Hertzian regime, the real contact area can be measured as a function of normal force by:

$$a = \sqrt[3]{\frac{RL}{E_{tot}}}. \quad (8)$$

Therefore, equation (3) takes the following form:

$$F_f = \bar{\tau}\pi \left(\frac{RL}{E_{tot}}\right)^{\frac{2}{3}} \qquad (9)$$

Here, R is the effective radius, defined as $\frac{1}{R} = \frac{1}{R_1} + \frac{1}{R_2}$, where R_1 and R_2 are the radii of circular cross-sections of the fibers. Equation (9) can take the following general form:

$$F_f = \bar{\tau} K L^{\frac{2}{3}}. \quad (10)$$

Here, K is a constant repressing the stiffness and the size of fibers. By comparing equations (6) and (10) the theoretical values for a and n are $a = \bar{\tau}K$ and $n = 2/3$. As can be seen, the parameter a is a general term, with the dimension of $[force]^{1-n}$, which is different from the dimensionless friction coefficient μ in equation (1). The value of $n = 0.67$ is obtained for fully elastic deformation. Howell noted that for pure plastic deformation, n reaches unity and equation (6) becomes identical with the Amontons' law of friction $F_f = \bar{\mu} L$. For viscoelastic materials such as textile fibers, the index n is intermediate between 0.67 and 1.0. Equation (6) has been employed experimentally on

various fibers. For drawn nylon and cellulose acetate fibers, n was measured to be 0.80 and 0.96 respectively [59, 60]. Lincoln, however, reported the value of $n = 0.67$ for nylon fibers [64].

Gupta and El-Mogahzy published a friction model based on Archard's multiple asperities contact approach [62, 63]. In Archard's model, spherical asperities with similar radius of curvature are evenly distributed over the surface of a larger elastic sphere. It was shown by Archard that with an increasing number of asperities m per unit area, A_{real} becomes linearly proportional with L, and frictional forces obey Amontons' law [65]. According to Gupta et al., the total area of real contact in the case of uniform stress distribution can be obtained as

$$A_{real} = K^{-\beta} m^{1-\beta} L^{\beta} \qquad (11)$$

Where K represents the stiffness or the hardness factor and $\beta = 1/(\alpha + 1)$. The constant α is a shape factor in the pressure-area relationship as denoted by $P = KA^{\alpha}$. Here, P is the pressure. In the case of spherical stress distribution, the total area of real contact is expressed as:

$$A_{real} = [\frac{3^{\beta} 2^{1-\beta}}{\beta+2}] K^{-\beta} m^{1-\beta} L^{\beta}. \qquad (12)$$

They further generalized their model to the following form:

$$A_{real} = C_M K^{-\beta} m^{1-\beta} L^{\beta} \quad (13)$$

Here, C_M is a constant related to the nature of the stress distribution. Using this model, they were able to describe the a and n indices in equation (6) in terms of the mechanical properties of asperities and the number of asperities in contact. In addition to the

aforementioned models, several other studies have been conducted to study the frictional properties of textile yarns using the Capstan equation, in which the yarns are modeled as traveling around a pin or a cylinder; these yarn models are outside the scope of this research.

Howell's Friction Law Related to Crossed Fiber Contact

Equation (6) was developed in the 1950s by Howell and gained popularity for the study of fiber friction [32]. Since then, it has been the basis of modern nonlinear friction theories between non-adhesive surfaces at the micro and nanoscale [54]. With developments in Surface Force Apparatuses (SFAs), it is possible to collect both single asperity friction and contact area empirical data between two crossed cylinders coated with materials of interest [55]. With SFAs, data on friction and contact area as a function of applied load can be fit to equation (10) by adjusting the a and n indices or by inserting some known values for both n and K and solving for $\bar{\tau}$. While equation (10) is easy to execute and interpret, care must be taken in fitting this equation for study of various contact problems. The key conditions that have to be met are as follow:

(i) The sublinear relationship between F_f and L holds only in the case of microscale point contacts between smooth fibers under very *light* normal pressures. Upon the occurrence of surface damage and the formation of wear debris between the surfaces, friction will be dominated by $F_f = \bar{\mu}L$. In the study of macroscale friction under relatively high normal force, surface damages and plastic deformation are unavoidable; therefore Amontons' law of friction is found to be a more accurate fit for macroscale friction experiments of bulk materials [31].

(ii) Howell's assumptions of nominally flat surfaces and fibers circular cross-section can be easily violated. For instance, natural fibers, such as desiccated cotton fibers, have nanoscale surface roughness and irregular cross-section shape that can alter the stress distribution inside the contact region and affect the real contact area between the contacting surfaces. According to Archard, and later Greenwood, the validity of Amontons's friction law for a given surface also depends on its surface roughness [51, 65]. Although $F_f \propto L^{2/3}$ for an elastic single-asperity contact, it has been shown that the value of index n tends to reach unity for a rough multiasperity contact.

(iii) One should also consider the effect of environmental conditions on experimental results. Specifically, in the study of biological materials, the outermost layer of the plant cell wall often consists of various amounts of polysaccharides and fatty acids. The polysaccharide constituent of the primary cell wall is a hydrophilic structure, meaning that if contact experiments are not conducted under low humidity, a water meniscus can be formed between the crossed fibers. This water meniscus will affect the overall inter-fiber friction forces.

(iv) In the case of two parallel fibers in contact or a fiber in contact with a flat surface, the contact area is no longer circular. In these cases, the contact area is a rectangle with length l and width $2b$. With Hertz theory, the half-width b and the corresponding friction force in the direction of fiber axis are defined as follows:

$$b = \sqrt{\frac{4RL_l}{\pi E_{tot}}} \quad (14)$$

$$F_f = 4\bar{\tau} l \sqrt{\frac{RL_l}{\pi E_{tot}}}. \quad (15)$$

Here, L_l is the normal force per unit length of l and $F_f \propto L_l^{1/2}$. More recently, Cornelissen et al. have employed the Hertz theory, equations (8) and (14), to quantify the real contact area between two contacting carbon fibers with different crossing angles [66, 67]. In the case where the fibers are not oriented perpendicular or parallel to each other, the contact area is an ellipse with semi-minor and semi-major axes. The area of an elliptical contact geometry can be also predicted by employing the Hertz contact model. (v) Equation (10) assumes Hertzian deformation at the point of contact between two crossed cylinders. In the Hertzian theory, as previously mentioned, the intermolecular attractive forces between the two surfaces are neglected. The Jonson-Kendall-Roberts (JKR) model corrected the Hertz approach by considering attractive forces between surfaces in the form of work-of-adhesion W. In the JKR model [68], the contact radius can be measured by equation (31). By replacing the contact area component in equation (7) with the corresponding JKR component, the friction force at the point of contact between two crossed cylinders (fibers) with adhesion can be measured as

$$F_f = \bar{\tau}\pi\left(\frac{R}{E_{tot}}\left(\sqrt{\frac{3}{2}\pi RW} + \sqrt{L + \frac{3}{2}\pi RW}\right)^2\right)^{\frac{2}{3}}. \quad (16)$$

Although the JKR model is well-developed for spherical contact geometries, limited work has been conducted on the study of JKR-type contact deformation between parallel cylindrical surfaces or a smooth cylinder in contact with a flat surface.

4. Studies on cotton fiber friction

Fiber friction has been reviewed extensively [69–73]. Various books and book chapters are available on this topic. However, ambiguity still exists in fiber friction experimental

techniques and interpretation of fiber friction results. On the study of cotton fiber friction, most experiments have been performed on frictional forces between groups of fibers rather than individual fibers. This is partially due to the difficulties associated with measuring nanoscale frictional force between individual fibers. However, it may also be due to the fact that the fiber bundle friction experiment provides an effective average friction measurement of a sample which reduces the error caused by variation between individual fibers. Also, fiber bundle friction results correlate better with common fiber and yarn physical properties. Following is a brief review of published studies on the subject of frictional properties of cotton fibers. These studies are also listed in Table 1.

Table 1 Previous studies on cotton fiber friction

Authors	Year	Experiment type	Number of samples	Relationship with normal load
Sen et al. [74]	1938	Single fiber withdrawing	17	Not mentioned
Lord [75]	1955	Fiber fringe (combed nearly parallel fibers)	29	$F_f = \bar{\mu}L$
Du Bois [76]	1959	Fiber fringe (combed nearly parallel fibers)	12	$F_f = aL^n$
Belser et al. [77]	1968	Crossed fibers (two single perpendicular fibers)	Not mentioned	$F_f = aL^n$
Hertel [78]	1970	Web of fibers(large scale carding machine webs)	28	$S = \frac{L\,K\,(A_0 - A_n)^2 T}{n^2(A_0 + A_n)}$
Viswanathan [79]	1973	Fiber fringe (combed nearly parallel fibers)	10	$F_f = aL^n$ and $F_f = \bar{\mu}L$
Subramaniam et al. [80, 81]	1981	Fiber fringe (combed nearly parallel fibers)	17	$F_f = aL^n$
El Mogahzy et al. [62]	1993	Fiber fringe (combed nearly parallel fibers)	2	$F_f = aL^n$
El Mogahzy et al. [82]	1998	Rotor ring or fiber opening (inter-fiber friction)	Not mentioned	Not mentioned
Gamble [83]	2006	Rotor ring or fiber opening (inter-fiber friction)	2	Not mentioned
Nowrouzieh et al. [84]	2007	Sliver cohesion (inter-fiber)	2	$F_f = aL^n$
Zhang et al. [85]	2016	Rotating cylinder	1	$F_f = \bar{\mu}L$
Hosseinali et al.	2017	Modified version of ASTM D 1894 for randomly oriented fibrous assemblies	48	$F_f = \bar{\mu}L$

Sen and Ahmad performed a comprehensive investigation on the effects of various fiber quality parameters and experimental conditions on what is called the clinging power of individual cotton fibers [74]. The clinging power is defined as the force necessary to withdraw a fiber along the fiber axis from between two assemblies of parallel fibers in an effort to assess the coefficient of friction of the fiber against its adjacent fibers. Their results on the clinging power of seventeen different cotton varieties showed that samples with larger fiber cell diameter are characterized with higher inter-fiber friction. This is probably because of the larger contact area associated with these fibers. In the study of the effect of fiber convolutions on fiber friction, they reported a weak correlation between the average number of convolutions per unit length and fiber friction. They noted that the effect of convolutions on fiber friction can be masked by other significant factors such as the fiber diameter and the degree of secondary cell wall (SCW) thickness. Also, according to their results, removing the waxy layer from the fiber surface significantly increased the inter-fiber friction. By removing the cotton wax, the overall friction between the fibers increases because of the rougher surface of the layer underneath.

Lord compared the coefficient of friction ($\mu = F_f/L$) of twenty-nine varieties of cottons as measured by withdrawing a fringe of parallel fibers from between two other fringes [75]. He reported correlation coefficients of -0.806 and 0.609 between $\bar{\mu}$ and maturity and $\bar{\mu}$ and convolutions per unit length, respectively. He explained that since mature fibers (higher degree of SCW thickness) have rounder cross-section, it should be

easier for them to slide over one another. Du Bois repeated Lord's work on twelve varieties and concluded that fibers from *Gossypium barbadense* specie are associated with lower friction coefficient compared to those of from *Gossypium hirsutum* [76]. Viswanathan noted that the frictional force between fringes of fibers under low normal force is proportional to $l/\sqrt{MH}$, where l is the mean fiber length, M is the fiber maturity, and H is the fiber fineness [86]. For thirty different cotton varieties, he reported the correlation coefficient of -0.634 between F_f and $l/\sqrt{MH}$. In another study on frictional properties of ten different varieties of cotton fibers, Viswanathan found a negative correlation between yarn strength and frictional forces between fringes of fibers, again under low normal force [79]. This finding confirms that the lower fiber friction at the preparatory stages of yarn manufacturing (opening, carding, drawing, and roving) eases fiber drafting and increases the degree of cohesion in the yarn structure. However, higher fiber friction is more desirable at the final stages of yarn manufacturing (fiber spinning and twisting), where higher friction leads to better binding of fibers in the yarn structure. El Mogahzy et al., measured the frictional of properties of HVI fiber beards as the fiber bundle slips between two parallel metallic plates under controlled normal pressure [87]. They compared frictional properties of Pima and Deltapine cottons and stated that both fiber/metal and fiber/fiber frictional forces are higher for the latter. Roedel et al. studied the frictional properties of cotton/polyester needle-punched nonwoven webs [88]. They explained that looping and interlocking of fibers due to the needling process caused the formation of surface protrusions. These surface irregularities on the web surface enhanced static friction and led to a pronounced stick-slip behavior.

Subramaniam et al. studied the relationships between fiber friction measured with the fiber fringe method and fiber quality parameters among seventeen different cotton samples [80]. They found significant correlation coefficients of -0.73, +0.73, and -0.69 between fiber friction and length, Micronaire, and bundle strength, respectively. Based on the strong positive correlation between Micornaire and fiber friction, it was concluded that inter-fiber friction forces are higher for courser cottons. Subramaniam et al. also investigated the effect of fiber friction on the performance of carding and drawing unit operations [81]. For this purpose, they modified surface characteristics of fibers of a given sample by applying chemical surface treatments, such as surfactants and colloidal silica, to either reduce or enhance fiber friction to a desired amount. Their results indicated that treatment of bulk samples with surfactant decreased both card-wastes and nep numbers per unit area of the card web. Treatment with colloidal silica to enhance inter-fiber friction, had the opposite effect. They explained that low static inter-fiber friction facilitates the smooth and orderly movement of fiber mass throughout different steps of fiber processing. High static inter-fiber friction increases the energy required for separating and disentangling fiber lumps; therefore, the probability that fibers remain in cluster form during the process will be sufficiently enhanced. In practice, in order to achieve a higher degree of lint cleaning, more energy is often consumed to open and separate such clusters, which causes an increase in both the percentages of waste products and broken fibers.

Belser et al. conducted an exclusive study on frictional properties of individual cotton fibers using the crossed fiber technique [77]. By sliding a cotton fiber over an ideal

cylindrical fiber of approximately the same size, they plotted frictional forces between the two fibers as a function of the traveling distance of the moving fiber. Their results showed that the stick-slip behavior is more pronounced for cotton fibers compared to other textile fibers with circular cross-sections. They noted that the larger stick peaks for cotton fibers are mainly due to the natural twists of the ribbon-like structure of a cotton fiber, such as convolutions and reversals. While these natural twists cause relatively high-energy static friction between fibers, once the slip occurs they reduce the mean dynamic friction by decreasing the real contact area between the fibers. Their results showed that the large static inter-fiber friction of cotton fibers can be the principal driving energy for fiber travel during cotton processing under low normal forces.

Hertel developed an apparatus to measure the dissipated energy in a large assembly of cotton fibers. In this method, the fiber mass is subjected to alternating shearing forces [78]. The total energy loss during the shearing action is expressed as shear-friction. The magnitude of shear friction for a sample of cotton fibers depends upon various factors such as number of fibers in the assembly, fiber convolutions, fiber orientation, degree of entanglement, fiber crimp, length, fineness, diameter, and inter-fiber friction. Hertel investigated the relationship between shear-friction and other fiber physical properties of 28 different cotton bales [89]. He found a high negative correlation between mean shear-friction and both fiber upper-half mean length and mean bundle strength. He concluded that assemblies consisting of longer fiber not only tend to be stronger but also have lower shear-friction.

Fiber cohesion is defined as the resistance to separation of fibers in contact with one another. Similar to the shear-friction, this property of bulk fibrous assemblies depends on the combined effects of various fiber physical properties, including inter-fiber friction. The fiber cohesive force in cotton slivers can be quantified with the ASTM standard D 2612. With this technique, a known mass of cotton sliver is pulled in an axial direction, and the resisting forces are recorded with a tensile tester machine [84]. Another technique to measure the fiber cohesion is to use a RotorRing instrument [82, 83, 90, 91]. The RotorRing device was originally designed to simulate different operation processes in a rotor-spinning machine. Its working principle is as follows. First, a known mass of a fiber sliver is fed to the device. Then an opening roller, which can rotate up to 3000 RPM, separates fibers from the sliver and drags them against the interior surface of a metallic casing that covers the entire opening mechanism. The energy consumed by the opening roller to separate the fibers from their bundle is called the opening energy. In a RotorRing instrument, the opening energy is measured with a torque system that is attached to the main axis of the opening roller. It is reported that, at low RPMs, the dissipated energy is mainly due to the magnitude of forces required to overcome fiber-to-fiber friction during opening action. At higher RPMs, there are more interactions between fibers and the metallic casing because of larger centrifugal forces; therefore, the dissipated energy is mainly due to the fiber-metal friction. In the next step, the individualized fibers are transported from the opening roller to the inside of a rotor with an air suction system. The rotor rotates at ~10000 RPM. Due to the great centrifugal forces in this stage, fibers are condensed into a narrow assembly of parallel fibers

(known as the fiber ring) inside the rotor wall. The thickness of the produced fiber ring is an indicator of the degree of fiber cohesion and the opening propensity of the sample fibers. Ghosh et al. used a RotorRing to study the relationship between fiber cohesion and crimp for synthetic fibers [91]. Their results showed that the higher the crimp measurement, the lower the fiber ring thickness. That is, fibers with higher crimp per unit length were more cohesive and had lower opening propensity. Their results on the opening energy of the fiber samples showed that more energy was required to open samples with higher crimp measurements; In general, fibers with higher crimp were characterized with larger fiber-to-fiber and fiber-to-metal friction. El Mogahzy et al. investigated the relationship between the opening propensity and the NIR wax content of cotton fibers using a modified RotorRing instrument [82]. They found an inverse correlation of -0.74 between these two variables, meaning that cottons with higher wax content required less energy for opening. Gamble examined the effect of surface electrolyte treatment of cotton fibers on fiber-to-fiber friction [83]. He reported that any surface electrolyte treatment increased both fiber-metal and fiber-to-fiber friction.

As previously mentioned, fiber crimp affects overall frictional properties of fiber assemblies. Lewin et al. compared the crimp behavior of two cotton varieties: Deltapine 15 and Acala 1517 [92, 93]. They measured both the geometrical waviness of fibers and the specific energy required to remove the crimp from them. They concluded that Deltapine fibers were more significantly crimped at the 1% level of confidence. They also measured the force required to separate a fiber from the lot. The results showed that Deltapine fibers were more entangled since the force required to separate them was

significantly higher on average. Alexander et al. studied the crimp recovery of the same cotton varieties [94–96]. They reported that the crimp recovery of fibers after multiple extension cycles consisted of both the immediate elastic recovery part and the irreversible part. Their results showed that the amount of the stable part of cotton crimp varies significantly between varieties. While the Deltapine fibers recovered about 50 percent of their initial crimp after extension and relaxation, the Acala variety fibers recovered only 25 per cent of their initial crimp.

In a recent study, the influence of the surface topography on the mechanical interlocking between cotton fibers and a metallic surface was studied [85]. The mechanical interlocking took place in both directions when the ratio between the height of surface asperities on the metallic surface, *h*, and the radius of cotton fiber, *r*, exceeded one. However, the mechanical interlocking occurred in only one direction when the ratio *h/r* was slightly less than one. According to this paper, no mechanical interlocking took place when the ratio *h/r* was reduced to the lower values. This study shows the importance of surface topography on sliding friction experiments of cotton fiber assemblies.

Macroscale friction largely depends on the physical properties and environmental conditions of the counter faces during relative motion. Since real surfaces are rough, macroscale friction always involves the complex interactions between the multi-asperity contacts of both contacting surfaces on length scales ranging from molecular to macroscopic. Quantifying the number of asperities in contact and monitoring their deformation are difficult to achieve in practice. For these reasons, macroscale friction

results are often unclear and may not be the best tool for fundamental research on interfacial forces and friction. The next sections provide a literature review on the subject of single asperity contact experiments on polymeric and biological substrates.

Surface Characterization of Viscoelastic Materials with AFM

Microscale friction: its relationship with rheological properties

Recent friction theories have been established based on molecular dynamics simulations of atomically smooth surfaces in contact. During the last two decades, the invention of surface force apparatuses (SFAs) [97] and Atomic Force Microscope (AFM) [98] marked a big step forward in such studies by providing precise measurements of both the contact area and the relative separation distance between the two surfaces. Since the contact area in this type of friction experiments is in the sub-micrometer range, these techniques are often referred to collectively as interfacial single-asperity nanotribology [99–104]. A systematic nanotribological experiment avoids the complexity of multi-asperity contact interactions. This new area of study has led to the fundamental understanding of friction forces at the molecular level [55, 105, 106].

The AFM has been widely used to measure interfacial frictional forces between a probe tip and a surface. The design of the AFM has been reviewed extensively elsewhere (Figure 2) [99–101, 103, 105]. Briefly, the AFM probe consists of a sharp tip (radius of curvature varies between ~8 and 500 nm) attached to a cantilever with a low spring constant. Rectangular cantilevers are typically 225 μm long and 35 μm wide. In the contact mode AFM, as the tip approaches a sample surface, it raster scans the surface, using a piezoelectric scanner. Based on the stiffness of the cantilever, scanning can be

performed under a range of normal loads from nano- to micro-newtons. In the case of nominally flat surfaces, the friction force between the surface and the tip during sliding is the only cause of the lateral torsion (or twist) of the cantilever. The cantilever torsion deflection is on the order of several mrads and is precisely monitored by reflecting a laser beam off the back of the cantilever and a position-sensitive photo-detector (PSPD) sensor. Therefore, the lateral deflection of the cantilever, with respect to the plane of the sample surface, produces a signal corresponding to the interfacial friction between the tip and the surface. In order to convert this torsion signal to the absolute friction force, one should first measure the lateral torsional sensitivity of the cantilever. Absolute friction force between the AFM tip and a given surface can be determined with the following equation:

$$F_f = \Delta V \times S \times k_t \quad (17)$$

where ΔV is the torsional signal-difference (obtained from trace and retrace scanning directions) in volts, S is the cantilever torsional sensitivity in volts/meter, and k_t is the cantilever torsional spring constant in newtons/meter.

Determining the cantilever torsional sensitivity is a difficult and time-consuming task. Meanwhile, the torsion signal is still being reported in most scientific publications as an indication of friction forces between the AFM tip and a surface. In the case of comparative studies between different materials, it is recommended that the same AFM tip to be used for all measurements. This practice reduces the variability that may arise due to the variation in cantilever sensitivity and tip radius of curvature. During the AFM contact mode imaging of a surface, the process of raster scanning a surface produces a

high-resolution image of the spatial distribution of interfacial friction. This approach is known as lateral force microscopy (LFM) or friction force microscopy (FFM). The nanotribological properties of nominally flat surfaces such as silicon-based materials, gold, diamond, sapphire, mica, graphene, and atomically thin lamellar materials have been extensively studied. The AFM experiments along with molecular dynamic simulations on these well-defined surfaces have improved our understanding of the influence of various physical phenomena, such as surface roughness, stick-slip behavior, wear, and asperity interlocking, on friction [101–103, 105, 106]. The nanotribological, wear, and stability properties of smooth surfaces coated with Langmuir-Blodgett monolayers and thin organic lubricant films have been also investigated [107, 108]. The AFM results on self-assembled monolayers have shown that packing density, layer thickness, chain length, and chemistry of constituent molecules significantly affect the friction of coated surface.

Several studies have been conducted to measure the microscale frictional properties of rough polymeric surfaces and study their relationships with local rheological parameters [109–114]. In the case of rough surfaces, not only the friction forces between the AFM tip and the surface, but also the local slopes of the surface and the plowing of the soft surfaces during sliding can cause a lateral torsion of the cantilever. However, the shear stress between the tip and the surface still has a major effect on the cantilever torsion. For polymers, generally speaking, single asperity frictional forces are largely influenced by the extent of their internal molecular relaxation, which manifests itself in viscoelastic energy dissipative characteristics of the polymer. Here, some applications of the AFM only in the study of polymer surfaces nanotribology will be reviewed.

Nanoscale friction measurements can be used to study the surface structure and molecular conformation of polymer crystals. Nisman et al. measured surface frictional forces on single lamellar crystals of poly(oxymethylene) (POM) [115]. The results showed that the magnitude of frictional forces changed depending on the direction of AFM scanning. This observation revealed an anisotropic nature of friction at the surface of different folded domains of single POM crystals. The anisotropic effect was attributed to the presence of directionally ordered chain folds and chain loops at the surface of different folded domains. Bhushan et al. measured nanoscale friction of PET films and investigated its relationship with surface roughness, stiffness, and macroscopic friction values [116]. Their results showed a lower coefficient of friction for nanofriction than macroscopic friction, mainly because of a lesser plowing effect with nanoscale single asperity friction measurements. Cho et al. measured nano- and macroscale frictional properties of PET, PP, and HDPE films [117]. Their results are in agreement with previous studies, reporting lower values for friction at nanoscale compared to macroscale. Kumar et al. studied the effect of adding TiO_2 nanoparticles on nanotribological properties of high density PE (HDPE), linear low density PE (LLDPE), and low density PE (LDPE) polymer blends [118]. The resulting nanocomposite films exhibited higher stiffness and a lower nanoscale friction coefficient. Tambe et al. studied the scale dependence of friction on polymer surfaces [119]. They measured friction over 2 μm to 25 μm length scales and reported lower coefficient of friction at smaller length scales. They reported that friction is highly influenced by the surface roughness of contacting bodies and its

scale dependence originates from the variation in the surface roughness over different length scales.

Bogdanovic et al. mounted a cellulose colloidal microsphere, with an approximate diameter of 30-50 μm, to the tip of an AFM cantilever [120]. This technique allowed them to quantify the interfacial friction for a cellulose microsphere sliding against silica and chemically modified silica surfaces. Using both the Derjaguin-Muller-Toporov (DMT) and linear fits, they showed that the magnitude of frictional force is higher for the bare silica surface, which is more hydrophilic, compared to the hydrophobic methylated silica. The variation in friction between the two surfaces was attributed to the differences in their surface chemistry. The existence of polar groups and the ability of the surface to create a water meniscus around the microsphere tip were stated to be two important factors that influenced the friction. Nordgren et al. used the same approach to measure friction between untreated and chitosan treated cellulose microspheres at different pH values [121]. Their results demonstrated that the biolubrication properties of the chitosan layer were significantly increased at lower pH—mainly due to its high surface charges in low pH values.

Morphological and nanotribological properties of different components of thin gelatin films have been investigated [122]. The plot of frictional force versus applied load, along with the AFM force-distance data, showed that a thin gelatin is composed of two structurally different regions: a "first layer" of continuous high-friction and low-stiffness film; and a "second layer" of low-friction and high-stiffness islands. It was stated that cross-linking and intramolecular folding of the gelatin chains constrained the molecular

relaxational freedom and reduced the viscoelastic dissipation characteristics of the polymer network, resulting in lower single asperity frictional properties and stiffer substrate.

Repeated raster scanning at nonperturbative normal force and high velocities gradually elevates the temperature of the scanning region. A cumulative effect of friction-derived heating substantially increases the frictional forces of the substrate until it reaches a dynamic equilibrium. The role of frictional heating on phase transformation of crystalline and semicrystalline components of a gelatin film has been studied [123]. It was shown that a crystalline polymer tends to transform directly from glassy state to melted under nonperturbative frictional heating, while the semicrystalline polymer first passed through a rubbery phase before melting. Resting the polymer film at room temperature allowed the frictional heated region to relax toward the ground state.

Scan-velocity dependency of frictional forces on gelatin films have been investigated [123, 124]. Velocity dependency of friction seemed to be well-correlated to the different molecular relaxation peaks of a tangent delta plot (tangent delta indicates the relative contribution of viscous and elastic properties to the viscoelastic moduli of a material in Dynamic Mechanical Analysis (DMA) experiments as a function of time and temperature). While the tests were performed in decreasing scan velocity order, the larger friction force in very high scan velocities (> 300 μm/s) was assigned to the secondary molecular conformation peak (β relaxation process) in the tangent delta plot. An increase in frictional force at lower scan velocities (< 100 μm/s) was attributed to the glass transition peak (α relaxation process). A similar type of research has been

performed to investigate the velocity dependency of frictional forces as a function of molecular weight on monodisperse and polydisperse polystyrene (PS) films [125, 126]. The results are in agreement with previous studies; that is, magnitude of friction is proportional to the loss modulus of the polymer, which itself depends on the glassy or rubbery state of the polymer. In order to better understand the causation of frictional energy dissipation processes in polymeric surfaces, the velocity dependency of frictional forces on different polymer films such as poly(vinyl alcohol) (PVA), crystalline poly(ethylene terephthalate) (PET), and poly(vinyl acetate) (PVAc) have been tested [127]. A comparison between PET viscoelastic loss modulus and its AFM friction results indicated that the variation in frictional forces at high scan velocities is similar to the β relaxation process at high frequencies. For all other polymers used in the research, it was shown that changes in the α and/or β relaxation behaviors as a function of temperature, water content, or plasticizing have comparable effects on the velocity dependency of frictional response. Temperature dependency of frictional forces on poly(methyl methacrylate) (PMMA) and PS thin films has also been studied [128]. In this study, frictional forces at different temperatures and the corresponding tangent delta values were compared. The results revealed a good correlation between temperature-dependent changes in friction and the molecular relaxation peaks as measured by DMA. Both for PMMA and PS, frictional forces increased significantly near the glass transition temperature, due to the variation in viscoelastic loss near this temperature. Time-temperature superposition of friction on a PMMA surface has also been studied [129]. Using a temperature-controlled AFM, authors were able to perform friction tests at

different velocities for various temperatures. They constructed a master curve of frictional forces and showed that the β relaxation process shifts to the lower temperatures with decreasing the sliding velocity.

The AFM friction and wear measurements can be used to study the interfacial adhesive forces relevant to different components of nanocomposite and layered materials [130]. Using this technique, the cohesive strength and the detachment process of extracellular polymeric biofilms have been studied. Authors applied successive AFM friction tests at high contact force (50 nN) to abrasively shear and remove the biofilm from a mica surface. After calibration of friction force and conversion of the raw friction signal (volts) to the friction force (nN), they were able to develop an AFM based method to determine the cohesive energy of a volume of biofilm in units of $nJ/\mu m^3$. In another study, authors applied the same methodology on various nanocomposites and probed the bonding strength between PET matrix and different nanofillers such as graphene or clay platelet [131].

Few studies have been published on nano- and microscale friction of biological surfaces. Bhushan et al. investigated nanoscale friction of four different plant leaves in dried state: *lotus, colocasia, fagus,* and *magnolia*- [132]. According to the results, the hydrophilic leaves (fagus, and magnolia) showed a higher friction coefficient than the hydrophobic ones (lotus and colocasia). For hydrophilic surfaces, the contact area is higher due to the formation of water meniscus between the tip and the surface. Zhang et al. investigated nanoscale frictional properties of cotton fibers [133]. The nanofrictional characterization of textile fibers can be used to evaluate the performance of chemical

treatments and fiber surface modification techniques. The authors showed that the nanoscale friction coefficient increased after multiple washes in the absence of fabric conditioner. They concluded that excessive washing cycles damages the fiber surface and increases the fiber surface roughness, leading to higher friction forces between the AFM probe and fiber surface. In the presence of fabric conditioner, however, the friction coefficient decreased. Their results indicate that the nanoscale friction forces obey Amontons' law of friction.

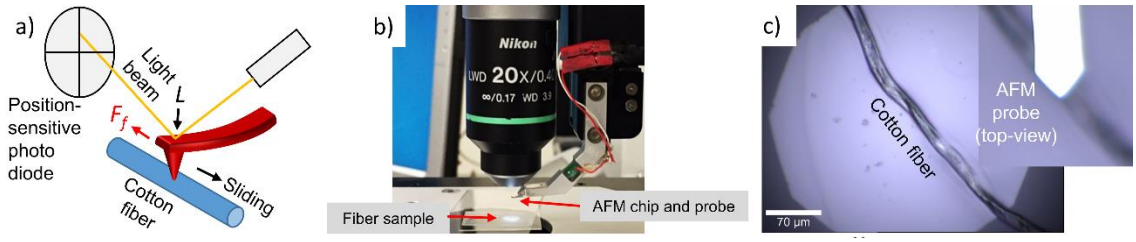

Figure 2 (a) Schematic of different AFM components, raster scanning on fiber surface; (b) AFM chip mounted on AFM head which is coupled with optical microscope system; (c) cotton fiber and AFM cantilever viewed from optical microscope

Microscale Adhesion

Various nanomechanical attributes of surfaces—such as elastic modulus, plasticity, and adhesion—can be measured by quantifying forces acting on the AFM tip as it vertically approaches a surface, slightly indents it, and finally is withdrawn from it [134, 135]. This technique has been extensively applied to quantify the surface nanomechanical properties of silicone and polymeric thin films, SAMs, nanocomposite materials, and

living cells [134, 136–140]. Nanomechanical properties of plant cell walls have been also investigated [141–143]. These studies have provided invaluable insight into the understanding of plant cell growth and development (morphogenesis). In the research reported herein, part of the focus will be on the nanoscale adhesive forces between an AFM tip and the cotton fiber surface, mainly due to the critical contribution of adhesion on the overall frictional responses of the specimen. As mentioned previously, the correlation between adhesion hysteresis and friction for polymers has been well-studied [55, 57]. Additionally, variation in surface adhesion properties has been previously utilized to discriminate between different materials.

Adhesive forces between two surfaces can be extracted from a plot of interfacial forces between the surfaces versus their separation distance, commonly known as a force-distance curve (FDC). Specifically, in the AFM technique, the FDC is obtained from measuring the vertical deflection of a cantilever (which can be converted to unit force) as a function of piezoelectric tube vertical extension (which can be converted to indentation/separation distance) when the tip is brought into contact with the sample and then withdrawn. Similar to microscale friction, the main advantage of adhesion measurements with AFM is the single asperity contact at the molecular level, which removes the ambiguity due to multiple asperity contacts. A hypothetical FDC and its different regions are shown in Figure 3. The general shape of the FDC resembles a typical non-bonding intermolecular force curve between two non-polar particles. In region A, the tip is in resting position and the net force acting on it is zero. In region 2, as the tip is driven toward the surface, at some critical distance, the forces acting on the

tip suddenly become attractive, and the tip jumps to contact. In order to accommodate the abrupt movement of the tip, the cantilever experiences an instability and bends forward (region B). By multiplying the vertical deflection of the cantilever in nm with its spring constant in N/m, total forces acting on the tip can be quantified. This sudden large attractive force acting on the tip is defined as the pull-on force and its magnitude can be explained by extent of ever-present van der Waals, electrostatic, capillary, and chemical bonding forces. In region C, as the piezoelectric tube continues to extend toward the sample surface, the repulsive forces are first detected and the net force starts to increase. This point is defined as the tip-surface contact point. After this point, the tip starts to penetrate into the sample and causes elastic and/or plastic deformation of the surface (assuming higher stiffness value for the tip). Meanwhile, the cantilever deflection gradually changes from being bent downward to upward. The indentation process continues until ultimate contact is reached at a predefined maximum upward deflection. In region D, the piezoelement movement reverses and it begins to withdraw the tip. When the tip is being retracted, it still remains in contact with the surface until the cantilever exerts sufficient tensile force to overcome the adhesive bonds formed between the tip and the surface (pull-off force). The difference between the pull-off force and the forces acting on the tip at the resting position is proportional to the adhesion force, which is significantly affected by real contact area and chemistry of the two materials. Upon the tip-sample separation, depending on its spring constant, the cantilever experiences a second instability and springs back to the resting position in region E.

There are three modes of deformation associated with the force measurement technique with the AFM: the cantilever is either bent upward, or downward, or twisted. These cantilever deformations are associated with surface stiffness, adhesion, and friction, respectively. The deformation can be converted to the forces causing it with Hooke's law. That is, the strain (deformation) of an elastic material is proportional to the stress applied to it:

$$F = k_c d_c \quad (18)$$

Here, k_c is the spring constant of the cantilever, and d_c is the deflection of the cantilever. By obtaining forces acting on the cantilever, the force-distance curve of a given material's surface can be acquired (the distance is obtained by adding the piezoelectric motion to d_c). Therefore, the force of adhesion, the stiffness of the surface, and the friction between tip and surface can be extracted from the curve. Since the invention of the AFM, one of the main challenges has been how to precisely measure the deflection of the cantilever, d_c, as the main output signal of the AFM instrument. In almost all the AFMs available on the market, the deflection of the cantilever is measured with the optical lever technique. In this method, a beam from a diode is adjusted onto the cantilever and reflects from its shiny end. A position sensitive detector (PSD) monitors the position of the reflected beam. As the cantilever bends, the reflection angle of the beam changes to twice the change of the slope at the end of the cantilever. Therefore, the deflection of the cantilever can be measured as [134]:

$$d_c = \frac{Fl^3}{3EI} = \frac{\Delta_{PSD} l}{3b} \quad (19)$$

Here, l is the length of the cantilever, I is the moment of inertia of the cantilever, E is the Young's modulus of the cantilever, F is the force acting on the cantilever, Δ_{PSD} is the distance the laser spot moves on the PSD, and b is the distance between the PSD and the end of the cantilever. In the optical lever technique, the Δ_{PSD} is the only output of the instrument. This output is used to calculate d_c, the deflection of the cantilever, the variable of interest. Other disadvantages of AFM and possible sources of error include the possibility of contaminating the tip during scanning and lack of standard procedure to examine the true radius of curvature of the tip before performing nanomechanical testing.

Different aspects of the adhesive force measurement technique with the AFM have been reviewed and studied. Batteas et al. studied the adhesion and wear of colloidal silica nanoparticles at different pH values. In order to simulate the actual particle-particle interaction, they used AFM probes with a blunt tip (curvature radius of ~ 50 nm). They showed that the tip-particle adhesion, as measured by the JKR contact mechanics, is higher at low pH values [144]. Burnham et al. attempted to model the magnitude of attractive forces between the tip and surface using magnetic, electrostatic, and van der Waals interactions [135]. For uncharged and non-magnetic surfaces, they concluded that the effect of van der Waals forces on the tip is often masked by the longer-range attractive forces which are better explained by capillary, fixed dipole, and patch charge models. Kawai et al. measured the pull-on and pull-off forces for eight reference surfaces [145]. They showed that the pull-off forces were well correlated with the adhesion energy of the reference samples as measured from contact angle experiments. Mate et al.

utilized the shape of the pull-on region of the FDC to estimate the thickness of the ultrathin polymeric liquid films (less than ~ 300 Å thick) on a flat silicon surface [146, 147]. Using this technique, they were able to map the spatial distribution of the film thickness coated on the surface. Bhushan et al. performed an adhesive force measurement study on the 2 nm thick lubricant layer film [148]. They concluded that the magnitude of meniscus forces between the tip and the lubricant layer, which manifested themselves in the corresponding pull-off force, was proportional to the film thickness. The dependence of adhesion on both surface topography and nanomechanics has been widely investigated. Mizes et al. demonstrated that the local curvature of the surface affects the adhesion between the AFM tip and the surface [149]. This observation was explained by the fact that a real contact area was much lower for contacts in the apex of an asperity compared to that of in the bottom of a pit. Sirghi et al. modeled the capillary and interfacial tension forces between an AFM tip and a substrate based on the local radius of curvature of the asperity (positive value for a convex curvature, and negative for a concave curvature) [150]. Their analytical solution demonstrated that the capillary forces were much larger for concave surface curvature. Eaton et al. investigated the capability of the adhesive force measurement technique to discriminate between different domains of polymer blends based on their surface energetic and nanoscale stiffness [151]. The adhesive force measurement results on PDDMA/PMMA thin films demonstrated that the average force of adhesion was much higher for PDDMA-rich domain compared to PMMA regions, mainly due to its higher surface deformation and, consequently, greater tip-sample real contact area [152, 153]. Begat et al. glued pharmaceutical micro-particles from various

inhaler formulations to a tipless cantilever and measured the adhesive forces between them and a reference substrate with well-defined surface texture [154]. Using this technique, they were able to quantify the inter-particle cohesive-adhesives forces and predict the bulk properties of the bulk powder formulation.

A positive strong correlation exists between the adhesion hysteresis and frictional forces [55, 57, 58]. Adhesion hysteresis is defined as the difference between the work needed to separate two surfaces (unloading) and that originally gained on bringing them together (loading) [155–157]. Tirrell investigated the adhesion hysteresis of various polymeric materials [157]. For hysteretic surfaces, such as polymers, the effect is attributed to both the reorientation of molecules near the surface and the viscoelasticity of the bulk material. Since a certain level of molecular rearrangement and transformation may take place after contact is made, only the loading data can be fit to the JKR model for the analysis of real contact area. The contact formation during loading is governed by the chemical constituents of the contacting materials.

Appropriate selection of an AFM probe is a crucial task for successful nanoscale adhesion and friction experiments. Generally, there are two important probe parameters which restrain the magnitude of the applied pressure to the surface: cantilever stiffness and tip apex radius. Cantilevers with low spring constant are more efficient in the study of adhesive properties of soft materials, since the pull-off deflection is higher for flexible cantilevers. Stiff cantilevers, on the other hand, are mostly used for indentation purposes. With regards to the radius of curvature of the tip, large radius tip probes are more favorable than sharp tip probes in the study of polymeric and biological substrates. The

larger contact area for these tips provides the following advantages. (i) The total interaction force between the tip and the surface is higher; as a result, the sensitivity to adhesion and friction forces is maximized. (ii) The applied pressure is lower; therefore, the penetration depth will be limited to a few nanometers. (iii) The stress concentration in front of the tip is lower, reducing the plastic deformation and surface damage in testing of compliant thin films. (iv) The probability of non-normal indentation is minimized since the local friction between the tip and the surface is enhanced (the indentation process occurs approximately perpendicular to the surface). (v) Finally, the spherical shape of the apex of the tip simplifies the implementation of the contact mechanics analysis.

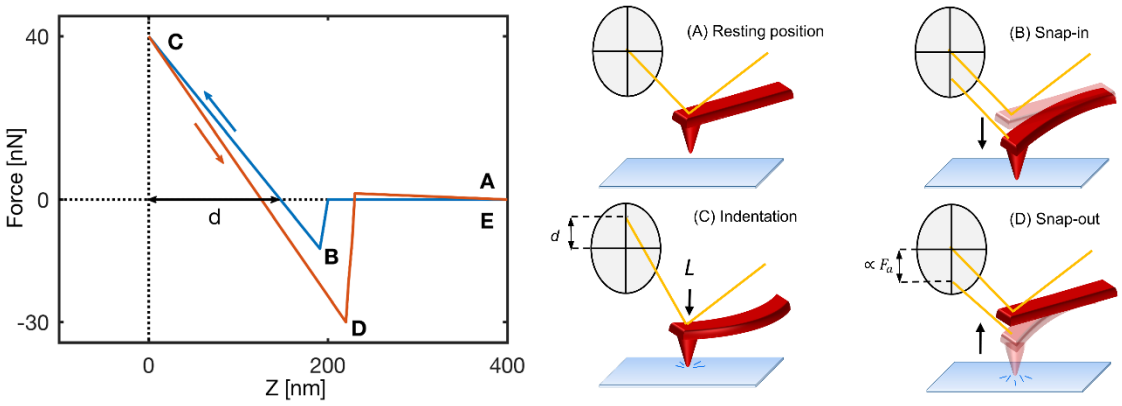

Figure 3 Hypothetical force-distance curve and its different regions.

Successive measurements of FDCs across the specimen surface can be used to generate a map of local adhesion, where each pixel represents a magnitude of the tip-sample adhesion force of that area [158]. Lately, a new FDC mapping technique has been

developed, known as pulsed-force microscopy, with the capability to produce high-resolution topography and nanomechanical properties images simultaneously [159, 160]. With this method (commercially known as the Peak Force Tapping mode), as the piezoelement raster scans the surface, it also resonates at very high frequencies. During each resonance cycle, the tip engages the surface and then is retraced from it at a given amplitude; thereby, hundreds of FDCs can be produced in matter of milliseconds [161, 162]. This AFM mode has gained increased popularity in the field of surface characterization of biological materials [163, 164].

Surface Characterization of Plant Cells and Cotton Fibers

Plant cells are covered with a thin extracellular membrane, known as the cuticle, which strengthens the overall structural stability of the cell and preserves its physiological integrity [165–167]. In the study of plant cell morphogenesis, precise measurements of the nanoscale mechanical properties of plant cell surfaces are crucial for investigations on the role of cuticle biomechanics in a cell shape changes and growth rate [141, 168]. The cuticle thickness varies significantly between different plant organs and species and also during cell development. This plant cell outer layer is a hydrophobic multicomponent structure and mainly consists of the biopolyester cutin, various lipid-derived compounds or so-called waxes, and pectins. Cutin is an insoluble biopolymer network makes up of C_{16} and C_{18} fatty acid monomers cross-linked by ester bonds. Cutin encompasses $40 - 80\%$ weight of the cuticle and can be submicron to $10\ \mu m$ thick. Cuticular waxes are chiefly composed of n-acyl alkane derivatives with chain length of C_{20}-C_{40}. Plant cell waxy components mostly travel through different layers of the

cuticular membrane and build up on the outermost layer of the cuticle. After deposition on a plant organ surface, they self-assemble into a thin continuous lipid-film. They form various crystalline microstructures, such as tubules ($0.3 - 3$ μm long and $0.1 - 0.3$ μm wide), platelets, and rodlets. Cuticular waxes directly affect interfacial bioprocesses and environmental interactions of plant organs. Self-assembly and growth of wax crystals has been monitored with AFM time-series images [169]. These observations showed that the morphology of wax crystals depends on the growth conditions, such as temperature and moisture content, the chemical composition of lipid compounds, and the structural template effect of the underlying substrate. Pectin polysaccharides can also be found in the outer surface of the cuticle. Round et al. studied the structure of individual pectin macromolecules extracted from green tomato fruits, using the AFM [170, 171]. Their work demonstrated the capabilities of AFM images in revealing molecular weight, length, branching, and aggregation of individual pectin polymers.

Even with recent advances in AFM techniques, quantifying the local nanomechanical attributes of soft biological membranes is a challenging subject. Often, due to the natural surface roughness and viscoelasticity of biological materials, accurate measurements of surface nanomechanical properties require an implementation of sophisticated contact mechanics models. Studies have been conducted to examine the surface biophysical behavior of cutin films, isolated from the cuticle of tomato fruits, with AFM [172–174]. Round et al. studied the effect of moisture content on the rheology of such films [173]. They reported that the surface elastic modulus, as obtained by fitting the FDCs with the Hertz model, decreases with increasing water absorption in a highly nonlinear fashion.

They concluded that the cutin film has a rubbery characteristic and water molecules increase its polymer chain mobility.

A fully developed cotton fiber is composed of five different layers: the cuticle, the primary cell wall, the winding layer, the secondary cell wall, and the cell lumen [175]. The cotton fiber cuticle is mostly made of lipids, alcohols, and fatty acids. These compounds are collectively called "cotton waxes" [176]. The cotton fiber cuticle also contains some portion of pectins [177]. Due to the presence of waxes and pectins in the cuticle, untreated native cotton fibers are hydrophobic [176]. The waxy layer is about 200 to 300 nm thick [175]. Cotton fiber wax content varies significantly among different varieties. Various studies have reported a strong positive relationship between cotton fibers wax content and their surface area [82, 178–181]. El Mogahzy showed that the frictional properties of cotton fibers are influenced by their wax content [82].

In the research reported herein, surface characteristics of different varieties of cotton fibers are investigated with AFM. Previous studies have successfully utilized various AFM operation modes to image both the surface and the cross-section of cotton fibers [182–185]. These studies obtained high-resolution AFM images of cotton fibers in tapping mode to study the geometry of cellulose microfibrils embedded inside the internal structure of fibers. As already mentioned, Zhang et al. investigated the nanoscale frictional properties of chemically treated cotton fibers [133]. However, no attempts have been made to study the variation of surface nanomechanical properties of cotton fibers, such as their Young's modulus and pull-off force, among different varieties. One of the surface characteristics of cotton fibers, which is compared across different varieties in

this work, is adhesion or pull-off force. As previously discussed, the nature of the adhesion forces probed with the AFM is complex. The magnitude of the adhesion force depends on topography of the surface, capillary forces, and surface energy characteristics of the tip and the surface. It can be assumed that the magnitude of adhesion force on the cotton fiber surface might be attributed to the thickness of the waxy layer. As the AFM tip approaches the fiber surface, sudden contact is made with this lipid layer. As the tip further approaches the fiber surface, it may penetrates into the waxy layer until it reaches an ultimate depth of contact. As the tip is withdrawn from the surface, a pull-off force is needed to break the lipid meniscus between the tip and the fiber surface. Due to the hydrophobicity of the waxy and pectin compounds on the fiber surface, the formation of the water meniscus is not likely in AFM adhesion experiments. Therefore, it can be assumed that the force required to break the lipid meniscus increases as the thickness of the lipid layer on the fiber surface increases. Also, upon applying proper contact mechanics models, it will be possible to estimate the work-of-adhesion and the estimated contact area between the probe and fiber for different cotton varieties.

Objectives

To Determine Friction Differences from Different Varieties

As previously mentioned, the main mechanism governing fiber-grid bar and fiber feed-plate interactions at the lint cleaning process is friction. Frictional forces that take place between grid bars and fibers can cause fiber breakage and damage. In fact, fiber tufts with higher surface roughness incur higher frictional force; therefore, they are more susceptible to break at this processing stage. The first objective of this research is was to

study the variability of frictional properties of ginned cotton fibers across different varieties. One of the most important fiber properties that might affect cotton fiber friction is maturity. In this study, fiber maturity will be isolated so that the effects of cotton fiber surface related properties on fiber friction can be analyzed. Variation in fiber maturity is mainly due to the dissimilarity in cotton growing conditions and harvesting dates. For this reason, the coefficient of friction of 48 cotton varieties with the same growing conditions and harvesting date are measured. The variation of fibers frictional properties across different varieties is analyzed with the one-way ANOVA test. Results from this part of the study can help breeders in selecting for development those cotton varieties that are associated with higher processibility and more damage resistivity.

To Investigate Correlations between Friction and Fiber Physical Properties

The second objective of this study was to measure the frictional properties of different cotton samples and investigate their relationship with other physical attributes of fibers. This was achieved by conducting standard sliding friction experiments on cotton slivers from five cotton samples. Other physical properties of cotton slivers were measured with Advanced Fiber Information System (AFIS) and High Volume Instrument (HVI). Simple and robust multiple linear regression analysis will be applied to study the relationship between the parameters.

To Model the Real Contact Area of Cotton Fiber Assemblies

In order to explain possible relationships between salient fiber geometrical features (length, radius, and maturity) and the friction of fibrous assemblies, a mathematical model was developed to compute (i) the number of fibers within a fiber assembly and

(ii) the contact area that it makes with a stiff, nominally flat surface. This model allows explanation of the hierarchical internal structure of a fibrous assembly that controls to some extent the macroscale frictional properties of the assembly. The ultimate goal was to develop a 3D space representing the set of all possible fiber geometrical features where every point in this space corresponds to a distinct contact area of the fibrous assembly based on the selected fiber structure measures.

To Evaluate Fiber Surface Friction at the Nanoscale

Previous studies have shown that the surface characteristics of cotton fibers significantly affect the frictional properties of their bulk. The objective here was to compare the nanoscale surface deformation, adhesion, and friction of fibers from two different cotton varieties, using various modes of AFM. The single asperity adhesion/friction of the cuticle layer under nonperturbative normal force can be explained by the local nanoscale stiffness, resiliency, and the plowing effect of the membrane biopolymer.

CHAPTER II

SOLUTION PROCEDURE

Materials Description

Cotton Card Sliver Samples Used for Macroscale Studies

Two sets of experiments were conducted, one on assemblies of aligned cotton fibers and the other on assemblies of randomly oriented fibers. For the first set, five highly characterized fiber samples were selected based on their diversity in fiber physical properties as evaluated by USTER® High Volume Instrument (HVI) 1000 instruments. The samples were in the form of card sliver. In a standard staple yarn manufacturing process, card sliver is a product of a carding machine. Carding machines comb fibers and brush them into a thin, low-density, web-like, fibrous structure. By passing the very wide web through a narrow nozzle, the web takes the form of a loose assembly of approximately parallel fibers, commonly called the card sliver. The average width of the card sliver used in this study was roughly 3 cm.

Cotton Varieties Used for Macroscale Studies

Samples used in the second set of experiments were collected from national and regional standard varieties from the Lamesa, TX location of the National Cotton Variety Testing program (NCVT) in 2014. The standard varieties, Deltapine 0912 B2RF, FiberMax 2484B2F, PhytoGen 499 WRF, PhytoGen 725 RF, FiberMax 2011GT, Stoneville 4946GLB2, All-Tex Nitro B2RF, NexGen 1511 B2RF, and Deltapine 1044 B2RF were included in a 48-entry variety performance field test. The field test was planted May 22, arranged in a randomized complete block experimental design, with

four blocks of two-row plots (measuring 2.0 m by 9.1 m). The soil type was Amarillo Fine Sandy Loam (Fine-loamy, mixed, superactive, thermic Aridic Paleustalfs), and 23 cm of irrigation water was applied in-season with center-pivot low-energy precision application irrigation. A 10-34-0 (*ie.*10 *wt* % N, 34 *wt* % P, and 0 *wt* % K) fertilizer was applied pre-plant, and 32-0-0 (*ie.* 32 *wt* % N, 0 *wt* % P, and 0 *wt* % K) was applied in-season through the center pivot. Plots reached maturity with over 90% open bolls on October 21, and a 150-random boll sample was harvested from two replications of each standard variety. Bolls were snapped from the plant by hand with burr intact. Boll samples were deburred with a two-saw cylinder stick machine and feeder-extractor at the Texas A&M AgriLife Research and Extension Center in Lubbock, TX (LREC) and ginned on a ten-saw Continental Eagle lab scale gin, after being cleaned on a Lummus 900 II incline cleaner. The lint was then cleaned with a Moss cleaner and condenser. The fiber samples covered a broad range of the variability that exists in cotton fiber physical and mechanical properties (Table 1). They also comprised a set of samples with varying genetic traits but similar growth conditions in terms of environment and management, thus minimizing to the extent possible the variability in fiber maturity among the samples.

Table 2 Summary of fiber quality measurements for the 48 bulk fiber samples.

Fiber quality parameter	Mean	Median	Minimum	Maximum
Micronaire	4.34	4.3	3.7	5.05
Bundle length [cm]	2.8	2.8	2.5	3.0
Bundle strength [g/Tex]	31.3	31.4	25.8	35.35
Bundle elongation [%]	7.6	7.75	5.85	10.25
+b	9.3	9.4	8.05	10.45

Cotton Varieties Used for Nanoscale Studies

According to the results from the first section of this study, a significant difference between the fiber friction means of samples B and C was observed at 1% level of confidence. Random subsamples of eight fibers were taken from samples B and C for further surface mechanical analysis with the AFM.

Experimental Procedure

Equipment Used

Friction Tester Apparatus and the TA.Xtplus Texture Analyzer

The sliding friction force of fiber specimens was determined with a friction tester apparatus mounted firmly on the lower frame of a tensile testing machine (TA.XTplus Texture Analyzer). The apparatus consisted of a 40 x 70 x 0.4 cm polished steel plane and a low-friction pulley. In order to study the effect of the apparent contact area on friction, three different rectangular sleds with areas of 15, 20, and 30 cm^2 were designed.

These sleds were aluminum sheets, bent at their leading edge, which carried the fiber against a nominally smooth and stiff metal surface. An eye screw was fastened to the bent end of each sled, allowing the attachment of stiff nylon string to the sled. The other end of the nylon string, after passing it through the pulley, was attached to the upper gauge of the tensile testing machine, which was equipped with both a driving mechanism and a load cell. Total weights of the sleds were 20, 25, and 36 g respectively. For each experiment, the sled was pulled for 10 cm at a constant velocity of 1 cm/s. At the end of each experimental run, the mean kinetic friction force (the force required to sustain the uniform motion of the sled) was recorded by the instrument's software. A new fiber specimen was used for each run.

The USTER® Advanced Fiber Information System PRO 2

Fiber dimensional properties of the five card sliver samples were examined with USTER® Advanced Fiber Information System (AFIS) PRO 2. In AFIS, a loose assembly of roughly parallel-oriented fibers were gently placed inside the vertical, narrow tubes on the top of the instrument. A fiber specimen prepared for the AFIS instrument weighs ~ 0.5 g and consists of roughly 8,000 fibers. In each AFIS run, one specimen was fed into the instrument. A sophisticated fiber individualizer mechanism separates impurity particles from the fiber specimen and individualizes the it into single fibers. An airflow system guides the individualized fibers and impurity particles through different nozzles where they pass through various optical sensors. These sensors measure main fiber dimensional properties such as length, maturity, and fiber diameter.

The instrument also reports additional statistical parameters estimated from the distributions of these fiber properties.

The USTER® High Volume Instrument

The HVI is a device relied upon by the U.S. government for classification of cotton fiber samples based on their prominent physical properties such as length, strength, color and linear density. It is a semi-automated machine composed of three modules. In the first module, it produces an array of approximately parallel fibers and measures their mean length and strength. In the second module, it measures the reflectance properties of the bulk fibers using an imaging system. In the last module, it measures the Micronaire value of a sample—an estimation of fiber linear density—a measure of the air permeability through a known mass of compressed cotton fibers.

The Tescan Vega-3 SEM

The projected width of fibers was precisely measured with the Tescan Vega-3 Scanning Electron Microscope (SEM) with an operating voltage of 20 kV.

The Bruker Dimension Icon AFM

Bruker's Dimension Icon AFM was used in this study to conduct surface nanomechanical and friction experiments.

Sample Preparation

Sample Preparation for Macroscale Studies

For each macroscale friction experiment with card sliver samples, a fiber specimen with a length of 5 cm was separated from the card sliver samples. Due to the approximate parallel orientation of fibers within the card sliver structure, specimens

exhibited different frictional characteristics in their respective principal directions due to anisotropy. In order to reduce the amount of stick-slip behavior, specimens were attached to a sled with small clips, with their constituent fibers oriented parallel to the travel direction of the sled. For friction experiments on the 48 raw fiber samples, 0.6g of fibers were pulled from bulk samples and attached to a sled in pre-existing random orientation.

Sample Preparation for Nanoscale Studies

During the AFM experiments, one end of a fiber was fixed to a microscope glass slide with a thin layer of glue. After the glue dried, the fiber was gently stretched with tweezers to remove its natural crimp. While the fiber was extended, multiple thin droplets of glue were applied the other end of the fiber. The distance between the two fixed points along the fiber length was ~10 mm. This technique ensured that the fiber was firmly immobilized on the glass slide and prevented any possible drift or creep of a surface during the AFM raster scanning. Special care was taken to make certain that the height of glue mass did not exceed the height of a fiber to avoid any contact between the probe tip and dried glue mass. This technique was found to be more efficient than the double-sided adhesive tape technique which can cause tip contamination during the interaction of a tip with adhesive substrate.

Protocol

Modeling the Real Contact Area of Cotton Fiber Assemblies

Counting the number of fibers within a known fiber mass is impractical, and measuring the real contact area the fiber assembly makes with a flat surface is virtually

impossible. Nevertheless, evaluation of these two parameters is crucial for proper analysis of frictional behavior of fibrous assemblies. Both parameters could potentially be determined by fiber dimensional factors such as length, diameter, and maturity, but one should also consider the effects of the mechanical properties of fibers. To model the two parameters of interest, a MATLAB function was created which takes the mass of a given fiber assembly, its thickness, the fiber length, maturity, and diameter distribution as inputs and returns (i) the number of fibers in the assembly and (ii) its contact area under maximum elastic deformation. The first assumption in the model was that all simulated fibers are made of 100% cellulose. This assumption is close to reality, as a typical cotton fiber is made of ~95% cellulose. Therefore, the input mass of fiber in g was converted to the total volume V in cm^3, using the reference cotton fiber cellulose density value of 1.5 g/cm^3 [186]. The second assumption was in regard to the fiber geometry; it was assumed that a hollow cylinder can denote fiber cells in their original state, before the cotton boll opens. Therefore, the cylinder external radius R represents the fiber radius, the internal radius r represents the lumen radius, and the length l represents the fiber length. After the boll opens, the water inside the lumen evaporates and the fiber becomes a hollow tube. As this occurs, due to tensions inside the fiber structure, the fiber flattens and twists. As a result, the fiber cross-section transforms from its original circular shape into a flat kidney-like geometry. The third assumption was that all fiber dimensional properties D_i are normally distributed with a respective mean value of μ_i and variance σ_i^2 ($D_i \sim \mathcal{N}(\mu_i, \sigma_i^2)$).

The number of fibers in a given mass of fibers was computed as follows. A hollow cylinder with parameters R_1, r_1, and l_1 was generated. The R_1 and l_1 values for a given sample were selected from its equivalent input fiber dimensional characteristic (diameter and length) distributions. The internal radius of the hollow cylinder, however, was calculated with the following equation:

$$r_1 = \sqrt{\frac{1}{\pi} - R_1^2\theta_1} \quad (20)$$

Here, θ_1 denotes the maturity level of the first fiber. The volume of the fiber v_1 was calculated by

$$v_1 = \pi l_1 R_1^2 \theta_1 \quad (21)$$

The three main characteristics of the simulated fiber and its volume (R_1, r_1, l_1, and v_1) were stored in the first row of a matrix A. More fibers were generated by iterating this process. The corresponding R_n, r_n, l_n, and v_n values of the fiber n were stored in row n of matrix A such that

$$A = \begin{bmatrix} R_1 & r_1 & l_1 & v_1 \\ \vdots & \vdots & \vdots & \vdots \\ R_n & r_n & l_n & v_n \end{bmatrix} \quad (22)$$

This process was iterated until the summation of all the simulated fibers' volume became equal to or exceeded the total sample volume V, i.e. $\sum_{j=1}^{n} v_j \geq V$. The length of matrix A corresponded to the number of fibers in the assembly of a given mass with desired fiber quality parameters.

Next, the contact area of the assembly against a given flat surface was computed. A real clump of cotton fibers resting on a flat surface is composed of randomly oriented

fibers accumulated on top of each other in three-dimensional directions in various layers. It is assumed that the fiber assembly is composed of multiple distinguishable layers. Every layer contains an equal number of fibers except the top layer, which might contain fewer. Fibers in each layer were randomly oriented in a two-dimensional space, independent of the fibers' orientation in other layers. The simulated fibers were free from any three-dimensional bending or crimp (Fig. 4(a)). In this simulation, the following mechanism for the spread of contact area of a fibrous assembly under given normal load was implemented. Initially, fibers from the first layer are in contact with the lower flat surface. After increasing the normal pressure, fibers of the first layer start to deform in the lateral (or the transverse) direction to accommodate the stress placed on them. At the same time that the fibers of the first layer are attaining their maximum elastic deformation under the applied normal force, fibers from the second layer begin to reach the flat surface to increase the overall contact area of the assembly and, consequently, support the increasing normal load. It was assumed that those sections of fibers from top layers which are crossing the fibers underneath them will flex around the lower fibers; therefore, the crossing sections of the fibers from top layers did not add any contact area to the overall contact area of the assembly (Fig. 4(b)). By this assumption, the total contact area of the assembly was computed with the union operation. That is, once we computed the contact area geometry A_i for the fiber i, the total contact area of the fiber assembly was the union of all geometries; i.e., $A_{real} = \bigcup_{i=1}^{n} A_i$.

The maximum contact area of the assembly was calculated with the following procedure. First, the maximum elastic deformation of all individual fibers in the first

layer was computed. The maximum elastic deformation of cotton fibers due to a compressive force in the lateral direction depends on various features of both their internal structure and dimensional characteristics. The combined contact areas of the fibers from the first layer formed arbitrary two-dimensional geometries. The vertices of the geometries (Fig. 4(b)), which represent the contact area of fibers from the first layer of the assembly, were stored in matrix C_1 (by plotting the matrix C_1, a two-dimensional image of the contact area of the first layer can be obtained). The vertices of the contact areas of other layers *k* were stored in the matrix C_k. A specific MATLAB function (polybool) was employed to take the contact area geometries of all layers as inputs, overlay them on top of each other, and return a matrix that contains the vertices of the overall contact area geometries as a union of all the input geometries. The resulting matrix *M* includes the vertices of all the contact area geometries from all the layers. The matrix *M* can be denoted as

$$M = C_1 \cup C_2 \cup \cdots \cup C_n = \begin{bmatrix} x_1 y_1 \\ \vdots \ \vdots \\ x_p y_p \end{bmatrix} \cup \begin{bmatrix} x_1' \ y_1' \\ \vdots \ \ \vdots \\ x_q' \ y_q' \end{bmatrix} \cup \cdots \cup \begin{bmatrix} x_1'' \ y_1'' \\ \vdots \ \ \vdots \\ x_r'' \ y_r'' \end{bmatrix} = \begin{bmatrix} X_1 Y_1 \\ \vdots \ \vdots \\ X_s Y_s \end{bmatrix} \tag{23}$$

Here, $[x_j \ y_j]_k$ represent the coordinates of a given vertex of the contact area geometry C_k in the layer *k*. In the last step, another MATLAB function was used to take the vertices of arbitrary two-dimensional geometries and return the total area of all the geometries. This final output is an estimate of the contact area of multi-layer randomly oriented fibrous assemblies as a function of different fiber quality parameters such as length, maturity, and fiber diameter. The flow chart of this algorithm is shown in Fig. 4(c). Multiple fiber assemblies were simulated, which are diverse in terms of their fiber

dimensional properties. These fibrous assemblies cover all the possible configurations in the cotton fiber length, diameter, and maturity space (Fig. 4(d)). The three-dimensional matrix *S* that contains all the contact area values as a function of *l*, θ, and *r* can be denoted as:

$$S_{\mathrm{l},\theta,\mathrm{r}} = \left[\begin{bmatrix} A_{111} & \cdots & A_{11n} \\ \vdots & \ddots & \vdots \\ A_{1m1} & \cdots & A_{1mn} \end{bmatrix} \cdots \begin{bmatrix} A_{l11} & \cdots & A_{l1n} \\ \vdots & \ddots & \vdots \\ A_{lm1} & \cdots & A_{lmn} \end{bmatrix}\right] \tag{24}$$

Another three-dimensional matrix, which contains the number of fibers in the assembly as a function of *l*, θ, and *r*, was also constructed.

The kidney-like cross-sectional geometry of individual fibers was partitioned into three sub-geometries: the main rectangle in the middle and two half circles at the ends (Fig. 4(e)). The fiber lumen flattens after the boll opens and the fiber dries out in the open air; thus the length of the rectangle (2a) is half of the lumen circumference. As the degree of fiber secondary cell wall (maturity) increases, the lumen becomes smaller. Thus, for mature fibers, the length of the central rectangle becomes smaller and the fiber cross-section shape more closely resembles a complete circle. When the simulated fiber is at rest under zero normal load, its contact area A_{real} can be obtained by multiplying the width of the central rectangle in the fiber cross-section *2a* by the length of the fiber ($A_{real}=2al$). Under the application of a load perpendicular to the main fiber axis, the fiber cross-section will deform in the transverse direction to accommodate the applied stress. This deformation depends on the Young's modulus and Poisson's ratio of the fiber. Under the cellulose elastic compressive stain of 8% and the Poisson's ratio of 0.5, the lateral strain of the fiber is on the order of $-(-8\%) \times 0.5 = 4\%$. Therefore, the length

of the central rectangle *2a* will experience a 4% increase at its maximum elastic deformation. The maximum elastic lateral strain of the fiber is denoted by *2b* and shown in Fig. 4(e). Under the application of normal stress, the half circles at the ends of the fiber cross section deform and expand their contact area according to the Hertz theory[66]. The maximum deformation and contact area of the half circles also depend on the stiffness of the fiber and their radii. Considering a compressive strength F of 40 MPa, an elastic modulus E of 4.7 GPa, a Poisson's ratio v of 0.38, and a length l of 0.03 m [72], the width of contact area of the half circle b_c as a function of the radius of half circle R_c can be calculated as:

$$b_c = \sqrt{\frac{4F(1-\nu^2)}{\pi l E} R_c} = \sqrt{\frac{4(4\times10^7)(1-.5^2)}{\pi(3\times10^{-2})(4.7\times10^9)} R_c} \approx 0.5\sqrt{R_c} \qquad (25)$$

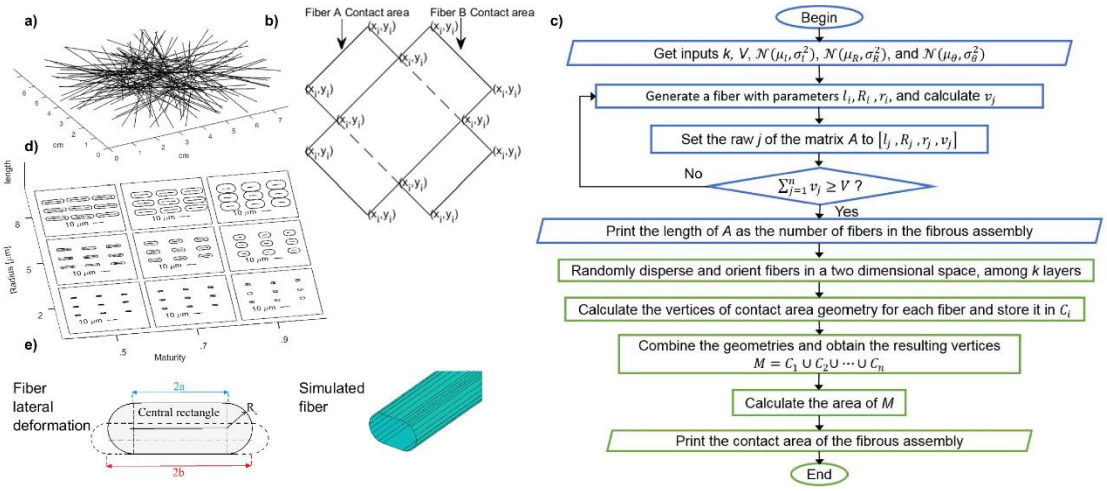

Figure 4 (a) Three dimensional view of the simulated fibers; (b) an example of contact area calculation for two crossing fibers; (c) flow chart of the algorithm used for the fiber simulation; (d) all the possible discrete points in the space of fiber length, maturity, and radius; (e) schematic of the fiber lateral deformation under compressive force

Macroscale Friction Experiments on Fiber Assemblies

Friction measurements were made on the card sliver samples under a range of normal loads (2.0, 5.0, 5.9, 7.3, 10.2, 12.2, and 15.2 N) applied by placing different weights on the sleds. For conducting friction experiments under the 2.0 N normal force, the smallest sled with area of 15 cm^2 was used. For experiments under 5.0, 5.9, and 7.3 N, the sled with area of 20 cm^2 was used. For all larger normal forces, the sled with area of 30 cm^2 was utilized. Sixty friction tests were performed under each normal load (420 total tests per sample). Once the friction data were collected, a one-way analysis of variance (ANOVA) was used to determine whether there are any statistically significant differences between the friction means at different normal loads. In order to determine which pairs of means are significantly different, multiple comparison tests were performed with Tukey's honestly significant difference procedure.

Friction tests on the 48 raw fiber samples were performed with the 30 cm^2 sled and four normal loads (5.3, 7.3, 10.2, and 12.2 N) with 45 replications under each load (135 tests per sample). The 45 number of replication was selected based on a common rule of thumb in statistics that recommends having at least 32 observations to properly fit the normal distribution to data. In general, the proper sample size to estimate the mean of a population can be calculated using the following equation:

$$(sample\ size) = \frac{(desired\ alpha\ level's\ z\ score)^2\ *\ (\sigma\ of\ the\ pilot\ study)^2}{(desired\ margin\ of\ error)^2}$$

A one-way ANOVA was performed to examine whether the samples were drawn from populations with the same mean.

In order to further investigate the relationships between fiber properties and fiber friction in a larger data set, a multiple linear regression model $Y = \beta_0 + \beta_1 x_1 + \cdots + \beta_n x_n + \epsilon$ was fitted to the data from the 48 raw-fiber samples. Input variables were standardized, and outlier effects were down-weighted with a robust fitting method (robustness of the fit was achieved by iteratively re-weighting least squares with a bisquare weighting function). The relative percent contribution $C_i\%$ for each variable was calculated with the following equation:

$$C_i\% = \frac{B_i^* R^2}{\sum_{i=1}^{k} B_i^*} \times 100 \quad (26)$$

where B_i^* is the standardized coefficient of the *i*th variable.

SEM Measurement

Five individual fibers from each card sliver sample were examined. The two ends of each fiber were fixed on an SEM sample holder with a thin layer of glue. The mounted fibers were sputter coated with gold. Longitudinal SEM images of fibers were collected and analyzed with a custom image-processing algorithm. The algorithm, first, improved the contrast of the grayscale SEM images by evenly distributing intensity values of each image throughout the entire intensity range. Then, it segmented the fiber from the background with the Canny operator. The widest section of the segmented fibers was manually selected. The distance between the two edges of projected fiber at the widest section and perpendicular to the main axis of the fiber was reported as the actual width

of that fiber (fiber ribbon width). Mature cotton fiber is not cylindrical but has a bean or kidney shape cross-section with twists along its length. Therefore, the width of a two-dimensional projection of a fiber does not represents its width in detail, but it gives a reasonable approximation of effective width.

Nanomechanical Properties Measurements

The surface topography and nanomechanical properties images of the fibers were obtained using a multimode AFM (Bruker's Dimension Icon) in PeakForce quantitative nanomechanical property mapping (PF-QNM) mode. Measurements were performed with a Team Nanotec probe with 40 nm tip radius and the nominal spring constant of 0.06 N/m. The full cone angle of the tip was 40° and its height was 9 μm. Before each set of experiments, the laser beam was aligned on the back of the cantilever. The photodetector position was adjusted accordingly to maximize the summation signal. The deflection sensitivity of the cantilevers was calibrated by making five FDCs on a hard sapphire surface. The cantilever spring constant was determined by recording the thermal noise power spectrum of the cantilevers. The approximate regions on the fiber surface for the purpose of force measurement experiments were determined with the built-in video camera with 508-4010 x magnification range and corresponding field of view of 190—1500 μm (Figure 5). The experiments were conducted in a 5 μm × 5 μm scan size with 512 lines per scan. All measurements were carried out in air. Two locations per each fiber were imaged. The scan rate was adjusted to 0.5 Hz (tip velocity of 5μm/s). To avoid sample damage and tip wear, the Peak Force Setpoint was fixed to 10 nN. In order to reduce the contact time between the tip and sample, the Peak Force

Amplitude was set to 300 nm. The Z-piezo was set to modulate at 1 kHz. The resulting topography (Height Sensor), Peak Force error, adhesion, and deformation images were collected for statistical analysis.

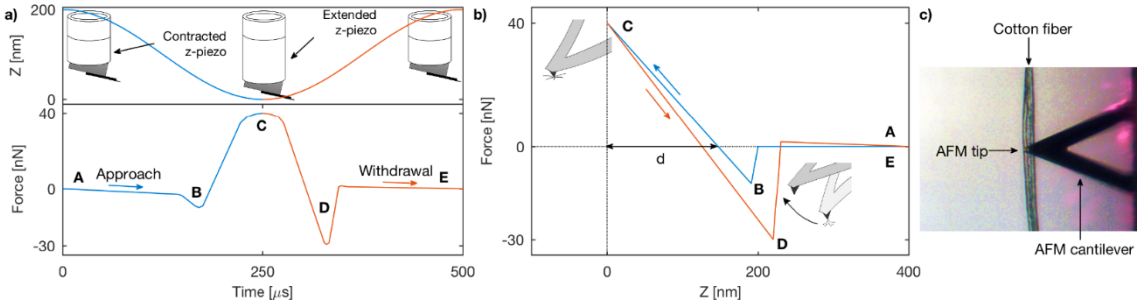

Figure 5 a) Vertical deflection of tip vs. time in a typical Peak Force Tapping mode cycle; b) vertical deflection of tip vs. piezo displacement; A – probe tip above sample surface, B – tip jumps into contact with surface, C – ultimate contact is made and tip indents the surface at a predefined PeakForce setpoint, D – tip-surface separation (adhesion force), E – z-piezo contracts and probe springs back to starting point; c) probe in contact with cotton fiber during scanning (view from built-in camera)

Estimating Real Contact Area

According to the Jonson-Kendall-Roberts (JKR) model, the tensile force required to separate surfaces from contact (pull off force) can be obtained from

$$F_{ad} = (3/2)\pi RW \quad (27)$$

where, F_{ad} is adhesive force, R is the radius of curvature of the tip, and W is the adhesion energy. For the elastic contact of two different solids, adhesion energy can be estimated from $W = \gamma_A + \gamma_B + \gamma_{AB}$ where γ denote interfacial energies between the materials A, B, and air and between materials A and B themselves. Solving equation (27) for W results:

$$W = 2F_{ad}/3\pi R. \quad (28)$$

Several studies have successfully employed the JKR model to estimate the adhesion energy of wide range of viscoelastic polymers[155–157, 187]. The adhesion energy obtained from the JKR model on polymer solids correlates well with those obtained from contact angle methods. In this study, equation (28) was used to determine the adhesion energy of the individual fibers. Afterwards, different contact theories were implemented to estimate the contact area between the AFM tip and fibers' surface. Contact mechanics is defined as the study of mechanics of solids spreading their interfacial area under normal load [134]. According to the Hertz contact theory, for a sphere of radius R_1 in contact with a flat surface ($R_2=\infty$), the true contact area is in the shape of a circle. Under elastic deformation, the contact radius a can be predicted as:

$$a = \sqrt[3]{\frac{R_1 L}{E_{tot}}} \quad (29)$$

Here, E_{tot} is the reduced Young's modulus and L is the normal force exerted by the asperity on the surface. The reduced Young's modulus can be obtained from

$$\frac{1}{E_{tot}} = \frac{3}{4}\left(\frac{1-v_s^2}{E_s} + \frac{1-v_a^2}{E_a}\right) \quad (30)$$

where, v_a, E_a, v_s, and E_s are the Poisson's ratios and Young's moduli of the asperity and the surface, respectively. In the Hertzian theory, the adhesion between the two surfaces is neglected. Jonson et al. and Derjaguin et al. modified the Hertz model by taking into account the attractive forces between surface. In the JKR model, the contact radius a can be obtained from the following equation:

$$a^3 = \frac{R_1}{E_{tot}}\left(\sqrt{\frac{3}{2}\pi R_1 W} + \sqrt{L + \frac{3}{2}\pi R_1 W}\right)^2 \quad (31)$$

The JKR model is mostly applicable for soft materials with large adhesion. The Derjaguin-Muller-Toporov (DMT) model, on the other hand, is applied in the case of stiff samples with small adhesion. The contact radius in the DMT model can be obtained from the following equation:

$$a^3 = \frac{R_1}{E_{tot}}(L + 2\pi R_1 W) \qquad (32)$$

In this study, equations (29), (31), and (32) were used to estimate the real contact area $A_{real} = \pi a^2$ of fibers as a function of normal load L.

Nanotribological Measurements

The surface topography and friction images of the fibers were obtained with a multimode AFM (Bruker's Dimension Icon) in contact mode. The probe tip used for friction experiments was similar to the one described in the nanomechanical experiments section (R = 40 nm and C = 0.06 N/m). The experiments were conducted in a 2 μm × 2 μm scan size (Figure 6). The scan speed in the fast scans direction (perpendicular to the primary cantilever axis) was adjusted to 4 μm/s (calculated from 2 × (scan length) × (scan frequency)). The frictional force (in volts) was measured by taking the average difference between the lateral deflection of the cantilever obtained from right-to-left and left-to-right scanning. In this comparative study in which all the measurements were obtained with the same probe, the conversion of the lateral deflection of the cantilever to the absolute frictional force was not necessary. Contact forces were varied by changing the vertical deflection of the cantilever during scanning. The friction measurements were carried out in air, under the normal force of 10 nN to 100 nN.

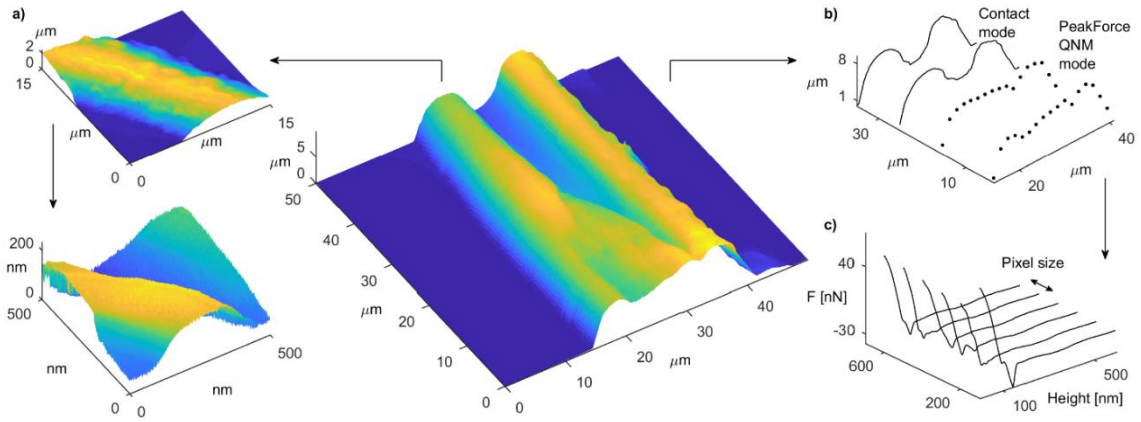

Figure 6 a) Surface topography images of cotton fibers obtained at different scan size; cotton fiber has a bean-shape cross-section b) different scan lines produced from different AFM modes; c) an array of force-distance curves as they were produced along a scan line in PeakForce Tapping mode.

CHAPTER III

RESULTS AND DISCUSSION

Macroscale Friction and Fiber Physical Properties

Results of the Five Carded Samples Study

Friction Force Variation and Coefficient of Friction

Figure 7 includes box plots of friction force measurements for the card sliver samples, grouped by the normal force. The line inside each box represents the median, and the box encloses the interquartile range. The extended lines above and below the box denote the whisker length, which corresponds to $\pm 2.7\sigma$. The small p-value of 0.00001 indicated that, for a given sample, at least one of the other friction means is significantly different from the others at the 0.1% level of significance. The pairwise comparison test results are presented in Table 3. At all normal forces, the mean friction for samples A and B was significantly higher than for the other samples. At higher normal forces (i.e., 7.3 to 15.1 N) the mean fiber friction for sample B was significantly higher than all other samples. Under most normal loads, mean friction for samples C and E was significantly lower than for all other samples, and the measured mean friction force for sample D tended to be in between. At the 10.2 and 4.9 N loads, the sample D mean was significantly different from both the lowest and the highest means.

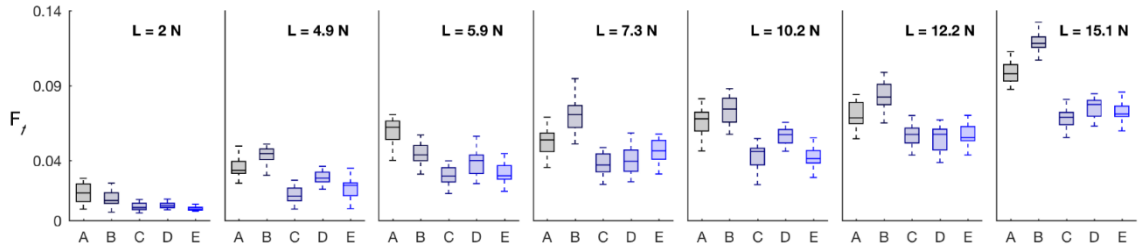

Figure 7 Distributions of fiber friction for five cotton samples under various normal loads *L*

Table 3 The mean friction force of card sliver samples

Sample	Mean friction force[1] [cN]						
	L=15.1 N	*L*=12.2 N	*L*=10.2 N	*L*=7.3 N	*L*=5.9 N	*L*=4.9 N	*L*=2 N
A	9.85 **a**	7.03 **a**	6.64 **a**	5.23 **a**	6.02 **a**	3.55 **a**	1.78 **a**
B	11.92 **b**	8.37 **b**	7.31 **b**	7.07 **b**	4.42 **b**	4.40 **b**	1.44 **b**
C	6.80 **c**	5.74 **c**	4.33 **c**	3.75 **c**	2.94 **c**	1.68 **c**	0.91 **c**
D	7.52 **c**	5.46 **c**	5.63 **d**	4.01 **c**	3.89 **b**	2.86 **d**	1.00 **c**
E	7.28 **c**	5.74 **c**	4.22 **c**	4.60 **a**	3.14 **c**	2.12 **c**	0.79 **c**

In order to obtain the coefficient of friction of samples, the mean friction and normal force data were fitted to the $F_f = \bar{\mu}L$ model with the method of least squares (Figure 8). The coefficients of determination were 0.90 or higher for all models, and regression lines were statistically significant at the 5% confidence level according to the ANOVA. This

[1] Mean values with the same letter are not significantly different at 95% confidence level (Tukey's honestly significant difference criterion)

result indicates that fibrous assemblies, similar to most bulk solid materials, obey Amonton's law of friction with a high degree of fidelity. More terms could be included in the model to achieve higher R^2 values, but additional terms would be difficult to interpret physically and fail to elucidate underlying friction phenomena. Sample B had the highest friction coefficient, and sample A also had relatively high friction. Sample C had the lowest friction coefficient among the five samples.

In order to obtain the coefficient of friction of samples, the mean friction and normal force data for each sled were fitted to the $F_f = \bar{\mu}L$ model with the method of least squares (Table 4). The coefficients of determination were 0.70 or higher for all models, and regression lines were statistically significant at the 5% confidence level according to the ANOVA (Figure 8). Although the calculated friction coefficients were higher for the 20-cm^2-sled than for the 30-cm^2-sled, the samples had the same ranking with both methods. That is, sample B had the highest friction coefficient, and sample A also had relatively high friction; sample C had the lowest friction coefficient among the five samples. This result indicates that fibrous assemblies, similar to most bulk solid materials, obey Amonton's law of friction to a significant degree. More terms could be included in the model to achieve higher R^2 values, but additional terms would be difficult to interpret physically and likely fail to elucidate underlying friction phenomena.

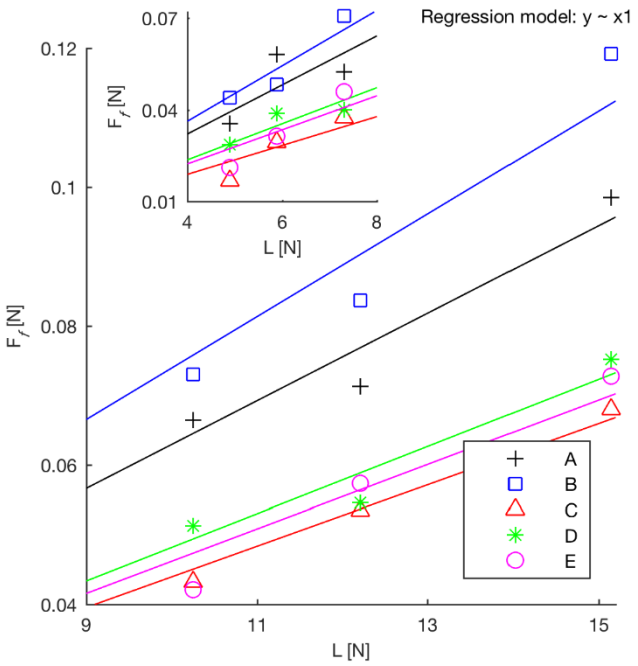

Figure 8 Plot of the mean friction force as a function of normal load

Table 4 The coefficient of friction of cotton fiber assemblies measured by sleds with different apparent contact area

Sample	μ from 20-cm^2-sled	μ from 30-cm^2-sled
A	0.0080	0.0063
B	0.0091	0.0074
C	0.0047	0.0044
D	0.0059	0.0048
E	0.0056	0.0046

Fiber Width Measurements from SEM Images

The average fiber widths for samples A, B, C, D, and E were 23.2, 26.4, 12.1, 16.7, and 19.2 micron, respectively. The SEM images of two fibers from each sample are presented in Figure 9. These measurements were in general agreement with the average AFIS fineness reading ($H = \rho A_{CW}$) for each sample (in terms of linear density: 156, 155, 166, 154, and 169 mTex, respectively). That is, fiber from samples A and B was characterized with higher ribbon width and lower linear density, as should be expected; it can be concluded that fibers from these samples had thinner cell walls and larger ribbon widths. Fiber from samples C and E was characterized with lower ribbon width and higher linear density; it can be concluded that fibers from these samples had thicker cell walls and smaller ribbon widths.

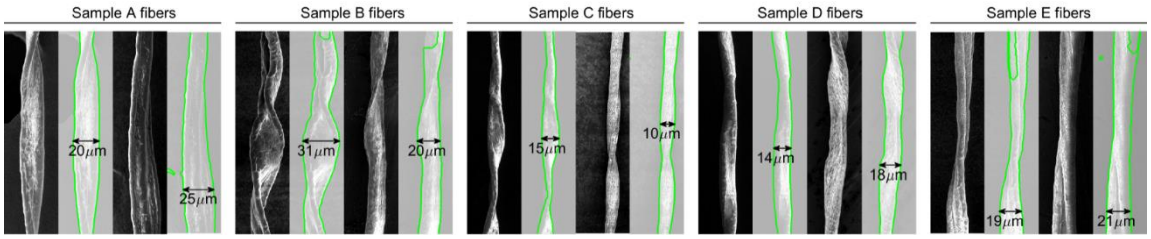

Figure 9 SEM images of fibers and their measured ribbon width

Relationships between Friction and Other Fiber Physical Properties

The distributions of the AFIS fiber dimensional properties (length, fineness, and maturity) of the card sliver samples are presented in Figure 10(a). Negative relationships existed between each of these properties and friction, with the strongest relationship between length and friction. Results further indicate that a significant (p=.05) negative relationship exists between the friction coefficient and HVI Micronaire (Figure 10(b)). A cotton sample's Micronaire value is measured as the air flow passing through a known mass of randomly oriented cotton fibers. According to the D'Arcy law,

$$Q = \frac{1}{k_0} \times \frac{A_F \, \Delta P}{{S_0}^2 \varphi B} \times \frac{\varepsilon^2}{(1-\varepsilon^2)} \qquad (33)$$

the flow Q passing through porous media is related to the area of the fibrous assembly A_F, the length of the fibrous assembly B, the pressure difference across the assembly ΔP, cross-sectional shape factor of the fibers k_o, the porosity of the assembly ε, the coefficient of viscosity of fluid φ, and fiber surface area per unit length S_0. Equation (33) thus shows that fluid flow through a fiber assembly depends in part on the orientation and dimensions of fibers. Under constant container dimensions, pressure difference, and fiber orientation, Q is inversely proportional to S_0^2. For cotton fibers, it has been shown that

$${S_0}^2 = \frac{14.7}{\theta H}. \qquad (34)$$

Here, θ and H denote fiber maturity and fineness, respectively. According to the adhesion theory of friction, friction force is related to the sum of all real contact areas formed between tips of asperities. As fibers slide on a steel plate, new nanoscale contact regions are formed while others sheared. Nonetheless, the average total real contact area

is roughly constant throughout the course of sliding. The negative correlation between the friction coefficient μ and the HVI Micronaire Q can be explained by the fact that fibers with higher Q are characterized by lower specific surface area. Therefore, the real contact area, and consequently, friction, will be comparatively lower for these high-Micronaire fibers. The negative correlation between fiber friction and AFIS dimensional properties (Figure 10(a)) is more noticeable when the product of H and θ is considered (Figure 10(c)). According to equation (34), $\sqrt{\theta H}$ is inversely related to the specific surface area S_0.

Friction is a complex surface phenomenon. Its magnitude depends not only on the real contact area but also on the shear strength of the contacting surfaces. The existence of lubricant between contacting surfaces significantly reduces friction, mainly due to the lower shear strength of the lubricating film. As cotton fibers slide on the metallic plate, slip takes place at slip planes between fatty acid molecules (Figure 11). The fatty acids' hydrocarbon chain length, the film viscosity, and the layer thickness affect the shear strength of the waxy layer, which is also affected by external factors such as the temperature at the contact interface, the applied load, the sliding velocity, and the humidity of the surrounding environment[136]. Figure 10(d) shows a significant ($p = 0.05$) negative correlation between +b and μ. The $+b$ value is comparable to the b^* dimension in the CIE color space and indicates the degree of fiber yellowness. Very few studies have been published on the origin of fiber color variation among cotton varieties. In practice, prolonged fiber storage at high humidity and temperature can lead to significant color changes in cotton samples. Because of growth and germination of microorganisms

(fungi or bacteria) on the fiber surface over time and through poor storage conditions, the intrinsic color of the fiber shifts toward darker yellow shades. In this study, samples did not experience prolonged storage. Therefore, the variation in $+b$ is mainly due to the intrinsic color of the fibers. It is conceivable that, within a variety of cotton, for fibers that are not affected by weathering, heat treatment, or storage conditions, changes in $+b$ can be attributed to the amount of the waxy layer on fiber surface. In fact, it has been reported that the wax extract from cotton is pale yellow in color. The yellowness of the waxy layer has been attributed to the presence of oxycellulose and proteins in the waxy layer [188]. In textile post-processing, the waxy layer, which affects the light absorption, can be removed to achieve a high degree of whiteness. The negative correlation between the $+b$ and μ has been also observed in previous studies [82, 178]. Brushwood has conducted several studies on relationships among cotton fiber friction, wax, $+b$, and other fiber physical properties [178]. He reported a strong negative correlation between $+b$ and fiber friction (as measured by RotorRing) (inset plot in Figure 10(d)). He also reported a strong positive correlation between $+b$ and the metals on a fiber surface. Metals serve to crosslink pectin biopolymers. Pectins are only present on the fiber surface (cuticle layer). Therefore, an increase in the concentration of metal oxides corresponds to an increase in the amount of pectins or cuticular materials, such as wax [178]. El Mogahzy et al. have also reported a significant negative correlation between the fiber friction and $+b$ [82]. More study is needed to better illuminate the relationships between the fiber natural color, its lubricity, and wax content.

Figure 10(e) shows the strong positive relationship (R^2 = .92) between μ and short fiber content (SFC). It is likely that, during the harsh mechanical separation process of the AFIS fiber individualizer, fibers with higher inter-fiber friction and crimp have a lesser tendency to detach from their bulk. Therefore, some fibers may break into shorter fibers as the individualizer seizes them [189]. This action of the AFIS instrument is similar to actions fibers experience in fiber blending and opening processes during lint cleaning in the cotton gin. The results herein tend to confirm the fiber-breakage concept by suggesting that fibers with higher friction coefficients have greater propensity to break during fiber processing. It is expected that fibers with higher natural lubricity, and thus lower friction, separate more readily from their bulk. As a result, they will flow more individually, orderly, and smoothly throughout different stages of fiber processing. As a result, the internal structure of the manufactured yarn from these smoother fibers is more uniform and cohesive [79, 82, 86].

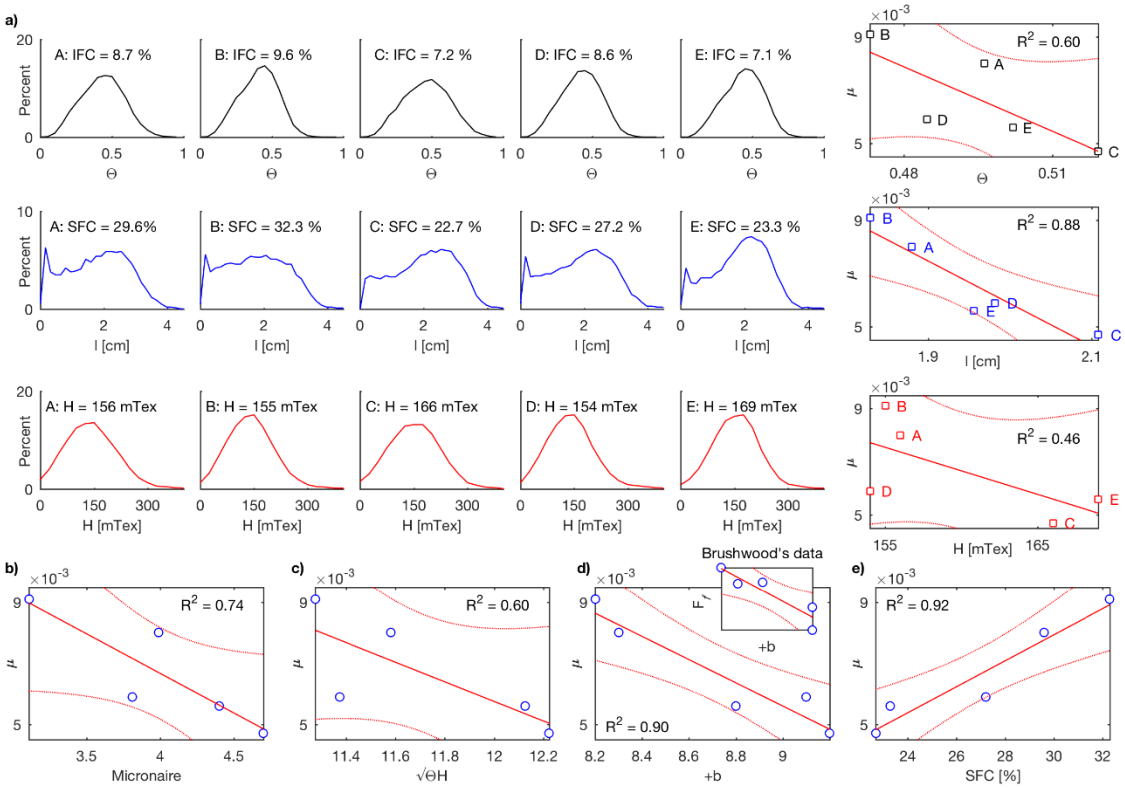

Figure 10 (a) Distributions of the AFIS fiber dimensional properties and their relationship with μ; corresponding values for the immature fiber content (IFC), the SFC, and the average fineness are presented. (b) Relationship between the friction coefficient and the Micronaire; (c) relationship between the friction coefficient and the square root of $H\theta$; (d) relationship between the friction coefficient and the $+b$; (e) relationship between the friction coefficient and the SFC**;**

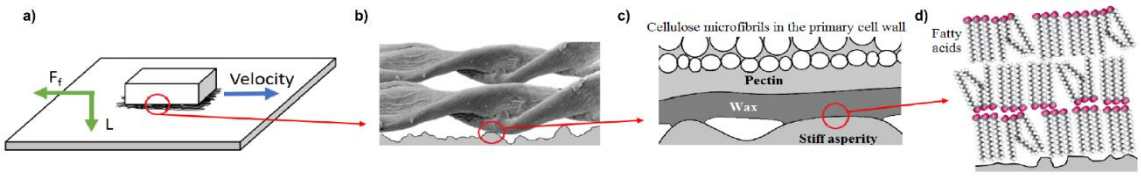

Figure 11 (a) Schematic of the fiber assembly sliding friction; (b-c) contact between cotton fibers and a nominally flat surface with nanoscale surface roughness at different length scale

Contact Area Simulation as a Function of Fiber properties

Figure 12(a) shows the relationships between the assembly contact area and the *r*, *l*, and θ values as obtained from the fiber simulation model. The calculated number of fibers in an assembly as a function of *r*, *l*, and θ is presented in Figure 12(b). Under constant θ and *r*, fiber assemblies with shorter fibers (1.8 to 2.2 cm) have more fibers in their structure, but fiber length did not considerably affect the calculated real contact area. Under constant length, assemblies with more immature fibers ($0.3 < \theta < 0.4$) and smaller radius fibers ($2.5 < r < 5.0$ μm) are associated with higher contact area (Figure 12(a)) and a higher number of fibers in their structure (Figure 12(b)). More fibers near the surface of the assembly increases the probability of mechanical interlocking between the fibers and fine texture of the metallic substrate. These relationships between fiber geometry parameters and contact area are in agreement with the experimental results and can be summarized by the following proportions:

$$F_f \propto S_0 \propto \frac{1}{\sqrt{\theta H}} \propto \frac{1}{\sqrt{Q}}. \quad (35)$$

In equation (35), the relationship between F_f and S_0 was theoretically interpreted from equation (7). It is logical to say that bulk fiber with higher specific surface area also provides more contact area with a given flat surface. The inverse relationship between S_0 and $\sqrt{\theta H}$ is clear from equation (34). The same relationship has been observed in the empirical results herein (Figure 10(c)). The modeling approach also revealed that $\sqrt{\theta H}$ has an inverse relationship with the true contact area of the fiber assembly (Figure 12(a) shows that, under constant length, fiber assemblies with smaller *r* and θ provide higher

contact area with a given flat surface). The inverse correlation between $\sqrt{Q}$ and S has been obtained from equation (33).

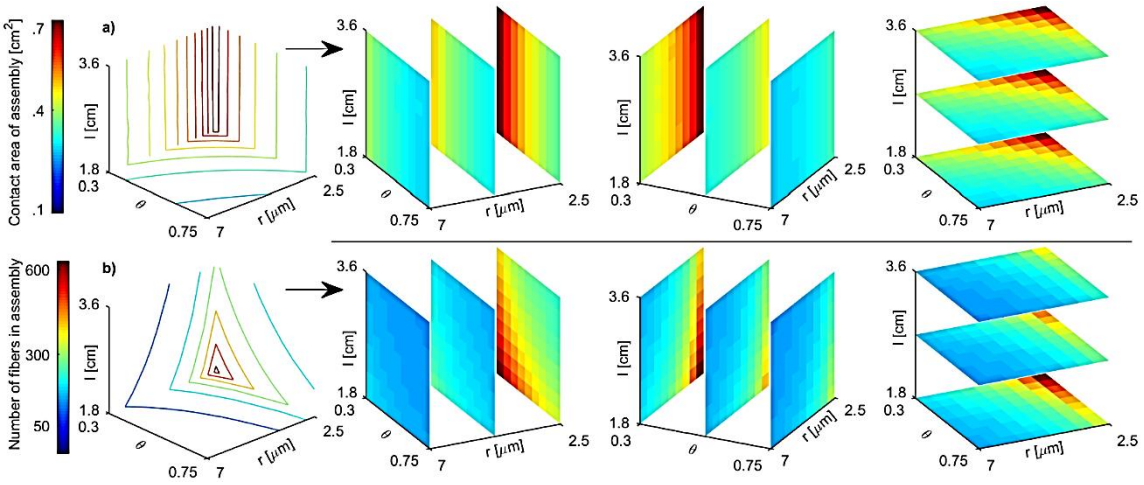

Figure 12 (a) The contact area of a known mass of fibrous assembly as a function of fiber length, maturity, and radius computed from the fiber simulation model; all four plots present the same volume data set. In order to provide a better visual context, the three plots on the right show different slice planes. Each slice plane expresses the variation in the real contact area when one of the three independent variables—l, θ, or r—is constant. (b) The number of fibers in a known mass of fibrous assembly as a function l, θ, and r; similar to (a), the slice planes in the three plots on the right depict the variation in the number of fibers when one of the three independent variables is constant.

Results of the Forty-Eight Ginned Samples Study

Friction Force Variation and Coefficient of Friction

Figures 13-14 depict the variation in fiber friction across the 48 ginned fibers from various cotton varieties. The distribution of fiber friction within each variety is displayed with a box plot (Figure 13). The black line inside each box represents the median, and the extended lines indicate the whisker length ($\pm 2.7\sigma$). The small p-values computed in

the ANOVA ($p<.0001$) suggested that at least one sample's friction mean, under a given normal force, is significantly different from the others, with a very high level of confidence. As previously mentioned, these varieties were grown, harvested, and ginned at the same date and location. Therefore, their variation in fiber cell maturity was minimized. Figure 14 shows the variation in friction force under 12.2 N normal force, as they are sorted by mean friction. Varieties were classified into three groups using arbitrary class boundaries. A large majority of the 48 varieties were classified into groups that produced fiber with either low or medium-range friction. Only seven had significantly higher friction than the rest. Figure 14 also shows a hierarchical binary cluster tree of the grouped data. The cluster tree shows that the difference between mean friction forces of any group compared to its nearest neighbor is on the order of 0.06 N, meaning these groups had differences in friction of between 5 and 10%. The small p-value ($p<0.0001$) for all case comparisons suggests that mean fiber friction was significantly different from group to group among all groups (Figure 14, inset plot).

Figure 15 shows the variability of fiber friction coefficients across the 48 cotton varieties. The regression lines were all significant (*i.e.,* slopes were nonzero) and had a high coefficient of determination. The models exhibit a wide range of slopes from 0.0669 to 0.0783. The friction coefficient of these bulk cotton fiber samples follows a normal distribution with a mean of 0.0719 and standard deviation of 0.0025. The mean friction coefficient for random assembly of the unprocessed cotton fiber is in the order of ten times greater than that of the processed and carded fiber.

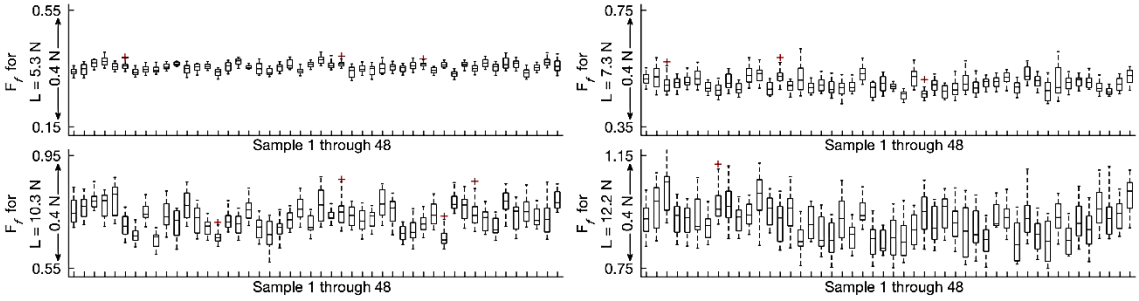

Figure 13 Distributions of fiber friction for forty-eight cotton varieties under various normal loads

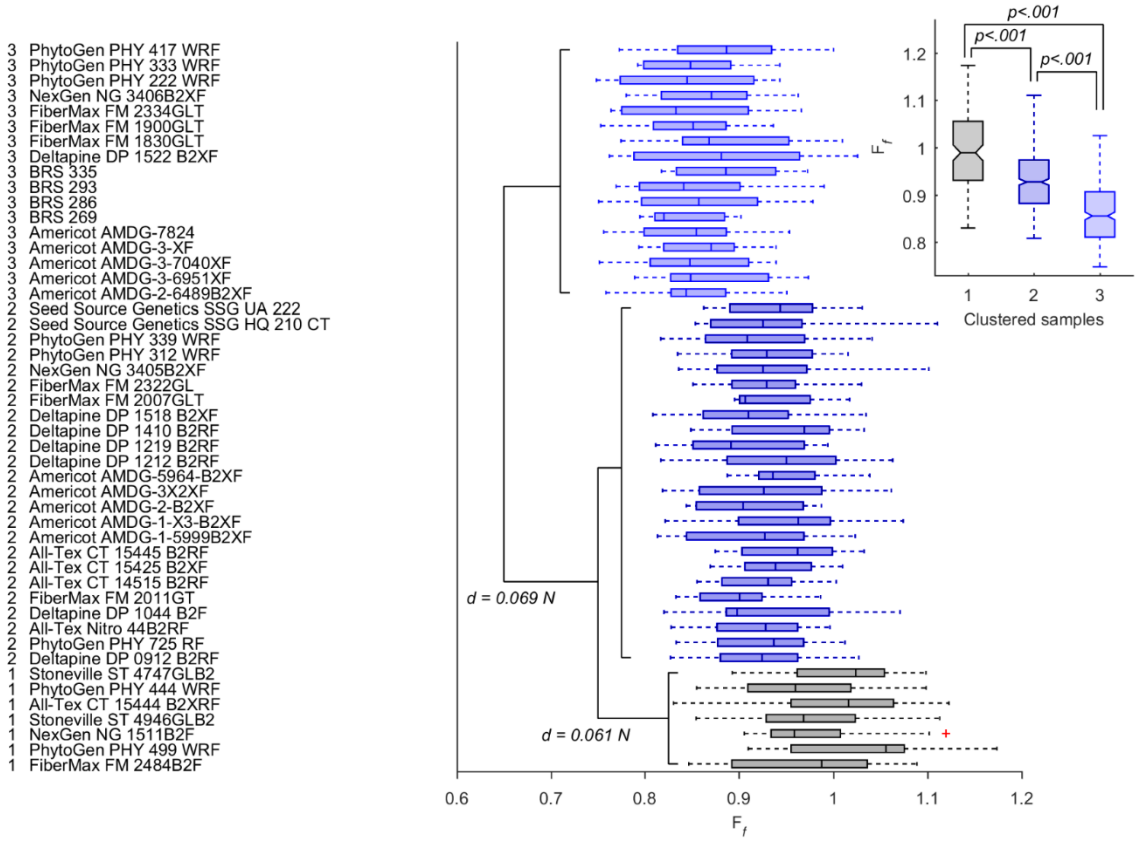

Figure 14 Distribution of fiber friction–under 12.2 N normal load–for different cotton samples, sorted by mean friction force; cotton varieties are classified into three groups using arbitrary class boundaries; (inset plot) fiber friction distributions for grouped fibers and their pairwise comparison at $\alpha = .05$

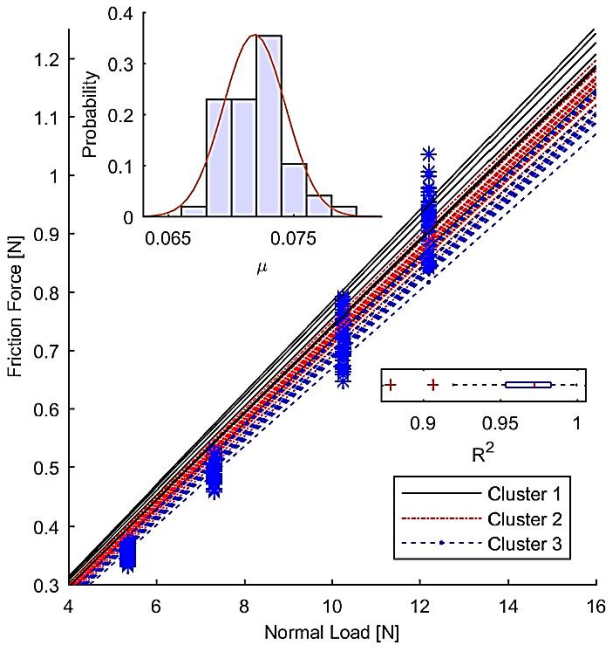

Figure 15 Plot of the mean friction force as a function of normal load; (inset plot) the histogram of μ

Relationships between Friction and Other Fiber Physical Properties

The results of multiple regression analysis on data from the 48 raw fiber samples are presented in Table 5 along with standardized coefficients and relative percent contributions. The coefficient of determination for the full F_f and μ models was 0.50 and 0.71, respectively. No actual model can perfectly estimate the tribological properties of natural fibers. In addition to inherent measurement error, there are always some unmeasured, hidden factors, which affect the frictional properties of cotton fiber. The

results from this analysis should thus not be considered as a predictive tool but rather as an indication of trends between significant fiber parameters and friction. The relationships between fiber properties and fiber friction obtained from the 48 raw fiber samples were in agreement with results from the five card sliver samples. The HVI properties that are apparently significantly related to friction are $+b$, Q, and fiber bundle elongation. The inverse relationships that $+b$ and Q have with fiber friction were discussed previously. In this larger 48-sample data set, a significant positive correlation between fiber elongation at break and fiber friction characteristics was observed. While it is not completely clear why this is the case, the effect of elongation seems to be due the experimental procedure. One possible explanation is, as a fibrous assembly slides on a hard surface, some fibers near the surface of the assembly will be embedded in a fine groove of the rigid plate, under high normal force. Tangential forces will be exerted on the imbedded fibers to separate them from the groove. These forces stretch and deform the fibers. Fibers with higher elongation undergo larger deformation until they separate from the groove and slip off. As mentioned previously, fibers from the 48 raw fiber samples were partitioned into three groups based on arbitrary class boundaries. Figure 16(a) shows the variation in mean friction force F_f, μ, Q, $+b$, and elongation associated with these groups. The mean HVI fiber properties varied between groups in accordance with the general trends observed earlier. That is, with increasing fiber linear density (as indicated by the airflow rate Q) and thickness of the natural waxy layer on the fiber surface (as possibly indicated by the degree of yellowness $+b$), fiber friction decreased. Conversely, higher friction was positively associated with higher elongation. Although

the fiber groups created in this study differ significantly in their frictional characteristics at .01 level of significance, their HVI properties do not necessarily show marked dissimilarities. In some pairwise comparisons between groups, these properties were not significantly different. Figure 16(b) shows the coefficient of friction data as a function of elongation and $+b$. A multiple-linear regression plane $Y = \beta_0 + \beta_1 x_1 + \beta_2 x_2$ was fitted through the data. Elongation and $+b$ account for ~65% of the variability that existed in fiber friction among these 48 samples. These observations on the larger dataset clearly indicate that frictional properties of cotton fibers do not originate from a single mechanism. In fact, multiple frictional mechanisms (adhesion, deformation, and lubrication) appear to be involved in this complex surface phenomenon. The relative importance of each mechanism depends on conditions of contact and type of fiber.

Table 5 Standardized coefficients β_i^* of the variables and their relative contribution $C_i\%$ to fiber friction

High Volume Instrument readings	Independent variable μ^*				Independent variable F_f^*			
	β_i^*	Standard error	$C_i\%$	*P*-value	β_i^*	Standard error	$C_i\%$	*P*-value
Micronaire	-0.30	0.13	18	**.03**	-0.20	0.17	13	.26
Length	-0.01	0.12	1	.80	+0.07	0.16	5	.65
Strength	-0.02	0.11	1	.75	+0.02	0.14	2	.87
Elongation	+0.26	0.11	16	**.02**	+0.29	0.14	20	**.04**
Rd	-0.07	0.09	4	.42	-0.08	0.12	5	.53
+b	-0.49	0.11	30	<**.001**	-0.37	0.15	25	**.009**
Intercept	0	0.08	0	1	0	0.11	0	1

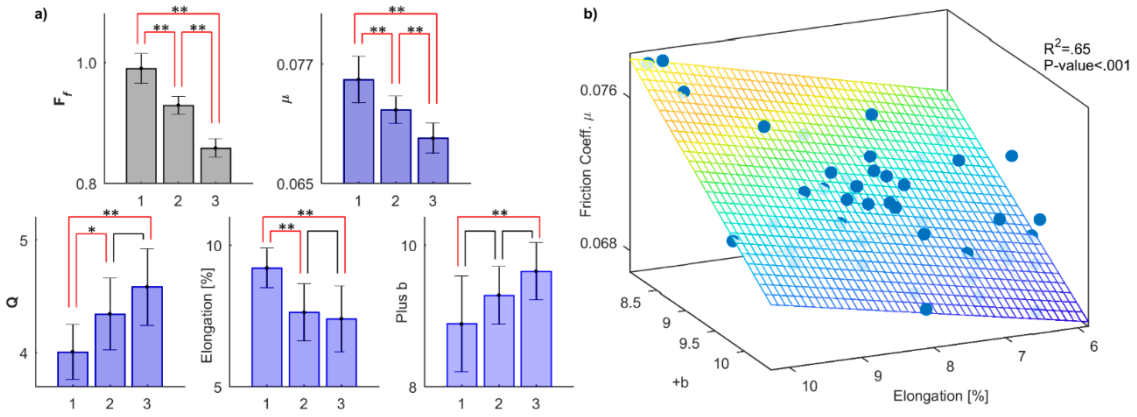

Figure 16 (a) Variation in the mean friction force, the friction coefficient, Micronaire, elongation, and $+b$ associated with grouped fibers; the error bars indicate the standard deviation of samples. In pairwise comparisons, ** and * indicate a significant difference at α=.01 and α=.05, respectively. (b) Friction data and fitted plane as a function of elongation and $+b$

For future investigation, the influence of fiber surface lubricity and waxy layer thickness on mechanical properties of fibers need to be investigated in more detail. The variation of these properties among different varieties of cotton could be investigated with force spectroscopy techniques such as Scanning Force Microscopy.

Nanofriction and Surface Nanomechanical Properties

Nanotopography Image of the Fibers

Figure 17 shows 5 µm × 5 µm three-dimensional surface topography and flat images of fibers from samples A and B (four fibers per each sample are shown). These height images were obtained in PeakForce QNM® mode (the corresponding adhesion and deformation images for each scanned area are presented in Figures 24 and 25, respectively). The scanned areas could be obtained from different regions of a fiber's

surface. Since cotton fiber has a bean-shaped cross-section, the scanned areas can be concave, convex, or relatively flat. As can be noticed in topography images, a characteristic sequence of furrows and ridges is evident on all fibers. The furrows and ridges are attributed to the wrinkles in the fibers primary cell wall, which are characteristics of dried, untreated cotton fiber. A growing fiber cell inside the cotton fruit is a hollow tube with high water content. As the fruit dehisces, the fiber is exposed to air and desiccates. The wrinkles are believed to be formed during the shrinkage of the fiber secondary cell wall in its initial desiccation. Figure 18 shows 2 μm × 2 μm three-dimensional surface topography images of the fibers from samples A and B, as obtained in contact mode (the corresponding friction images for each scanned area, under different normal loads, are shown in Figures 19 and 20). In addition to the furrows and ridges on the fibers surface, a series of irregular-shaped, particulate/plaque-like surface deposits are evident at this length scale. These granular surface deposits seemed to be more abundant on sample B fibers. While their exact nature is unclear, they could be associated with the self-assembly and growth of wax crystals. Plant cells' waxy components mostly travel through different layers of the cuticular membrane and build up on the outermost layer of the cuticle. After deposition on the plant organ surface, they self-assemble into a thin continuous lipid-film. They can form various crystalline microstructures, such as tubules (0.3 − 3 μm long and 0.1 − 0.3 μm wide), platelets, and rodlets, so it is possible the plaque-like deposits are some form of crystalline wax.

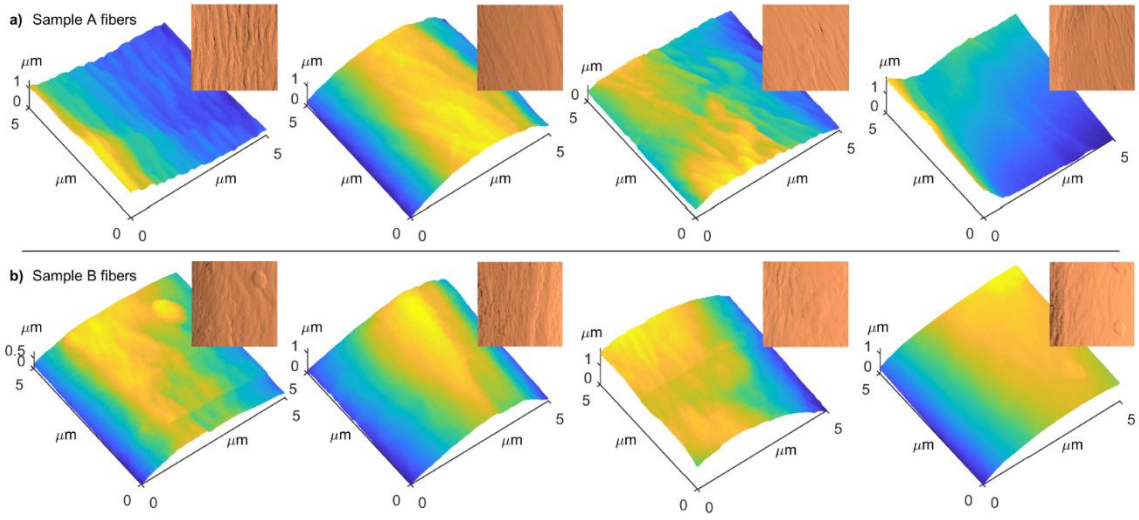

Figure 17 The 5 μm × 5 μm three-dimensional surface topography and flat image of fibers as obtained in Force Tapping mode (the corresponding adhesion and deformation images for each scanned area are presented in Fig. 10 and 11, respectively). The furrows and ridges on fibers surface are attributed to the wrinkles in the fibers primary cell wall, which are characteristics of dried, untreated cotton fiber.

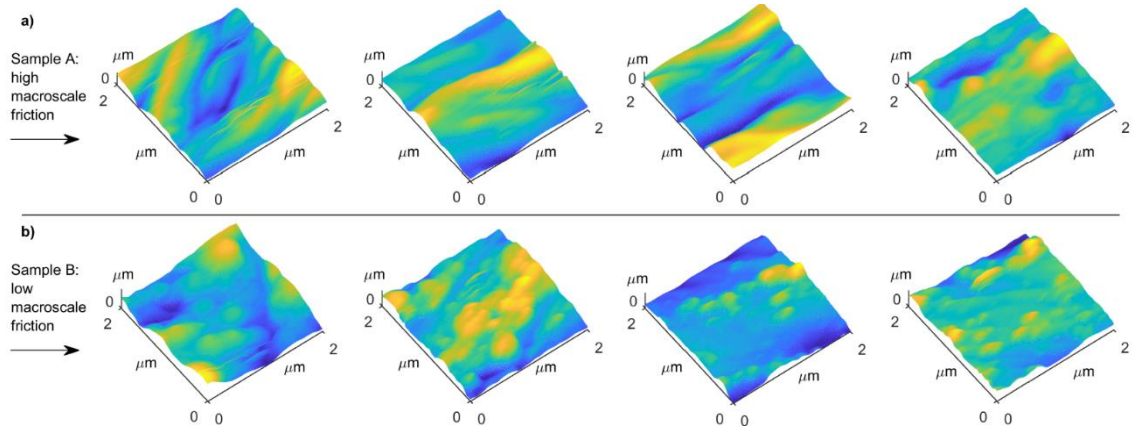

Figure 18 The 2 μm × 2 μm three-dimensional surface topography of fibers as obtained in contact mode (the corresponding friction image under increasing normal force for each scanned area are presented in Fig. 5 and 6). The granular surface deposits can be due to the self-assembly and growth of wax crystals.

Nanofrictional Properties of the Fibers

The friction images of the fibers obtained under the 10 nN normal load are shown in Figure 19. Under this normal load, the differences in friction between the two samples were not quite significant. Fibers from sample B were characterized with slightly higher nanoscale friction, but no general trend was observed to distinguish samples from one another. Figure 20 shows the friction images of the fibers obtained under the normal load of 50 nN. Under this higher normal load, the nanofriction signal was significantly different between the two samples. Fibers from sample A with higher macroscale friction were also characterized with significantly higher nanoscale friction. That is, the AFM probe experienced a higher degree of lateral deflection as it was raster scanning the surface of the fibers from sample A. Local variations in the nanofriction signal, which are more evident with sample B fibers, appear to be due to topographical effects. These variations can be explained by the ratchet mechanism. As the tip encounters an asperity with a given slope during raster scanning, it climbs against it and sends a larger lateral deflection signal to the position-sensitive detector. However, this lateral deflection signal is in part due to the variation in slope of the surface. These local variations are often referred to as the ratchet mechanism component of friction. Even though the trace and retrace friction signals have been subtracted, the local variations are still evident on the resulting images. Figure 21 shows the normalized histograms and their corresponding Gaussian fit for all the friction experiments under 50 nN normal load. The friction force distributions of the two samples were very well-separated. The

mean friction signal was 1.5 V for sample A fibers, compared to the significantly lower value of .75 V for sample B fibers.

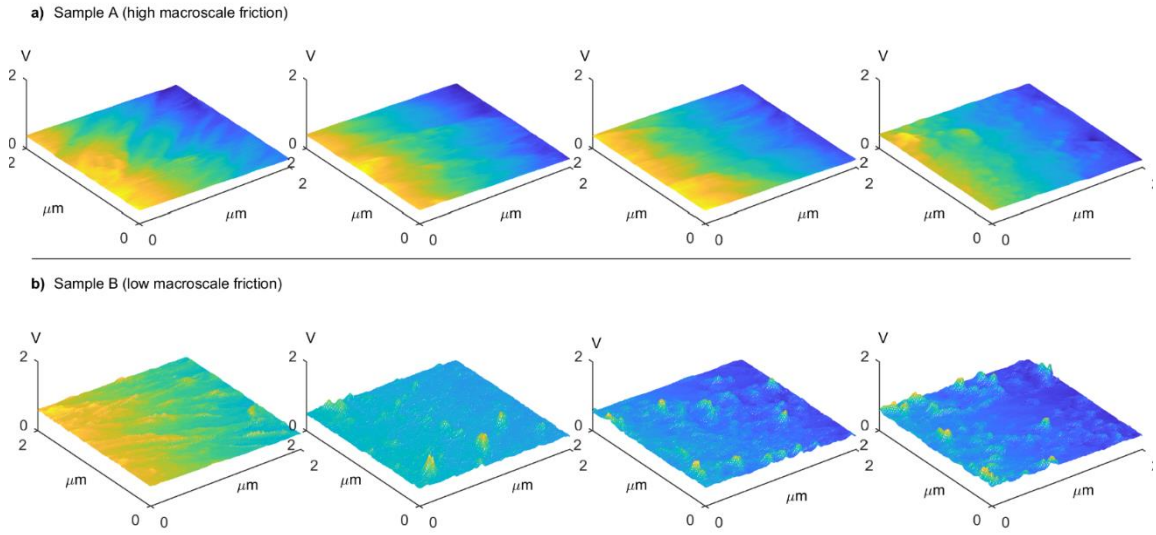

Figure 19 Friction images of the fibers obtained under the 10 nN normal load. Under this normal load, differences in friction signal between two samples were not quite significant.

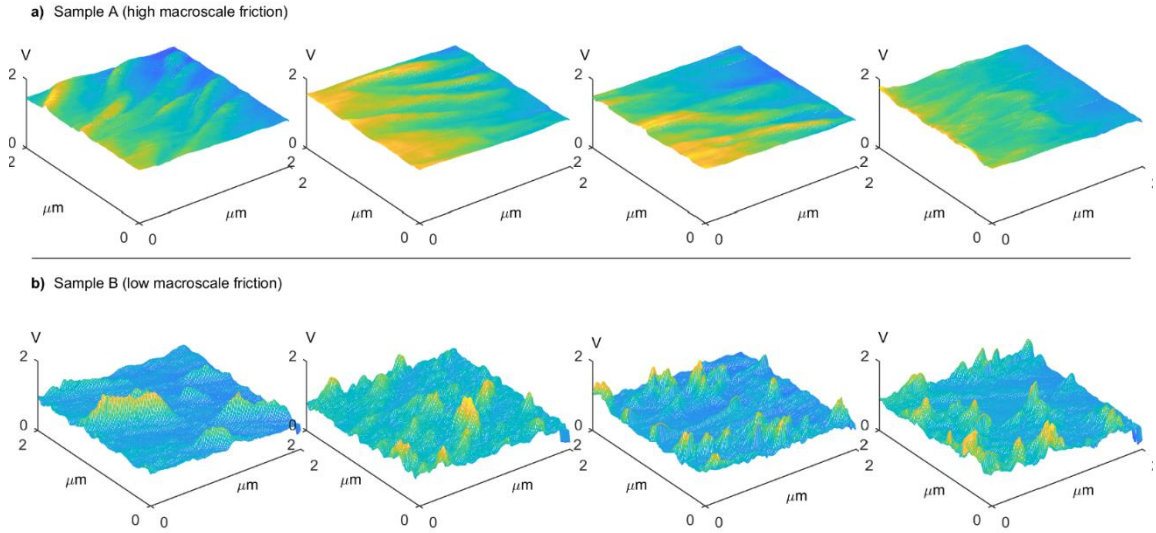

Figure 20 Friction images of fibers obtained under the normal load of 50 nN. Fibers from sample A with higher macroscale friction were also characterized with significantly higher nanoscale friction.

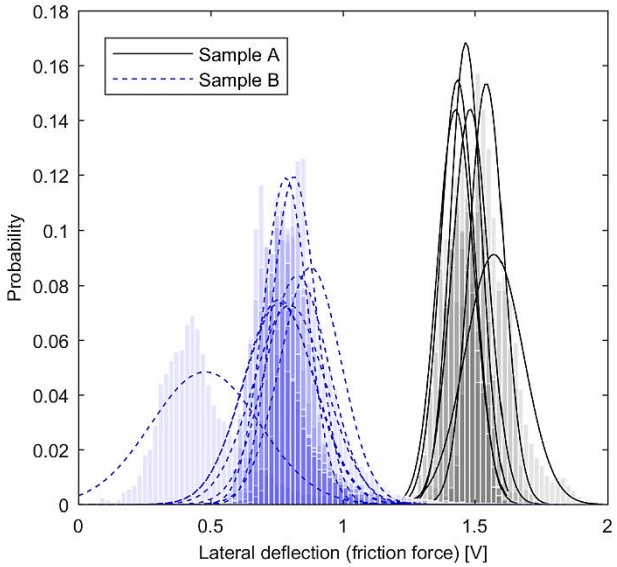

Figure 21 Normalized histograms and their corresponding Gaussian fit for all the friction experiments under 50 nN normal load. The friction force distributions of two samples were very well-separated. The mean friction signal was 1.5 V for sample A fibers, compared to the significantly lower value of .5 V for sample B fibers.

The relationship between microscale friction and normal load for all tested fibers is shown in Figure 22. As previously mentioned, at lower normal forces, no general trend was observed to distinguish samples from one another. It is possible that the relatively blunt tip with low spring constant could not penetrate into the fibers cuticle layer and slid on their outer surface for both samples, which are covered with lipid and fatty acid compounds. Therefore, these long chain hydrocarbons may have acted as a lubricant layer and reduced the shear forces between the tip and the fiber surface. Possibly for this reason, no significant differences between the nanoscale friction of fibers could be observed at very low normal forces. With increasing normal force, it is possible that the tip motion during raster scanning laterally displaced the cuticle layer molecules and piled them up on the two sides of the scanned area. As a result of this wear mechanism, the more hydrophobic compounds on the outer most layer of the cuticle layer may have been removed and the more hydrophilic layer underneath it, *i.e.* cellulose microfibrils in the primary cell wall, may have been exposed to the silicon nitride tip. As the scanned area became more hydrophilic, it is reasonable that water meniscus formation between the tip and surface increased; if this phenomenon occurred, the intermolecular interactions between the tip and the surface would have increased and the friction signal would have become stronger.

The same general trend, i.e. increase in friction at higher normal forces, was observed for fibers from both samples. However, the increase in friction as a function of normal force was much larger for fibers from sample A compared to sample B fibers, especially

at higher normal forces. In fact, sample A nanofriction seems to hold a linear relationship with the applied normal force. Nevertheless, the fundamental theoretical and empirical studies on single asperity friction show that the relationship between friction and normal force is sublinear. The deviation of sample A nanofriction from a sublinear relationship with normal force suggests that, after initial friction experiments at low normal forces, the scan area has been damaged (Figure 23(a)). That is, the tip motion has displaced the outer most layer on the fiber surface and, as a result, the surface underneath it, with new properties, has been exposed to later friction experiments. It is possible that the newly exposed surface in sample A is more hydrophilic since the friction increases at high normal loads. As already noted, for hydrophilic materials, nanoscale friction will be higher due to greater adhesion between the tip and the surface, because of the formation of a water meniscus between the tip and the surface. On the other hand, it seems that the fiber B surface did not experience the same type of damage and the tip slid on the same cuticular material even after significant wear. These observations can be explained by variation in the cuticle layer thickness among different fiber varieties. It is conceivable that the fibers from sample A are naturally coated with a thinner cuticle layer. As the friction experiments were conducted on the same scan area, the hydrophobic lubricant materials may have been removed from the fiber surface in the middle of the experiments. Therefore, the more hydrophilic layer underneath was exposed to the tip during the last friction tests at higher normal forces (Figure 23(b)). Also, it is possible that fiber B samples were covered with a thicker cuticle layer. As the friction tests were conducted on the same scan area, the tip was not able to fully

penetrate through the entire thickness of the cuticle layer. Therefore, the scanned surface may have remained less hydrophilic compared to sample A. This reasoning suggests that the outermost hydrophobic layer of the fiber surface may not have been completely displaced during friction tests, partially due to its higher thickness (Figure 23(c)).

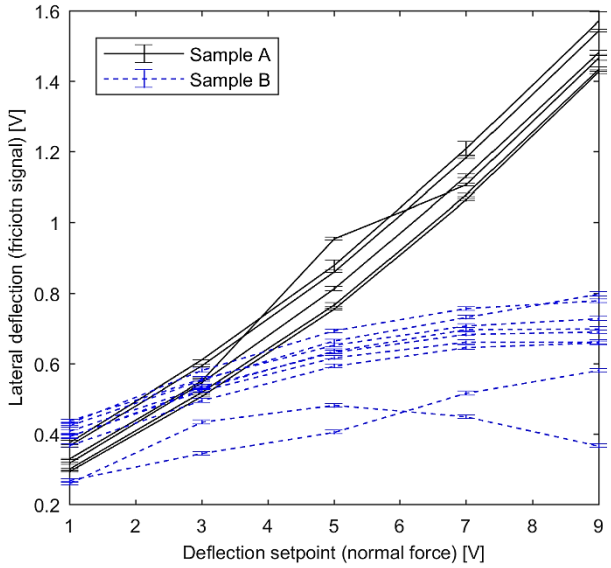

Figure 22 Relationship between single asperity nanofriction and normal load for all tested fibers

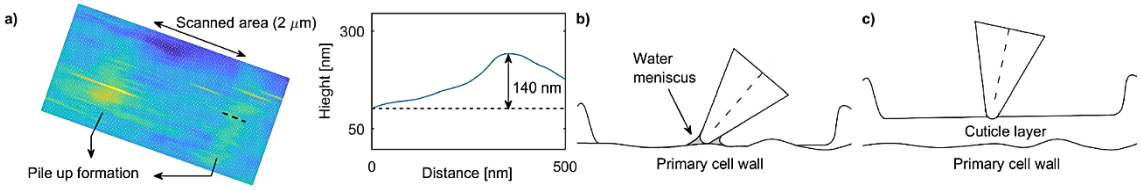

Figure 23 a) Typical wear mark after a set of friction experiments; the plot shows height profile along the dashed line; b) schematic of tip-surface interaction for fibers with thin cuticular membrane; c) schematic of tip-surface interaction for fibers with relatively thick cuticular layer

Nano-scale Fiber Adhesion, Deformation, and Contact Area Analysis

Figure 24 shows the adhesion images of the fibers. The mean pull-off force for sample A fibers was 37.7 ± 5.8 nN compared to 20.8 ± 6.5 nN for sample B fibers. The p-value of close to zero ($p < 0.001$) indicates that differences between the adhesion means are significant. Since water meniscus may play a major role in single asperity adhesive forces, the higher adhesion for sample A fibers was possibly in part due to their higher surface hydrophilicity. Due to their higher surface energy, they should attract more water molecules. Therefore, a larger water meniscus should form as the tip approaches their surface. Fibers from sample B were characterized with lower adhesion due to their more hydrophobic surface. Generally, surface hydrophilicity of cotton fiber can be affected by chemistry and orientation of lipid and fatty acid molecules (such as their hydrocarbon chain length), the viscosity of the thin waxy layer on the fiber surface, and the thickness of the cuticular membrane. However, since the nanofriction tests under various loading showed that sample B fibers are likely covered with a thicker cuticle layer, it seems possible that the thicker cuticle layer of these fibers also reduced their water affinity and lowered their adhesion.

Figure 25 shows the maximum surface deformation images of the fibers obtained in PeakForce QNM® mode. The mean maximum penetration depth of the tip was considerably higher for sample A fibers. The mean maximum deformation for the sample A fibers was 13.6 ± 5.1 nm, compared to 1.8 ± 1.3 nm for the sample B fibers.

The p-value of close to zero ($p<0.0001$) indicated that the mean maximum deformations for samples A and B were significantly different. According to the JKR theory, under the elastic regime, the indentation depth *d* is related to radius of curvature of the tip *R*, contact area *a*, modulus of elasticity of the surface *E*, and adhesion energy *W*:

$$d = \frac{a^2}{R} - \frac{2}{3}\sqrt{\frac{6\pi W a}{E_{tot}}} \quad (36)$$

Among these variables, *R* can be considered constant throughout all the experiments. However, *a*, *W*, and *E* could vary in each experiment. The contact radius *a* itself depends on *R*, *E*, applied normal force *L*, and *W*. Since the applied normal force was kept constant, the variation in deformation *d* could only be explained in terms of *W* and *E*. In this regard, the higher surface deformation in sample A fibers can be attributed to their higher nanoscale adhesion or lower local stiffness – which is related to the biophysical properties of the cuticle. On the other hand, the lower surface deformation in sample B fibers could be in part due to their stiffer surface or lower adhesion. Overall, the nanoscale deformation data were in agreement with nanofriction results. The surfaces with higher deformation provide more contact area between the tip and the surface. As a result, interaction between the tip and the surface increases, leading to higher frictional forces.

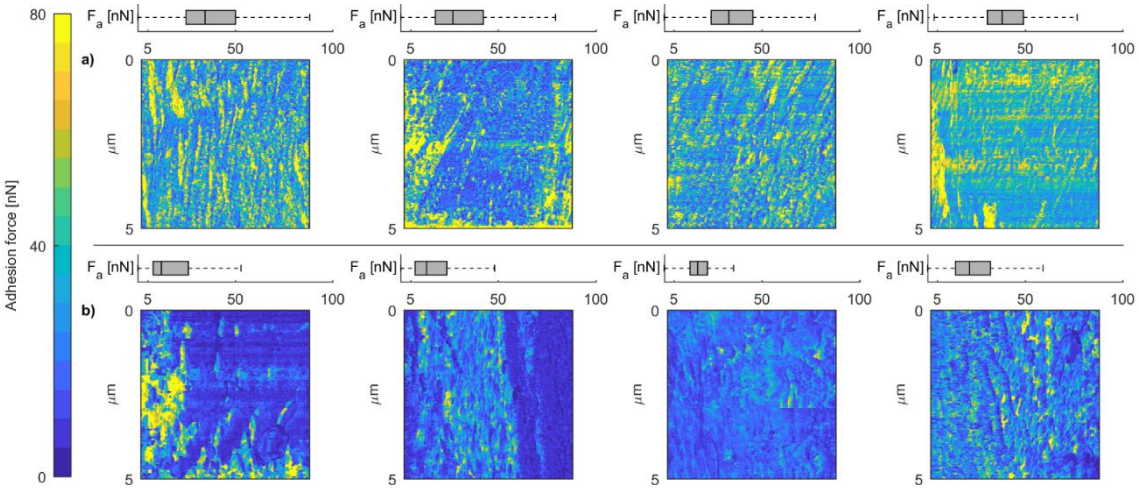

Figure 24 Adhesion images of the fibers as obtained in PeakForce Tapping mode. The corresponding adhesive force distribution is presented in the form of box plot above each image. The mean pull-off force for the sample A fibers was 17.2 ± 6.2 nN, compared to 45.5 ± 10 nN for the sample B fibers

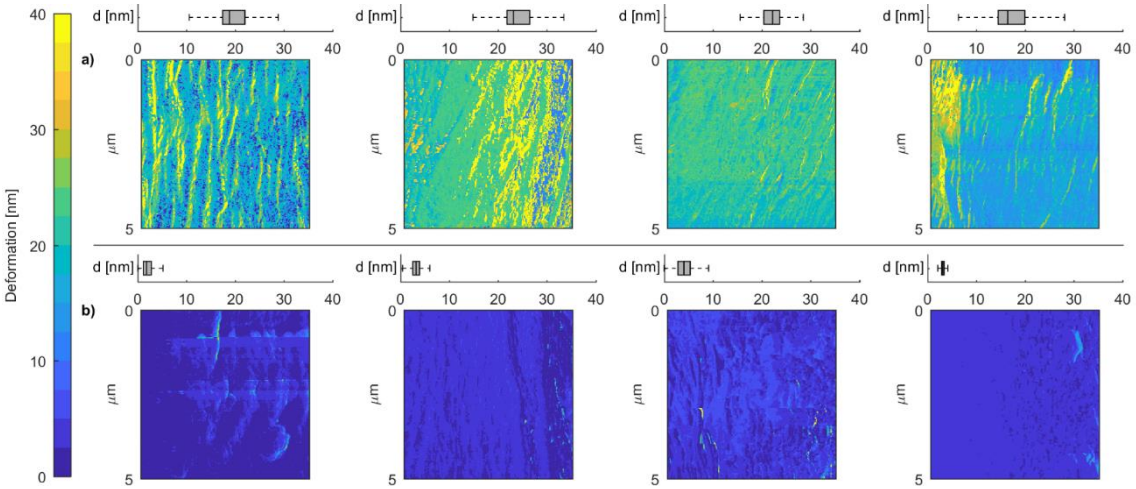

Figure 25 Deformation images of the fibers generated in PeakForce Tapping mode. The corresponding nanoindentation depth distribution is presented in the form of box plot above each image. The mean surface deformation for the sample A fibers was 6.3 ± 1.2 nm, compared to 22.5 ± 3 nm for the sample B fibers

The contact area between the tip and the fiber surface has been estimated with contact mechanics theories (Hertz, JKR, and DMT). The input average adhesion energy for sample A and B fibers were 0.2 and 0.11 *N/m*. Figure 26 shows the stated contact area for sample A and B fibers as a function of normal force. Under each contact mechanics model, the calculated real contact area is larger for sample A fibers. This estimation is in agreement with friction and adhesion experiments. That is, in larger real contact areas, interactions between the tip and the surface increase and the overall resistive forces become larger. Among different contact theories, the JKR estimated larger real contact area, because the JKR takes into account the short-range adhering force between the contacting surfaces once the contact is made. DMT only considers the long-range attractive forces before the contact is made. As can be seen, the Hertzian model underestimated the real contact area since it ignores attractive forces between the surfaces.

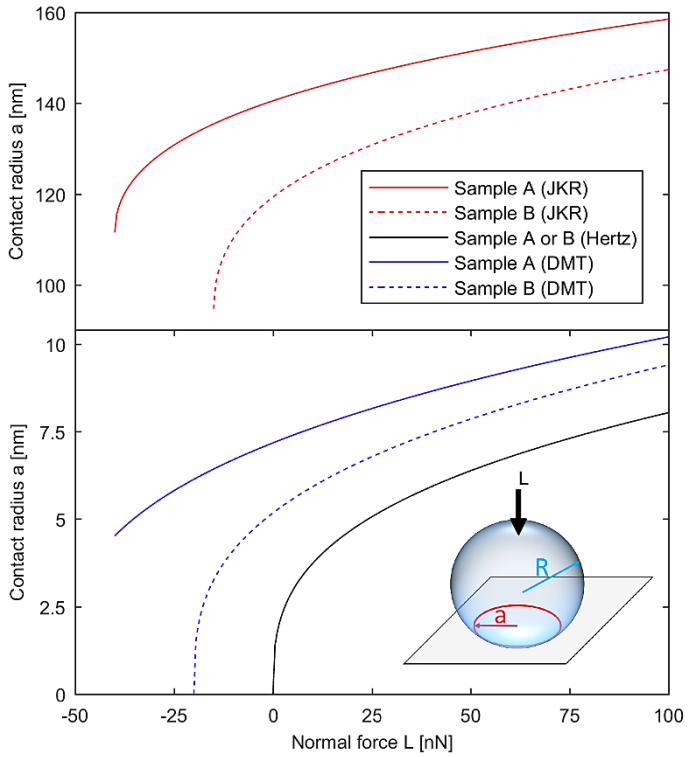

Figure 26 Estimated contact radius *a* as a function of normal force *L* for a silicon nitride tip with radius of curvature of 40 *nm* as obtained using Hertz, DMT, and JKR contact mechanics models.

CHAPTER IV

SUMMARY AND CONCLUSIONS

The friction of fibrous assemblies was studied with a sliding friction experiment. The friction coefficient μ was calculated by fitting the data to the $F_f = \bar{\mu}L$ model. In the first set of experiments, five samples of approximately parallel fiber (card sliver samples) were tested. Two sleds with different apparent contact area were used; the samples had the same ranking in terms of μ in both methods. Other physical and dimensional properties of fibers were measured with HVI, AFIS, and SEM. The fiber width measured with the SEM was in agreement with the AFIS fineness measurement. Relationships between fiber dimensional properties and friction can be summarized in the following expression: $F_f \propto S_0 \propto 1/\sqrt{\theta H} \propto 1/\sqrt{Q}$. These partial relationships were confirmed theoretically using the fiber simulation model, which computes the real contact area of a given mass of fibrous assembly as a function of the dimensional properties of its constituent fibers. The fiber simulation model showed that fiber assemblies with more immature and smaller radius fibers, under constant fiber length and mass, are associated with higher contact area and a larger number of fibers in their structure. Our experimental investigation also indicated a significant, negative, linear correlation between μ and $+b$ value (R^2 = 0.90). The $+b$ indicates the degree of fiber yellowness. In this study, the fiber $+b$ value was considered as possibly related to the amount of the waxy layer on fiber surface. Furthermore, a strong, positive correlation was observed between μ and SFC (R^2 = 0.92). The SFC can be interpreted as an indirect measurement of fiber propensity to break during processing. It was reasoned that fibers with higher

friction likely have greater propensity to break during processing, thus potentially explaining the relationship between friction and SFC. In the second set of experiments, 48 samples of randomly oriented fiber (ginned samples) were tested. Samples from this study were obtained from a small-plot replicated trial with varying genetic traits but similar growth conditions. Results indicated that frictional characteristics of cotton fibers varied significantly among varieties. The friction coefficient of ginned fiber samples varied from 0.065 to 0.082, on the order of ten times greater than that of the card sliver samples, likely due to the random orientation of the fibers in this case. A multiple linear regression analysis was used to study the relationships between fiber physical properties and friction in this larger data set. In addition to $+b$ (an indicator of fiber surface properties) and Micronaire (an indicator of fiber dimensional properties), fiber elongation (an indicator of fiber mechanical properties) was also found to be significantly related to friction. The proportional contributions of these properties to friction were considered. Elongation and $+b$ accounted for ~65% of the variation in fiber friction. It can be concluded that the sliding friction of a cotton fiber assembly is a complex phenomenon, which involves multiple friction mechanisms such as adhesion, deformation, and lubrication. For future studies, friction experiments can be conducted on fibers with different level of moisture content to better simulate industrial-scale ginning process.

In order to better understand the origin of cotton fiber friction, fiber nanotribological properties were investigated with an AFM instrument. Eight fibers each were tested from two different cotton varieties that were quite distinct in terms of their macroscale

frictional properties. The surface topography of the fibers was analyzed in both Contact and Force Tapping modes. The surface of both fiber types was characterized by a series of furrows and ridges, while the surface of fibers with lower macroscale friction (sample B) was also characterized by certain granular-like surface deposits. Surface nanotribological properties of the fibers were examined under various normal forces. Differences in fiber nanofriction were more apparent under higher normal forces. Fibers from sample B with lower macroscale friction were also characterized by lower nanoscale friction. Differences in nanofrictional properties under higher normal forces may be due to changes in fiber surface hydrophilicity as a result of the cuticle layer removal. Since the increase in nanofriction as a function of normal force was not as significant for sample B fibers, these fiber may be covered with a thicker layer of cuticular materials. The nanoscale adhesion and deformation of the fibers were also investigated in Force Tapping mode. Fibers from sample B were characterized with lower average adhesion, possibly due to their lower hydrophilicity. The lower surface deformation of the sample B fibers was attributed to both the biophysical properties of their cuticle layer, which makes their surface stiffer, or possibly their lower surface hydrophilicity, which would increase the attractive forces. By measuring the average adhesion energy for both samples, it was possible to estimate the real contact area between the probe and the fibers as a function of normal force. While different contact mechanics models estimated different values for the real contact area, it was shown that, under any model, fibers from sample B are characterized with smaller contact radius.

REFERENCES

1 W. S. Anthony and W. D. Mayfield, *Cotton ginners handbook*. United States Department of Agriculture, Agricultural Research Service, 1994.

2 J. A. Thomasson and S. A. Shearer, "Correlation of NIR data with cotton quality characteristics.," *Trans. ASAE*, vol. 38, pp. 1005–1010, Jul. 1995.

3 R. Sui, J. A. Thomasson, Y. Ge, and C. Morgan, "Multispectral Sensor For In-Situ Cotton Fiber Quality Measurement," *Trans. ASABE*, vol. 51, no. 6, pp. 2201–2208, Nov. 2008.

4 M. Shahriar, I. Scott-Fleming, H. Sari-Sarraf, and E. Hequet, "A machine vision system to estimate cotton fiber maturity from longitudinal view using a transfer learning approach," *Mach. Vis. Appl.*, vol. 24, no. 8, pp. 1661–1683, Nov. 2013.

5 A. C. Griffin and V. P. Moore, "Relation of Physical Properties of Cotton to Commerce and Ginning Research," *Trans. ASAE*, vol. 8, no. 4, pp. 0488–0490, 1965.

6 V. L. Stedronsky, "Ginning Processes and Their Effects on Cotton Quality," *Trans. ASAE*, vol. 9, no. 2, pp. 0282–0283, 1966.

7 R. E. Childers and R. V. Baker, "Effect of Moisture Conditioning on Ginning Performance and Fiber Quality of High Plains Cotton," *Trans. ASAE*, vol. 21, no. 2, pp. 0379–0384, 1978.

8 W. S. Anthony and C. K. Bragg, "Response of Cotton Fiber Length Distribution to Production and Ginning Practices," *Trans. ASAE*, vol. 30, no. 1, pp. 0290–0296, 1987.

9 W. S. Anthony, "Cotton Length Uniformity and Short Fiber Content," *Trans. ASAE*, vol. 35, no. 2, pp. 443–449, 1992.

10 W. S. Anthony, "Impact of Cotton Gin Machinery Sequences on Fiber Value and Quality," *Appl. Eng. Agric.*, vol. 12, no. 3, pp. 351–363, 1996.

11 F. Hosseinali, “Investigation on the tensile properties of individual cotton (Gossypium hirsutum L.) fibers,” Texas Tech University, 2012.

12 G. J. Mangialardi, “Lint Cleaning at Cotton Gins,” *Cott. Gin Oil Mill Press*, vol. 89, no. 23, p. 8, Nov. 1988.

13 S. E. Hughs, C. B. Armijo, and J. A. Foulk, “Upland fiber changes due to ginning and lint cleaning,” *J. Cotton Sci.*, vol. 17, no. 2, pp. 115–124, 2013.

14 R. Sui, J. A. Thomasson, R. K. Byler, J. C. Boykin, and E. M. Barnes, “Effect of machine-fiber interaction on cotton fiber quality and foreign-matter particle attachment to fiber,” *J. Cotton Sci.*, vol. 153, pp. 145–153, 2010.

15 W. S. Anthony and E. P. Columbus, “Principles of Dust Removal in Gin Machinery: Theoretical and Measured,” *J. Eng. Ind.*, vol. 107, no. 3, p. 288, 1985.

16 E. P. Columbus, “Principle Forces Applied to Fine Dust in Lint Cleaners,” *Trans. ASAE*, vol. 28, no. 6, pp. 2042–2046, 1985.

17 G. L. Barker and R. V. Baker, “Prediction of Cotton Quality as a Function of Lint Cleaner Operating Parameters,” *Trans. ASAE*, vol. 29, no. 3, pp. 0702–0706, 1986.

18 R. V. Baker, “Performance Characteristics of Saw-Type Lint Cleaners,” *Trans. ASAE*, vol. 21, no. 6, pp. 1081–1087, 1978.

19 R. V. Baker, J. D. Towery, and J. B. Cocke, “Effects of Lint-Cleaner Combing Ratio and Suction Nozzles on Cotton Dust Levels in Processing,” *Text. Res. J.*, vol. 51, no. 8, pp. 497–502, Aug. 1981.

20 C. G. Leonard, T. E. Wright, and S. E. Hughs, “Lint Cotton Cleaners with Notched Grid Bars,” *Trans. ASAE*, vol. 25, no. 1, pp. 0204–0209, 1982.

21 E. P. Columbus, “Effect of Lint Cleaner Saw Speed and Tooth Density on Cotton Quality,” *Trans. ASAE*, vol. 28, no. 5, pp. 1692–1696, 1985.

22 R. V. Baker and A. D. Brashears, “Effects of Grid and Saw Variables on Lint Cleaner Performance,” *Trans. ASAE*, vol. 32, no. 4, pp. 1138–1142, 1989.

23 G. J. Mangialardi Jr., “Alternate Carding and Combing Procedures for Cotton Lint Cleaners,” *Appl. Eng. Agric.*, vol. 11, no. 6, pp. 801–810, 1995.

24 S. Le, “Fiber Quality Properties Produced by Saw-Type Lint Cleaners,” *Appl. Eng. Agric.*, vol. 23, no. 2, pp. 125–130, 2007.

25 S. G. Gordon, K. M. Bagshaw, and F. A. Horne, “The Effect of Lint Cleaner Elements, Settings, and Fiber Moisture Content on Fiber Quality,” *Trans. ASABE*, vol. 54, no. 6, pp. 2267–2278, 2011.

26 J. K. Dever, J. R. Gannaway, and R. V. Baker, “Influence of cotton fiber strength and fineness on fiber damage during Lint cleaning,” *Text. Res. J.*, vol. 58, no. 8, pp. 433–438, 1988.

27 G. J. Mangialardi and W. F. Lalor, “PROPENSITY OF COTTON VARIETIES TO NEPPINESS,” *Trans. ASAE*, vol. 33, no. 6, pp. 1748–1758, 1990.

28 S. E. Hughs, W. F. Lalor, and F. T. Wahba, “Relationship of Ginning and Fiber Properties to Dyeing Imperfections,” *Text. Res. J.*, vol. 58, no. 10, pp. 557–565, Oct. 1988.

29 J. N. Israelachvili, *Intermolecular and surface forces*. Academic Press, 1992.

30 J. Gao, W. D. Luedtke, D. Gourdon, M. Ruths, J. N. Israelachvili, and U. Landman, “Frictional forces and Amontons’ law: From the molecular to the macroscopic scale,” *J. Phys. Chem. B*, vol. 108, no. 11, pp. 3410–3425, Mar. 2004.

31 A. M. Homola, J. N. Israelachvili, P. M. McGuiggan, and M. L. Gee, “Fundamental experimental studies in tribology: The transition from ‘interfacial’ friction of undamaged molecularly smooth surfaces to ‘normal’ friction with wear,” *Wear*, vol. 136, no. 1, pp. 65–83, Feb. 1990.

32 D. Tabor, “Friction, Adhesion and Boundary Lubrication of Polymers,” in *Advances in Polymer Friction and Wear*, Boston, MA: Springer US, 1974, pp. 5–30.

33 L.-H. Lee, “Effect of Surface Energetics on Polymer Friction and Wear,” in *Advances in Polymer Friction and Wear*, Boston, MA: Springer US, 1974, pp. 31–68.

34 H. Zeng, “Adhesion and Friction Mechanisms of Polymer Surfaces and Thin Films,” in *Polymer Adhesion, Friction, and Lubrication*, Hoboken, NJ, USA: John Wiley & Sons, Inc., 2013, pp. 391–442.

35 W. G. Sawyer, N. Argibay, D. L. Burris, and B. A. Krick, “Mechanistic Studies in Friction and Wear of Bulk Materials,” *Annu. Rev. Mater. Res.*, vol. 44, no. 1, pp. 395–427, Jul. 2014.

36 S. Bahadur, “The development of transfer layers and their role in polymer tribology,” *Wear*, vol. 245, no. 1–2, pp. 92–99, Oct. 2000.

37 K. R. MAKINSON and D. TABOR, “Friction and Transfer of Polytetrafluoroethylene,” *Nature*, vol. 201, no. 4918, pp. 464–466, Feb. 1964.

38 S. K. Biswas and K. Vijayan, “Friction and wear of PTFE — a review,” *Wear*, vol. 158, no. 1–2, pp. 193–211, Oct. 1992.

39 B. N. J. Persson, “Theory of rubber friction and contact mechanics,” *J. Chem. Phys.*, vol. 115, no. 8, pp. 3840–3861, Aug. 2001.

40 S. Nak-Ho and N. P. Suh, “Effect of fiber orientation on friction and wear of fiber reinforced polymeric composites,” *Wear*, vol. 53, no. 1, pp. 129–141, Mar. 1979.

41 D. L. Burris and W. G. Sawyer, “A low friction and ultra low wear rate PEEK/PTFE composite,” *Wear*, vol. 261, no. 3–4, pp. 410–418, Aug. 2006.

42 S. Bahadur and D. Gong, “The action of fillers in the modification of the tribological behavior of polymers,” *Wear*, vol. 158, no. 1–2, pp. 41–59, Oct. 1992.

43 D. L. Burris, B. Boesl, G. R. Bourne, and W. G. Sawyer, “Polymeric Nanocomposites for Tribological Applications,” *Macromol. Mater. Eng.*, vol. 292, no. 4, pp. 387–402, Apr. 2007.

44 J. P. Gong *et al.*, “Friction and lubrication of hydrogels—its richness and complexity,” *Soft Matter*, vol. 2, no. 7, pp. 544–552, 2006.

45 L. J. T. Landherr, C. Cohen, P. Agarwal, and L. A. Archer, “Interfacial Friction and Adhesion of Polymer Brushes,” *Langmuir*, vol. 27, no. 15, pp. 9387–9395, Aug. 2011.

46 D. W. Lee, X. Banquy, and J. N. Israelachvili, “Stick-slip friction and wear of articular joints.,” *Proc. Natl. Acad. Sci. U. S. A.*, vol. 110, no. 7, pp. E567–74, Feb. 2013.

47 J. Yu, S. Chary, S. Das, J. Tamelier, K. L. Turner, and J. N. Israelachvili, “Friction and Adhesion of Gecko-Inspired PDMS Flaps on Rough Surfaces,” *Langmuir*, vol. 28, no. 31, pp. 11527–11534, Aug. 2012.

48 T. Kang *et al.*, “Mussel-Inspired Anchoring of Polymer Loops That Provide Superior Surface Lubrication and Antifouling Properties.,” *ACS Nano*, vol. 10, no. 1, pp. 930–7, Jan. 2016.

49 H. Jiang, R. Browning, J. Fincher, A. Gasbarro, S. Jones, and H.-J. Sue, “Influence of surface roughness and contact load on friction coefficient and scratch behavior of thermoplastic olefins,” *Appl. Surf. Sci.*, vol. 254, no. 15, pp. 4494–4499, 2008.

50 H. Jiang, R. Browning, and H.-J. Sue, “Understanding of scratch-induced damage mechanisms in polymers,” *Polymer (Guildf).*, vol. 50, no. 16, pp. 4056–4065, 2009.

51 J. A. Greenwood and J. H. Tripp, “The contact of two nominally flat rough surfaces,” *Arch. Proc. Inst. Mech. Eng. 1847-1982 (vols 1-196)*, vol. 185, no. 1970, pp. 625–634, Jun. 1970.

52 D. Tabor, “Surface forces and surface interactions,” *J. Colloid Interface Sci.*, vol.

58, no. 1, pp. 2–13, Jan. 1977.

53 M. Benz, K. J. Rosenberg, E. J. Kramer, and J. N. Israelachvili, “The Deformation and Adhesion of Randomly Rough and Patterned Surfaces,” *J. Phys. Chem. B*, vol. 110, no. 24, pp. 11884–11893, Jun. 2006.

54 M. Urbakh, J. Klafter, D. Gourdon, and J. Israelachvili, “The nonlinear nature of friction,” *Nature*, vol. 430, no. 6999, pp. 525–528, Jul. 2004.

55 N. Maeda, N. Chen, M. Tirrell, and J. N. Israelachvili, “Adhesion and friction mechanisms of polymer-on-polymer surfaces.,” *Science*, vol. 297, no. 5580, pp. 379–82, Jul. 2002.

56 H. R. Brown, “Chain Pullout and Mobility Effects in Friction and Lubrication,” *Science (80-.).*, vol. 263, no. 5152, pp. 1411–1413, Mar. 1994.

57 N. Chen, N. Maeda, M. Tirrell, and J. Israelachvili, “Adhesion and Friction of Polymer Surfaces: The Effect of Chain Ends,” *Macromolecules*, vol. 38, no. 8, pp. 3491–3503, Apr. 2005.

58 H. Zeng, N. Maeda, N. Chen, M. Tirrell, and J. Israelachvili, “Adhesion and Friction of Polystyrene Surfaces around T_g,” *Macromolecules*, vol. 39, no. 6, pp. 2350–2363, Mar. 2006.

59 H. G. Howell, “The laws of static friction,” *Text. Res. J.*, vol. 23, no. 8, pp. 589–591, Aug. 1953.

60 H. G. Howell and J. Mazur, “Amontons’ law and fibre friction,” *J. Text. Inst. Trans.*, vol. 44, no. 2, pp. T59–T69, Feb. 1953.

61 H. G. Howell, “The laws of friction,” *Nature*, vol. 171, no. 4344, pp. 220–220, Jan. 1953.

62 Y. E. El Mogahzy and B. S. Gupta, “Friction in fibrous materials,” *Text. Res. J.*, vol. 63, no. 4, pp. 219–230, Apr. 1993.

63 B. S. Gupta and Y. E. El Mogahzy, “Friction in Fibrous Materials: Part I: Structural Model,” *Text. Res. J.*, vol. 61, no. 9, pp. 547–555, Sep. 1991.

64 B. Lincoln, “Frictional and Elastic Properties of High Polymeric Materials,” *Br. J. Appl. Phys.*, vol. 3, no. 8, pp. 260–263, Aug. 1952.

65 J. F. Archard, “Elastic Deformation and the Laws of Friction,” *Proc. R. Soc. A Math. Phys. Eng. Sci.*, vol. 243, no. 1233, pp. 190–205, Dec. 1957.

66 B. Cornelissen, M. B. de Rooij, B. Rietman, and R. Akkerman, “Frictional behavior of carbon fiber tows: a contact mechanics model of tow–tow friction,” *Text. Res. J.*, vol. 84, no. 14, pp. 1476–1488, Sep. 2014.

67 B. Cornelissen, M. B. de Rooij, B. Rietman, and R. Akkerman, “Frictional behaviour of high performance fibrous tows: A contact mechanics model of tow–metal friction,” *Wear*, vol. 305, no. 1–2, pp. 78–88, Jul. 2013.

68 K. L. Johnson, K. Kendall, and A. D. Roberts, “Surface Energy and the Contact of Elastic Solids,” *Proc. R. Soc. A Math. Phys. Eng. Sci.*, vol. 324, no. 1558, pp. 301–313, Sep. 1971.

69 J. H. Langston and W. T. Rainey, “A Literature Survey on Fiber Friction,” *Text. Res. J.*, vol. 24, no. 7, pp. 643–653, Jul. 1954.

70 S. S. Ramkumar, R. Rajanala, S. Parameswaran, A. K. Sarkar, and A. P. S. Sawhney, “Frictional Characterization of Polymeric Materials--A Review.,” *AATCC Rev.*, vol. 5, no. 2, pp. 17–20, Feb. 2005.

71 M. W. E. and H. J. W. S., “Physical Properties of Textile Fibers.,” *Phys. Prop. Text. Fibers*, 1993.

72 H. G. Howell, *Friction in Textiles*. Textile Book Publishers in association with the Textile Institute, 1959.

73 B. S. (Bhupender S. . Gupta, *Friction in textile materials*. Woodhead Pub, 2008.

74 K. R. Sen and N. Ahmad, “23—THE CLINGING POWER OF SINGLE COTTON FIBRES IN RELATION TO THEIR PHYSICAL PROPERTIES,” *J. Text. Inst. Trans.*, vol. 29, no. 11, pp. T258–T279, Nov. 1938.

75 E. Lord, “FRICTIONAL FORCES BETWEEN FRINGES OF FIBRES,” *J. Text. Inst. Proc.*, vol. 46, no. 1, pp. P41–P58, Jan. 1955.

76 W. F. du Bois, “Frictional Measurements on Fibrous Materials,” *Text. Res. J.*, vol. 29, no. 6, pp. 451–466, Jun. 1959.

77 R. B. Belser and J. Taylor, “Frictional Properties of Cotton Fibers,” Feb. 1968.

78 K. L. Hertel, “Measurement of Fiber Assembly Shear Energy Transformation,” *Text. Res. J.*, vol. 37, no. 5, pp. 433–434, May 1967.

79 A. Viswanathan, “Some experiments on the friction of cotton fibers,” *J. Text. Inst.*, vol. 64, no. 10, pp. 553–557, Oct. 1973.

80 V. Subramaniam, K. Sreenivasan, and K. P. R. Pillay, “Studies in Fibre Friction: Part I-Effect of Friction on Fibre Properties and Processing Performance of Cotton,” *Indian J. Fibre Text. Res.*, pp. 9–15, 1981.

81 V. Subramaniam, K. Sreenivasan, and K. P. R. Pillay, “Studies in Fibre Friction: Part II-Influence of Fibre Friction on Cohesion, Configuration and Evenness of Fibre Assemblies,” *Indian J. Fibre Text. Res.*, pp. 16–21, 1981.

82 Y. El Mogahzy, R. Broughton, H. Hong Guo, and R. A. Taylor, “Evaluating staple fiber processing propensity,” *Text. Res. J.*, vol. 68, no. 11, pp. 835–840, Nov. 1998.

83 G. R. Gamble, “Influence of Surface Electrolyte and Moisture Content on the Frictional Behavior of Cotton Fiber,” *J. Cotton Sci.*, vol. 10, no. 1, pp. 61–67, 2006.

84 S. Nowrouzieh, A. Sinoimeri, J.-Y. Drean, and R. Frydrych, “A new method of measurement of the inter-fiber force,” *Text. Res. J.*, vol. 77, no. 7, pp. 489–494, Jul. 2007.

85 Y. Zhang, Y. Tian, and Y. Meng, “Mechanical interlocking of cotton fibers on slightly textured surfaces of metallic cylinders.,” *Sci. Rep.*, vol. 6, p. 25403, May 2016.

86 A. Viswanathan, “Frictional forces in cotton and regenerated cellulosic fibres,” *J. Text. Inst. Trans.*, vol. 57, no. 1, pp. T30–T41, Jan. 1966.

87 Y. E. El Mogahzy and R. M. Broughton, “A new approach for evaluating the frictional behavior of cotton fibers,” *Text. Res. J.*, vol. 63, no. 8, pp. 465–475, Aug. 1993.

88 C. Roedel and S. S. Ramkumar, “Surface and Mechanical Property Measurements of H Technology Needle-Punched Nonwovens,” *Text. Res. J.*, vol. 73, no. 5, pp. 381–385, May 2003.

89 K. L. Hertel and R. Lawson, “Shear friction within multiple card web specimens,” *Text. Res. J.*, vol. 40, no. 5, pp. 472–477, May 1970.

90 Y. E. El Mogahzy, “Friction and surface characteristics of cotton fibers,” in *Friction in Textile Materials*, B. Gupta, Ed. 2008, pp. 225–252.

91 S. Ghosh, J. E. Rodgers, and A. E. Ortega, “RotorRing measurement of fiber cohesion and bulk properties of staple fibers,” *Text. Res. J.*, vol. 62, no. 10, pp. 608–613, Oct. 1992.

92 M. Lewin, Y. Litav, and M. Shiloh, “Crimp in cotton: Crimp as a new characteristic of cotton fibres,” *Nature*, vol. 196, no. 4850, pp. 152–153, Oct. 1962.

93 A. Hecht and M. Shiloh, “Studies on Cotton Crimp: Part I: Comparisons Between the Crimp Parameters of Twelve Varieties of Cotton1,” *Text. Res. J.*, vol. 35, no. 6, pp. 539–546, Jun. 1965.

94 E. ALEXANDER, Y. LITAV, and H. PERES, “Crimp in Cotton: Some Aspects of the Behaviour of Crimp of Cotton Fibres,” *Nature*, vol. 196, no. 4850, pp. 153–154, Oct. 1962.

95 M. Shiloh and Y. Litav, “Studies on Cotton Crimp: Part II: The Recovery of Crimp of Cotton Fibers After Successive Loadings,” *Text. Res. J.*, vol. 35, no. 6, pp. 546–553, Jun. 1965.

96 E. Alexander, M. Lewin, Y. Litav, H. Peres, and M. Shiloh, “The Crimp of Cotton Fibers,” *Text. Res. J.*, vol. 32, no. 11, pp. 898–908, Nov. 1962.

97 J. Israelachvili *et al.*, “Recent advances in the surface forces apparatus (SFA) technique,” *Reports Prog. Phys.*, vol. 73, no. 3, p. 036601, Mar. 2010.

98 G. Binnig, C. F. Quate, and C. Gerber, “Atomic Force Microscope,” *Phys. Rev. Lett.*, vol. 56, no. 9, pp. 930–933, Mar. 1986.

99 B. Bhushan, J. N. Israelachvili, and U. Landman, “Nanotribology: friction, wear and lubrication at the atomic scale,” *Nature*, vol. 374, no. 6523, pp. 607–616, Apr. 1995.

100 S. S. Perry, “Scanning probe microscopy measurements of friction,” *MRS Bull.*, vol. 29, no. 07, pp. 478–483, Jul. 2004.

101 I. Szlufarska, M. Chandross, and R. W. Carpick, “Recent advances in single-asperity nanotribology,” *J. Phys. D. Appl. Phys.*, vol. 41, no. 12, p. 123001, Jun. 2008.

102 C. Mathew Mate, “On the Road to an Atomic- and Molecular-Level Understanding of Friction,” *MRS Bull.*, vol. 27, no. 12, pp. 967–971, Dec. 2002.

103 B. Bhushan, “Nanotribology and nanomechanics,” *Wear*, vol. 259, no. 7–12, pp. 1507–1531, Jul. 2005.

104 R. W. Carpick and M. Salmeron, “Scratching the Surface: Fundamental Investigations of Tribology with Atomic Force Microscopy,” *Chem. Rev.*, vol. 97, no. 4, pp. 1163–1194, Jun. 1997.

105 Y. Mo, K. T. Turner, and I. Szlufarska, “Friction laws at the nanoscale,” *Nature*,

vol. 457, no. 7233, pp. 1116–1119, Feb. 2009.

106 C. Lee *et al.*, “Frictional Characteristics of Atomically Thin Sheets,” *Science (80-.).*, vol. 328, no. 5974, pp. 76–80, Apr. 2010.

107 N. J. Brewer, B. D. Beake, and G. J. Leggett, “Friction Force Microscopy of Self-Assembled Monolayers: Influence of Adsorbate Alkyl Chain Length, Terminal Group Chemistry, and Scan Velocity,” *Langmuir*, vol. 17, no. 6, pp. 1970–1974, Mar. 2001.

108 V. N. Bliznyuk, M. P. Everson, and V. V. Tsukruk, “Nanotribological Properties of Organic Boundary Lubricants: Langmuir Films Versus Self-Assembled Monolayers,” *J. Tribol.*, vol. 120, no. 3, p. 489, 1998.

109 V. V. Tsukruk and D. H. Reneker, “Scanning probe microscopy of organic and polymeric films: from self-assembled monolayers to composite multilayers,” *Polymer (Guildf).*, vol. 36, no. 9, pp. 1791–1808, Apr. 1995.

110 V. V. Tsukruk, “Scanning Probe Microscopy of Polymer Surfaces,” *Rubber Chem. Technol.*, vol. 70, no. 3, pp. 430–467, Jul. 1997.

111 L. L. Johnson, “Atomic Force Microscopy (AFM) for Rubber,” *Rubber Chem. Technol.*, vol. 81, no. 3, pp. 359–383, Jul. 2008.

112 J.-A. Ruan and B. Bhushan, “Atomic-Scale Friction Measurements Using Friction Force Microscopy: Part I—General Principles and New Measurement Techniques,” *J. Tribol.*, vol. 116, no. 2, p. 378, 1994.

113 B. Bhushan and J.-A. Ruan, “Atomic-Scale Friction Measurements Using Friction Force Microscopy: Part II—Application to Magnetic Media,” *J. Tribol.*, vol. 116, no. 2, p. 389, 1994.

114 G. Haugstad, W. L. Gladfelter, and R. R. Jones, “Nanotribology on a polymer network film,” *J. Vac. Sci. Technol. A Vacuum, Surfaces, Film.*, vol. 14, no. 3, pp. 1864–1869, May 1996.

115 R. Nisman, P. Smith, and G. J. Vancso, “Anisotropic Friction at the Surface of

Lamellar Crystals of Poly(oxymethylene) by Lateral Force Microscopy," *Langmuir*, vol. 10, no. 6, pp. 1667–1669, Jun. 1994.

116 B. Bhushan and V. N. Koinkar, "Microtribology of PET Polymeric Films," *Tribol. Trans.*, vol. 38, no. 1, pp. 119–127, Jan. 1995.

117 D.-H. Cho and B. Bhushan, "Nanofriction and nanowear of polypropylene, polyethylene terephthalate, and high-density polyethylene during sliding," *Wear*, vol. 352–353, pp. 18–23, Apr. 2016.

118 A. Kumar and B. Bhushan, "Effect of Nanoparticles on Nanomechanical and Nanotribological Properties of Polyethylene Blend Films," *Macromol. React. Eng.*, vol. 7, no. 10, pp. 538–548, Oct. 2013.

119 N. S. Tambe and B. Bhushan, "Scale dependence of micro/nano-friction and adhesion of MEMS/NEMS materials, coatings and lubricants," *Nanotechnology*, vol. 15, no. 11, pp. 1561–1570, Nov. 2004.

120 G. Bogdanovic, F. Tiberg, and M. W. Rutland, "Sliding Friction between Cellulose and Silica Surfaces," *Langmuir*, vol. 17, no. 19, pp. 5911–5916, Sep. 2001.

121 N. Nordgren, P. Eronen, M. Österberg, J. Laine, and M. W. Rutland, "Mediation of the Nanotribological Properties of Cellulose by Chitosan Adsorption," *Biomacromolecules*, vol. 10, no. 3, pp. 645–650, Mar. 2009.

122 G. Haugstad, W. L. Gladfelter, E. B. Weberg, R. T. Weberg, and T. D. Weatherill, "Probing Biopolymers with Scanning Force Methods: Adsorption, Structure, Properties, and Transformation of Gelatin on Mica," *Langmuir*, vol. 10, no. 11, pp. 4295–4306, Nov. 1994.

123 G. Haugstad, W. L. Gladfelter, E. B. Weberg, R. T. Weberg, and R. R. Jones, "Probing molecular relaxation on polymer surfaces with friction force microscopy," *Langmuir*, vol. 11, no. 9, pp. 3473–3482, Sep. 1995.

124 G. Haugstad, W. L. Gladfelter, and R. R. Jones, "Nanotribology on a polymer network film," *J. Vac. Sci. Technol. A Vacuum, Surfaces, Film.*, vol. 14, no. 3, pp.

1864–1869, May 1996.

125 T. Kajiyama, K. Tanaka, and A. Takahara, “Surface Molecular Motion of the Monodisperse Polystyrene Films,” *Macromolecules*, vol. 30, no. 2, pp. 280–285, Jan. 1997.

126 K. Tanaka, A. Takahara, and T. Kajiyama, “Effect of Polydispersity on Surface Molecular Motion of Polystyrene Films,” *Macromolecules*, vol. 30, no. 21, pp. 6626–6632, Oct. 1997.

127 J. A. Hammerschmidt, B. Moasser, W. L. Gladfelter, G. Haugstad, and R. R. Jones, “Polymer Viscoelastic Properties Measured by Friction Force Microscopy,” *Macromolecules*, vol. 29 , no. 27, pp. 8996–8998, 1996.

128 J. A. Hammerschmidt, W. L. Gladfelter, and G. Haugstad, “Probing Polymer Viscoelastic Relaxations with Temperature-Controlled Friction Force Microscopy,” *Macromolecules*, vol. 32, no. 10, pp. 3360–3367, May 1999.

129 G. Haugstad, J. A. Hammerschmidt, and W. L. Gladfelter, “Viscoelasticity in Nanoscale Friction on Thin Polymer Films,” in *Interfacial Properties on the Submicrometer Scale*, J. Frommer and R. M. Overney, Eds. ACS Symposium Series, 2000, pp. 230–253.

130 F. Ahimou, M. J. Semmens, P. J. Novak, and G. Haugstad, “Biofilm cohesiveness measurement using a novel atomic force microscopy methodology.,” *Appl. Environ. Microbiol.*, vol. 73, no. 9, pp. 2897–904, May 2007.

131 S. Aoyama, Y. T. Park, C. W. Macosko, T. Ougizawa, and G. Haugstad, “AFM Probing of Polymer/Nanofiller Interfacial Adhesion and Its Correlation with Bulk Mechanical Properties in a Poly(ethylene terephthalate) Nanocomposite,” *Langmuir*, vol. 30, no. 43, pp. 12950–12959, Nov. 2014.

132 B. Bhushan and Y. C. Jung, “Micro- and nanoscale characterization of hydrophobic and hydrophilic leaf surfaces,” *Nanotechnology*, vol. 17, no. 11, pp. 2758–2772, Jun. 2006.

133 Z. Zhang *et al.*, “Morphological and quantitative frictional measurements of

cotton fibres using friction force microscopy," *J. Mater. Chem.*, vol. 20, no. 39, p. 8531, 2010.

134 H.-J. Butt, B. Cappella, and M. Kappl, "Force measurements with the atomic force microscope: Technique, interpretation and applications," *Surf. Sci. Rep.*, vol. 59, no. 1–6, pp. 1–152, Oct. 2005.

135 N. A. Burnham, R. J. Colton, and H. M. Pollock, "Interpretation of force curves in force microscopy," *Nanotechnology*, vol. 4, no. 2, pp. 64–80, Apr. 1993.

136 D. Leckband and J. Israelachvili, "Intermolecular forces in biology," *Q. Rev. Biophys.*, vol. 34, no. 02, p. 105, May 2001.

137 M. E. McConney, S. Singamaneni, and V. V. Tsukruk, "Probing Soft Matter with the Atomic Force Microscopies: Imaging and Force Spectroscopy," *Polym. Rev.*, vol. 50, no. 3, pp. 235–286, Jul. 2010.

138 B. Cappella, "Mechanical Properties and Adhesion of a Micro Structured Polymer Blend," *Polymers (Basel).*, vol. 3, no. 4, pp. 1091–1106, Jul. 2011.

139 A. Alessandrini and P. Facci, "AFM: a versatile tool in biophysics," *Meas. Sci. Technol.*, vol. 16, no. 6, pp. R65–R92, Jun. 2005.

140 W. F. Heinz and J. H. Hoh, "Spatially resolved force spectroscopy of biological surfaces using the atomic force microscope.," *Trends Biotechnol.*, vol. 17, no. 4, pp. 143–50, Apr. 1999.

141 P. Milani, S. A. Braybrook, and A. Boudaoud, "Shrinking the hammer: micromechanical approaches to morphogenesis," *J. Exp. Bot.*, vol. 64, no. 15, pp. 4651–4662, Nov. 2013.

142 D. W. Ehrhardt and W. B. Frommer, "New technologies for 21st century plant science.," *Plant Cell*, vol. 24, no. 2, pp. 374–94, Feb. 2012.

143 J. D. Batteas and R. E. Stark, "Surface and interfacial studies of plant biopolymers," in *Molecular Interfacial Phenomena of Polymers and Biopolymers*, Elsevier, 2005, pp. 580–608.

144 J. D. Batteas, X. Quan, and M. K. Weldon, “Adhesion and wear of colloidal silica probed by force microscopy,” *Tribol. Lett.*, vol. 7, no. 2/3, pp. 121–128, 1999.

145 A. Kawai, H. Nagata, and M. Takata, “Characterization of Surface Energetic Behavior by Atomic Force Microscopy,” *Jpn. J. Appl. Phys.*, vol. 31, no. Part 2, No. 7B, pp. L977–L979, Jul. 1992.

146 G. S. Blackman, C. M. Mate, and M. R. Philpott, “Interaction forces of a sharp tungsten tip with molecular films on silicon surfaces,” *Phys. Rev. Lett.*, vol. 65, no. 18, pp. 2270–2273, Oct. 1990.

147 C. M. Mate, M. R. Lorenz, and V. J. Novotny, “Atomic force microscopy of polymeric liquid films,” *J. Chem. Phys.*, vol. 90, no. 12, pp. 7550–7555, Jun. 1989.

148 B. Bhushan and C. Dandavate, “Thin-film friction and adhesion studies using atomic force microscopy,” *J. Appl. Phys.*, vol. 87, no. 3, pp. 1201–1210, Feb. 2000.

149 H. A. Mizes, K. -G. Loh, R. J. D. Miller, S. K. Ahuja, and E. F. Grabowski, “Submicron probe of polymer adhesion with atomic force microscopy: Dependence on topography and material inhomogeneities,” *Appl. Phys. Lett.*, vol. 59, no. 22, pp. 2901–2903, Nov. 1991.

150 L. Sirghi, N. Nakagiri, K. Sugisaki, H. Sugimura, and O. Takai, “Effect of Sample Topography on Adhesive Force in Atomic Force Spectroscopy Measurements in Air,” *Langmuir*, vol. 16, no. 20, pp. 7796–7800, Oct. 2000.

151 P. Eaton, F. F. Estarlich, R. J. Ewen, T. G. Nevell, J. R. Smith, and J. Tsibouklis, “Combined Nanoindentation and Adhesion Force Mapping Using the Atomic Force Microscope: Investigations of a Filled Polysiloxane Coating,” *Langmuir*, vol. 18, no. 25, pp. 10011–10015, Dec. 2002.

152 P. Eaton, J. R. Smith, P. Graham, J. D. Smart, T. G. Nevell, and J. Tsibouklis, “Adhesion Force Mapping of Polymer Surfaces: Factors Influencing Force of Adhesion,” *Langmuir*, vol. 18, no. 8, pp. 3387–3389, Apr. 2002.

153 P. J. Eaton, P. Graham, J. R. Smith, J. D. Smart, T. G. Nevell, and J. Tsibouklis, "Mapping the Surface Heterogeneity of a Polymer Blend: An Adhesion-Force-Distribution Study Using the Atomic Force Microscope," *Langmuir*, vol. 16, no. 21, pp. 7887–7890, Oct. 2000.

154 P. Begat, D. A. V. Morton, J. N. Staniforth, and R. Price, "The Cohesive-Adhesive Balances in Dry Powder Inhaler Formulations I: Direct Quantification by Atomic Force Microscopy," *Pharm. Res.*, vol. 21, no. 9, pp. 1591–1597, Sep. 2004.

155 V. Mangipudi, M. Tirrell, and A. V. Pcius, "Direct measurement of molecular level adhesion between poly(ethylene terephthalate) and polyethylene films: determination of surface and interfacial energies," *J. Adhes. Sci. Technol.*, vol. 8, no. 11, pp. 1251–1270, Jan. 1994.

156 W. W. Merrill, A. V. Pocius, B. V. Thakker, and M. Tirrell, "Direct measurement of molecular level adhesion forces between biaxially oriented solid polymer films," *Langmuir*, vol. 7, no. 9, pp. 1975–1980, Sep. 1991.

157 M. Tirrell, "Measurement of Interfacial Energy at Solid Polymer Surfaces †," *Langmuir*, vol. 12, no. 19, pp. 4548–4551, Jan. 1996.

158 D. R. Baselt and J. D. Baldeschwieler, "Imaging spectroscopy with the atomic force microscope," *J. Appl. Phys.*, vol. 76, no. 1, pp. 33–38, Jul. 1994.

159 A. Rosa-Zeiser, E. Weilandt, S. Hild, and O. Marti, "The simultaneous measurement of elastic, electrostatic and adhesive properties by scanning force microscopy: pulsed-force mode operation," *Meas. Sci. Technol.*, vol. 8, no. 11, pp. 1333–1338, Nov. 1997.

160 C. A. Rezende, L.-T. Lee, and F. Galembeck, "Surface Mechanical Properties of Thin Polymer Films Investigated by AFM in Pulsed Force Mode," *Langmuir*, vol. 25, no. 17, pp. 9938–9946, Sep. 2009.

161 M. Chyasnavichyus, S. L. Young, and V. V. Tsukruk, "Mapping micromechanical properties of soft polymer contact lenses," *Polymer (Guildf).*, vol. 55, no. 23, pp.

6091–6101, 2014.

162 B. Foster, “New Atomic Force Microscopy (AFM) Approaches Life Sciences Gently, Quantitatively, and Correlatively,” *Am. Lab.*, vol. 44, no. 4, p. 24, 2012.

163 S. Zhang, H. Aslan, F. Besenbacher, and M. Dong, “Quantitative biomolecular imaging by dynamic nanomechanical mapping.,” *Chem. Soc. Rev.*, vol. 43, no. 21, pp. 7412–29, Nov. 2014.

164 Y. F. Dufrêne, D. Martínez-Martín, I. Medalsy, D. Alsteens, and D. J. Müller, “Multiparametric imaging of biological systems by force-distance curve–based AFM,” *Nat. Methods*, vol. 10, no. 9, pp. 847–854, Aug. 2013.

165 H. Bargel, K. Koch, Z. Cerman, and C. Neinhuis, “Structure–function relationships of the plant cuticle and cuticular waxes — a smart material?,” *Funct. Plant Biol.*, vol. 33, no. 10, p. 893, 2006.

166 E. Domínguez, J. Cuartero, and A. Heredia, “An overview on plant cuticle biomechanics,” *Plant Sci.*, vol. 181, no. 2, pp. 77–84, Aug. 2011.

167 E. Domínguez, J. A. Heredia-Guerrero, and A. Heredia, “The biophysical design of plant cuticles: an overview,” *New Phytol.*, vol. 189, no. 4, pp. 938–949, Mar. 2011.

168 V. Mirabet, P. Das, A. Boudaoud, and O. Hamant, “The Role of Mechanical Forces in Plant Morphogenesis,” *Annu. Rev. Plant Biol.*, vol. 62, no. 1, pp. 365–385, Jun. 2011.

169 K. Koch, C. Neinhuis, H. Ensikat, and W. Barthlott, “Self assembly of epicuticular waxes on living plant surfaces imaged by atomic force microscopy (AFM),” *J. Exp. Bot.*, vol. 55, no. 397, pp. 711–718, Jan. 2004.

170 A. N. Round, A. J. MacDougall, S. G. Ring, and V. J. Morris, “Unexpected branching in pectin observed by atomic force microscopy,” *Carbohydr. Res.*, vol. 303, no. 3, pp. 251–253, Sep. 1997.

171 A. N. Round, N. M. Rigby, A. J. MacDougall, S. G. Ring, and V. J. Morris,

"Investigating the nature of branching in pectin by atomic force microscopy and carbohydrate analysis," 2001.

172 S. Chatterjee, S. Sarkar, J. Oktawiec, Z. Mao, O. Niitsoo, and R. E. Stark, "Isolation and biophysical study of fruit cuticles.," *J. Vis. Exp.*, no. 61, Mar. 2012.

173 A. N. Round, B. Yan, S. Dang, R. Estephan, R. E. Stark, and J. D. Batteas, "The Influence of Water on the Nanomechanical Behavior of the Plant Biopolyester Cutin as Studied by AFM and Solid-State NMR," *Biophys. J.*, vol. 79, no. 5, pp. 2761–2767, 2000.

174 J. D. Batteas and R. E. Stark, "16 – Surface and interfacial studies of plant biopolymers," in *Molecular Interfacial Phenomena of Polymers and Biopolymers*, 2005, pp. 580–608.

175 A. E. Flint, "The structure and development of the cotton fibre," *Biol. Rev.*, vol. 25, no. 4, pp. 414–434, Oct. 1950.

176 M. M. Hartzell-Lawson and Y.-L. Hsieh, "Characterizing the noncellulosics in developing cotton fibers," *Text. Res. J.*, vol. 70, no. 9, pp. 810–819, Sep. 2000.

177 K. C. Vaughn and R. B. Turley, "The primary walls of cotton fibers contain an ensheathing pectin layer," *Protoplasma*, vol. 209, no. 3–4, pp. 226–237, Sep. 1999.

178 D. E. Brushwood, "Noncellulosic constituents on raw cotton and their relationship to fiber physical properties," *Text. Res. J.*, vol. 73, no. 10, pp. 912–916, Oct. 2003.

179 G. R. Gamble, "Variation in Surface Chemical Constituents of Cotton (*Gossypium hirsutum*) Fiber as a Function of Maturity," *J. Agric. Food Chem.*, vol. 51, no. 27, pp. 7995–7998, Dec. 2003.

180 X. L. Cui, J. B. Price, T. A. Calamari, J. M. Hemstreet, and W. Meredith, "Cotton Wax and Its Relationship with Fiber and Yarn Properties," *Text. Res. J.*, vol. 72, no. 5, pp. 399–404, May 2002.

181 P. B. Marsh, H. D. Barker, T. Kerr, and M. L. Butler, "Wax Content as Related to

Surface Area of Cotton Fibers," *Text. Res. J.*, vol. 20, no. 5, pp. 288–297, May 1950.

182 J. M. Maxwell, S. G. Gordon, and M. G. Huson, "Internal Structure of Mature and Immature Cotton Fibers Revealed by Scanning Probe Microscopy," *Text. Res. J.*, vol. 73, no. 11, pp. 1005–1012, Nov. 2003.

183 S. K. Koc, "Applications of Atomic Force Microscopy in Textiles," *J. Eng. Fibers Fabr.*, vol. 10, no. 1, pp. 169–173, 2015.

184 T. C. Pesacreta, L. C. Carlson, and B. A. Triplett, "Atomic force microscopy of cotton fiber cell wall surfaces in air and water: quantitative and qualitative aspects," *Planta*, vol. 202, no. 4, pp. 435–442, Jul. 1997.

185 I. Lee, B. R. Evans, and J. Woodward, "The mechanism of cellulase action on cotton fibers: evidence from atomic force microscopy," *Ultramicroscopy*, vol. 82, no. 1, pp. 213–221, 2000.

186 S. Gordon and Y.-L. Hsieh, Eds., *Cotton: Science and Technology (Woodhead Publishing in Textiles)*. Woodhead, 2007.

187 V. Mangipudi, M. Tirrell, and A. V. Pocius, "Direct Measurement of the Surface Energy of Corona-Treated Polyethylene Using the Surface Forces Apparatus," *Langmuir*, vol. 11, no. 1, pp. 19–23, Jan. 1995.

188 E. R. McCall and J. F. Jurgens, "Chemical composition of cotton," *Text. Res. J.*, vol. 21, no. 1, pp. 19–21, Jan. 1951.

189 C. K. Bragg and F. M. Shofner, "A rapid, direct measurement of short fiber content," *Text. Res. J.*, vol. 63, no. 3, pp. 171–176, Mar. 1993.